

Milena Sabrina Godoi Dias

Discrete time sliding mode control strategies
applied to a multiphase brushless DC machine

kassel
university 
press


Elektrische Energiesysteme

Band 14

Herausgegeben vom
Kompetenzzentrum für Dezentrale
Elektrische Energieversorgungstechnik

Discrete time sliding mode control strategies applied to a multiphase brushless DC machine

Milena Sabrina Godoi Dias

kassel
university 
press

Die vorliegende Arbeit wurde vom Fachbereich Elektrotechnik / Informatik der Universität Kassel als Dissertation zur Erlangung des akademischen Grades eines Doktors der Ingenieurwissenschaften (Dr.-Ing.) angenommen.

Erster Gutachter: Prof. Dr.-Ing. habil. Peter Zacharias

Zweiter Gutachter: Prof. Dr. Rodrigo Padilha Vieira

Tag der mündlichen Prüfung

20.01.2017

Bibliografische Information der Deutschen Nationalbibliothek
Die Deutsche Nationalbibliothek verzeichnet diese Publikation
in der Deutschen Nationalbibliografie; detaillierte bibliografische
Daten sind im Internet über <http://dnb.d-nb.de> abrufbar

Zugl.: Kassel, Univ., Diss. 2017

ISBN 978-3-7376-0318-8 (print)

ISBN 978-3-7376-0319-5 (e-book)

DOI: <http://dx.medra.org/10.19211/KUP9783737603195>

URN: <http://nbn-resolving.de/urn:nbn:de:0002-403193>

© 2017, kassel university press GmbH, Kassel

www.uni-kassel.de/upress

Druck und Verarbeitung: Print Management Logistics Solutions, Kassel
Printed in Germany

Acknowledgements

This dissertation has been realized during my time as a research assistant at the Center of Competence for Distributed Electric Power Technology (KDEE) at the University of Kassel. While writing this dissertation I worked at projects related to the control of electrical machines in partnership with the industry.

I especially owe my gratitude to my supervisor Prof. Dr–Ing. habil. Peter Zacharias for his support and encouragement, his valuable help and suggestions during this study. Additionally, I would like to thank him for giving me the opportunity to realize this work.

I would also like to thank my second supervisor Prof. Dr. Rodrigo Padilha Vieira. His knowledge and experience in the field of control strategies applied to electrical machines has contributed to this work through important discussions and recommendations.

I want also to thank Prof. Dr. rer. nat. Ludwig Brabetz and Prof. Dr–Ing Markus Ziegler for taking part in the examination board.

I would like to express my gratitude to Samuel Vasconcelos de Araújo for his support to my research. Moreover, I am very thankful to the valuable help of my colleagues from KDEE, Christian Felgemacher, Christian Nödig and Bernhard Siano, in the implementation of the experimental setup.

I am grateful to all my colleagues from KDEE for the friendly working atmosphere and good teamwork. In particular, I would like to thank, Anja Clark-Carina, Lucas Menezes, Marita Wendt, Dario Lafferte, Manuel Günther, Eduardo Façanha and Markus Horn for their fellowship and assistance during my work.

To my dear parents, Salete and Moisés, and to my sister Mariana, I would like to express my gratitude for the constant encouragement and love, not only during my studies, but also in every moment of my life.

Many thanks to my husband Guilherme to be by my side at all moments, encouraging me to persevere and face the tough times and celebrating with me the achieved goals.

Thanks to Francisco for brightening my days.

Milena Sabrina Godoi Dias

Abstract

Nowadays, environmental issues motivates the replacement of mechanical, hydraulic and pneumatic system by electrical system in the transport sector aiming to reduce emissions generated by burning of fossil fuels in vehicles. The electrical system must ensure high electrical efficiency and should not exceed the weight of the substituted components. To attend these high performance requirements a fault-tolerant multiphase brushless DC machine was chosen for this research.

The present work introduces a six-phase 600W brushless DC machine with 8 poles. The main challenge for the control issues of this machine is the mutual magnetic coupling between the phases due to the wave winding machine configuration.

In this context, theoretical and practical investigations of different current control strategies based on the sliding mode control approach applied to the six-phase brushless DC machine are presented.

Firstly, the theoretical background of the continuous time sliding mode control is introduced. Subsequently, robust current controllers based on discrete time sliding mode approach are developed as well as the proof of stability and convergence of these algorithms. The controllers and observers are developed in discrete time domain aiming to the practical experimentation in a FPGA platform.

Due to the fact that the motion of a discrete time sliding mode system occurs in a limited quasi-sliding mode band, the robustness of the controller is reduced and for this reason a combination of the proposed controllers with disturbance observers is suggested in order to diminish the chattering effect and ensure a good performance of the system even when parameter uncertainties and non-idealities are added to the nominal model.

Aiming to minimize the effect caused by the mutual coupling between the phases, and consequently the torque oscillations, an optimized current reference is proposed in this work.

Simulation and experimental investigations are carried out in order to validate the proposed strategies. The performance of the controllers are analyzed considering the tracking accuracy, and mainly the resulting torque oscillations, since the application of this techniques in traction systems is desired.

Zusammenfassung

Heutzutage motiviert die Umweltproblematik den Austausch bestehender mechanischer, sowie hydraulischer und pneumatischer Systeme durch hoch-effiziente elektrischen Systeme für den Verkehrssektor, um die dementsprechende CO₂-Emissionen zu verringern, die durch die Verbrennung fossiler Brennstoffe entstehen. Das elektrische System soll einen hohen Wirkungsgrad gewährleisten und das Gewicht der ersetzten Komponenten nicht überschreiten. Zur Berücksichtigung dieser hohen Leistungsanforderungen wurde eine fehlertolerante mehrphasige bürstenlose Gleichstrommaschine für diese Dissertation ausgewählt.

Die vorliegende Arbeit stellt eine bürstenlose sechsphasige 600W Gleichstrommaschine mit 8 Polen vor. Die Hauptherausforderung für die Regelung dieser Maschine ist die magnetische Kopplung zwischen den Phasen aufgrund der Maschinenkonfiguration mit Wellenwicklung.

In diesem Zusammenhang werden theoretische und praktische Untersuchungen verschiedener, auf dem Sliding-Mode-Regelungsansatz basierten Stromregelungsstrategien dargestellt.

Zuerst werden die theoretischen Grundlagen der kontinuierlichen Sliding-Mode-Regelung präsentiert. Anschließend werden robuste, auf der zeitdiskreten Sliding-Mode-Regelung basierte Stromregler entwickelt, sowie der Nachweis für Stabilität und Konvergenz dieser Algorithmen gezeigt. Die Regler und Beobachter wurden für einen diskreten Zeitbereich entwickelt, da die praktischen Laboruntersuchungen in einer FPGA-Plattform implementiert worden sind.

In Anbetracht der Tatsache, dass die Bewegung eines zeitdiskreten Sliding-Mode-Systemzustands in einem limitierten Quasi-Sliding-Mode-Bereich geschieht, wird die Robustheit des Reglers reduziert. Aus diesem Grund wird eine Kombination aus den vorgeschlagenen Reglern mit

Störungsbeobachtern zwecks der Verringerung des Chattering-Effekts und der Gewährleistung einer guten Leistungsfähigkeit des Systems empfohlen, selbst wenn Parameterungewissheit und Nichtidealität zum Nominalmodell hinzu kommen.

Damit die Wechselwirkungen der magnetischen Kopplung zwischen den Phasen und somit die Drehmomentschwingungen minimiert werden, wurde ein optimierter Stromsollwert für die vorliegende Arbeit vorgeschlagen.

Simulations- und Laboruntersuchungen sind zwecks der Validierung der vorgeschlagenen Strategien durchgeführt worden. Die Leistungsfähigkeit der Regler wurde unter Berücksichtigung der Genauigkeit der Stromsollwertverfolgung und hauptsächlich der resultierenden Drehmomentschwingungen analysiert, da die Anwendung dieser Technik in Traktionssystemen erfolgen soll.

Contents

1. Introduction	1
1.1. Work motivation and overview	1
1.2. Research objectives	6
1.3. Scientific contributions	7
1.4. Structure of the work	8
2. Modelling of six-phase brushless DC machine	9
2.1. Permanent magnet machine	9
2.2. Six-phase brushless DC machine	16
2.2.1. Commutation of the six-phase BLDC machine	18
2.2.2. Six-phase BLDC model	19
2.2.3. State-space model of six-phase BLDC machine	23
2.2.4. Discrete time state-space model of the six-phase BLDC machine	25
2.2.5. Measurement of self- and mutual inductances	25
2.2.6. Measurement of back-emf	26
2.2.7. Summary	29
3. Current control strategies applied to the brushless DC machine	30
3.1. Introduction	30
3.2. Proportional-integral current controller	31
3.3. Continuous time sliding mode controller	34
3.3.1. Sliding surface design	35
3.3.2. Control law design	38
3.3.3. Stability proof of continuous time sliding mode	40
3.3.4. Chattering	42

3.4.	Discrete time sliding mode controller	46
3.4.1.	Discrete time sliding mode controller using Gao's approach applied to the six-phase BLDC machine	48
3.4.2.	Stability proof of the discrete time sliding mode controller on the basis of a Lyapunov function	51
3.4.3.	Stability proof of the discrete time sliding mode controller on the basis of a Lyapunov function considering disturbance in the system.	55
3.5.	Discrete time super-twisting controller	57
3.5.1.	Discrete time super-twisting controller applied to the six-phase BLDC machine	59
3.5.2.	Stability proof of the discrete time super-twisting controller on the basis of a Lyapunov function considering disturbance in the system.	61
3.6.	Simulation results	62
3.6.1.	Discrete time proportional-integral controller	63
3.6.2.	Continuous time sliding mode controller	64
3.6.3.	Discrete time sliding mode controller: Gao's approach . . .	66
3.6.4.	Discrete time sliding mode controller: super-twisting approach	68
3.6.5.	Speed control	70
3.6.6.	Summary	72
4.	Discrete time disturbance observer applied to the BLDC ma- chine	74
4.1.	Introduction	74
4.2.	DSMC with decoupled variable structure disturbance observer	75
4.3.	DSMC with reduced order disturbance observer	78
4.4.	Discrete time super-twisting control with reduced order dis- turbance observer	80
4.5.	Current reference optimization	81
4.6.	Simulation results	83
4.6.1.	Discrete time sliding mode control with decoupled variable structure disturbance observer	85

4.6.2. Discrete time sliding mode control with reduced order disturbance observer	87
4.6.3. Discrete time super-twisting control with reduced order disturbance observer	87
4.6.4. Discrete time sliding mode control with decoupled variable structure disturbance observer and optimized current reference	89
4.6.5. Discrete time sliding mode control with reduced order disturbance observer and optimized current reference	91
4.6.6. Discrete time super-twisting control with reduced order disturbance observer and optimized current reference	91
4.6.7. Summary	94
5. Experimental Results	96
5.1. Description of the experimental setup	96
5.1.1. Unipolar four-quadrant PWM technique	101
5.2. Discrete time proportional-integral current controller	104
5.3. Discrete time sliding mode controller based on Gao's approach	109
5.4. Discrete time super-twisting sliding mode controller	112
5.5. Gao's approach DSMC with decoupled disturbance observer	116
5.6. Gao's approach DSMC with reduced order disturbance observer	121
5.7. Torque load variation and proportional-integral speed control	125
5.8. Summary	129
6. Conclusions and future work	130
List of Figures	145
List of Tables	152
Acronyms	153
Symbols	154
Appendices	159

A.	Gain design of proportional-integral controller	160
A.1.	Proportional-integral current controller: gain design	160
A.2.	Proportional-integral speed controller: gain design	163
B.	Mathematical development for control stability analysis	165
B.1.	Stability proof of continuous time sliding mode controller . .	165
B.2.	Stability proof of DSMC based on a Lyapunov function . . .	166
B.3.	Stability proof of DSMC based on a Lyapunov function - Lower limit of ε	168
B.4.	Stability proof of DSMC based on a Lyapunov function . . .	169
B.5.	Stability proof of DSMC with disturbances in the model . .	170
B.6.	Stability proof of DSTC with disturbances in the model . .	174

1. Introduction

1.1. Work motivation and overview

The transportation sector — including road transport, aviation and maritime sectors — is responsible for about 23% of the world's CO₂ emissions from the combustion of petroleum-based products. These emissions have risen about 36% as a consequence of the increase in the amount of personal and freight transport during the period between the years 1990 and 2007 [1].

As issues relating to climate change and shortage of resources now appear more and more before the public, transport sector emissions should be significantly reduced to minimize the depletion of natural resources and to achieve the strict reduction targets defined in the Copenhagen Accord (2010).

The concerns relating to environmental issues, such as global warming and the greenhouse effect, motivate the development of researches which aim to replace the mechanical, hydraulic and pneumatic systems by the electrical system in the transport sector. It is expected that such replacements would help to reduce the carbon dioxide (CO₂) emissions generated by, for example, the burning of fossil fuels in personal vehicles or in aircrafts.

The substitution of these systems by the electrical system is carried out with the use of electric machines. Electric machines are the most common devices for industrial, commercial and residential sectors; they are responsible for the consumption of about 60% of the energy generated around the world. Energy efficiency improvement in electric machines is required in order to reduce the energy consumption. It is estimated that

increases in the energy efficiency of machine drives could reduce the energy consumption by about 7% [1].

The air traffic grew considerably during the last few years and it is still showing an increasing trend. To fulfill this demand, the aircraft system should operate more efficiently in order to attenuate the CO₂ emissions by reducing the fuel consumption.

The More Electrical Aircraft (MEA) concept intends to avoid polluting emissions and simultaneously to ensure high electrical efficiency by substituting the mechanical, hydraulic and pneumatic systems by the electrical system in aircrafts. Beyond a high efficiency, it should also ensure that the weight of the electrical system does not exceed the substituted components [2]. Hence, hydraulic actuators are gradually replaced by Electromechanical Actuators (EMAs) in aircraft applications. EMAs are used in secondary applications (stairs, door actuation and door-locking device) and also in more significant applications such as brakes, spoilers, or flap actuation [3].

In addition, the number of personal cars has become greater with increases in the global population. Most of these vehicles are equipped with Internal Combustion Engine (ICE), causing the depletion of fossil-fuel resources and being the major source of urban pollution, mainly through CO₂ emissions which contribute to the greenhouse effect [4, 5].

Environment awareness research and development efforts are now being carried out to make Electric Vehicles (EVs) and Hybrid Vehicles (HEVs) commercially viable. These work as an alternative to replacing the ICE automobiles. EVs were invented in the middle of the 19th century and they were very popular until 1918. However, their usage reduced drastically soon after due to the limitation associated with the batteries as well as the rapid advance of ICE automobiles [6].

The choice of the electric machine used for electric propulsion system in the electric vehicle or in the aircraft system is a crucial decision. Some requirements of the machine used in these applications are high power and torque density, robustness for different operating conditions, reasonable cost and reduced weight and volume.

Beyond that, in electric vehicles or aircraft applications, the system should operate with high reliability and must also have fault tolerance properties so that it can continue in operation even in case of a failure in the machine or in the converter. To fulfill this requirement, a multiphase machine supplied by a multiphase drive, with each phase as a single module is a good option.

Switched reluctance and brushless DC (BLDC) are good candidates for multiphase machines. However, BLDC machines present more advantages when compared with classical machines since they present reduced weight and volume as well as ease of refrigeration, all of which favour its use in limited space. Moreover, high power and torque density are important features of BLDC machines.

According to what is described in the literature [7], each single-phase module should present minimal electrical, magnetic and thermal interaction with the other phases in an ideal fault-tolerant drive. A machine designed with concentrated windings around each tooth provides thermal and magnetic isolation between the coils. However, this work investigates a six-phase brushless DC machine with a wave winding configuration. An advantage of the wave winding configuration is the reduction of the machine frame size, but it also significantly increases the magnetic coupling between the phases. The strong mutual coupling between the phases in this machine is the main challenge for the current control loop design as it increases significantly the complexity of the model. This is because the self- and mutual inductances vary in accordance with the rotor's position and the current amplitude.

The most common controller applied to the BLDC machine is the classical Proportional Integral (PI) controller. However, in this particular case, where parameter variations and uncertainties are added to the nominal model, the proportional-integral controller does not have the robustness property to overcome these disturbances and consequently fails to ensure a good dynamic response within the entire machine operation range.

A satisfactory dynamic response over the entire operation range can be achieved if the PI controller gains are carefully tuned, but there is still the

risk that the control would become unstable due to its limited bandwidth. Beyond that, considering that the model is nonlinear, the classical control strategies are not ideal for the controller design.

The performance of BLDC machines can be improved by using a robust control technique such as nonlinear adaptive control [8], model predictive control [9], or sliding mode control [10, 11]. These techniques ensure a good system performance, even against disturbances added to the model and are an appropriate tool for solving problems of a nonlinear nature.

Taking into consideration that nonlinear adaptive control and predictive control require extensive calculations and that they usually lead to a more complex implementation, the sliding mode control technique will be investigated owing to its simplicity and robustness property.

The sliding mode approach is a variable structure control technique (VSC) that provides robustness to the system in the presence of uncertain parameters or disturbances; it often provides systems completely insensitive to these perturbations — in other words, invariant systems. The sliding mode uses a discontinuous control law with high-frequency switching control to orientate the system trajectory to a determined region in the state-space, known as sliding surface and it is kept there for all future time, regardless the plant parameter variations.

However, the sliding mode on the sliding surface occurs just when an infinite switching frequency is considered. The switching frequency in real systems is nevertheless limited and therefore the system slides in the vicinity of the surface, causing high-frequency oscillations around this region. This phenomenon, known as chattering, is inherent to the discontinuous control, being the main restriction of this kind of control [12, 13]. The chattering mitigation is obtained by changing the dynamics of the system in the vicinity of the sliding surface, avoiding the discontinuity and preserving the main properties of the original system.

Most of the control strategies are nowadays implemented by using microcontrollers. The measurements of some system variables, such as phase currents, must be sampled for being used in the microprocessor which is made by an analog-to-digital convert (AD converter). Hence, a

continuous time control system is controlled by a discrete time computer, which happens to be a limitation of the continuous time sliding mode control implementation since it is intrinsically a continuous time control technique whose implementation requires high switching frequency.

Assuming that the implementation is based on a digital microprocessor, the information on control law can be updated at each sampling period, which degrades the performance of the continuous time sliding mode controller. Some approaches employ the discretization of the sliding mode control law established in continuous time for digital implementation [14]; but, in this case, the stability proof law is developed in a continuous time domain and it is no longer valid in a discrete time domain.

This fact motivates the research on the discrete time formulation of the sliding mode controller. Different approaches are presented in the literature for the development of a discrete time sliding mode control law. This work focuses on the research of the approach presented in [15]. In order to ensure the stability of a system in discrete time sliding mode, the reaching condition must be modified in relation to continuous time. In the reaching law considered in [15], the state trajectory should cross the sliding surface in each sampling time. Hence, the system moves it in a quasi-sliding mode band around the sliding surface and not more on the sliding surface such as in the continuous time sliding mode control. With this, it concludes that it is not possible to acquire an ideal sliding mode with the discrete time sliding mode controller and consequently the invariance property is lost. Despite this, a significant robustness, related to the width of the quasi-sliding mode band, is preserved and the system can overcome uncertainties and disturbances added to the model. The quasi-sliding mode width depends on the sampling period and the control parameters. For this reason, the robustness is limited and there is the possibility that the system would suffer from chattering when large disturbances are added to the model.

An association of a discrete time sliding mode control law, with a disturbance observer, is an alternative to improving the robustness of

the system and the reference tracking accuracy such as those proposed in [16–23].

This work presents a scenario where the uncertainties and parameter variations intrinsic to the system are accounted as disturbance terms added to the nominal model of the six-phase brushless DC machine. Hence, considering that these disturbances are rather weighty, a controller design procedure, based on the combination of a discrete time sliding mode control and a discrete time disturbance observer, is developed.

1.2. Research objectives

This work aims to the study of sliding mode controllers combined with a disturbance observer in a discrete time domain applied to the current control of a multiphase fault-tolerant brushless DC machine. The BLDC machine investigated in this work presents strong mutual coupling between the phases, and the self- and mutual inductances are dependent on the rotor position and on the current amplitude — all of which result in a model with nonlinear characteristics. Therefore, the use of a linear classical controller with limited bandwidth is not adequate for this application. In looking for good machine performance, this work seeks to investigate and to develop robust controllers based on the sliding mode technique which is an appropriate tool for solving problems of a nonlinear nature. It is also able to overcome the fact that the model is not exactly known for presenting parameter variations and disturbances. The theoretical formulation of the controllers and observers for the multiphase BLDC machine model and the mathematical controller's stability analysis are included in the study aiming its subsequent implementation. In order to experimentally investigate the performance of the proposed control strategies, the development of an experimental setup, based on the FPGA system and the implementation of the control strategies in VHDL code, is part of the research. The dynamic controller response and robustness, the presence of chattering and the observer's ability to observe and decouple the disturbances of the system under conditions of parameter uncertainties

and strong coupling between the phases are elements considered in the analysis of the obtained results. Furthermore, the torque oscillations analyzed in the results is a very important issue for this research since the main purpose is to obtain a resultant torque with minimal oscillations, even in a system with uncertainties and parameter variation, aiming to the application of this research in traction systems where a torque with no oscillations over the entire operation range is a requirement.

1.3. Scientific contributions

The main contributions achieved with the development of this work are:

- Analysis and development of high performance current control strategies based on the discrete time sliding mode technique applied to a multiphase BLDC machine under conditions of parameter uncertainties and strong magnetic coupling between the phases. The controllers developed in this work are the first-order sliding mode controller based on Gao's approach and the second-order sliding mode based on the super-twisting algorithm;
- Analysis and development of disturbance observers, in combination with current controllers in the discrete time domain, which are applied to the multiphase BLDC machine in a scenario where parameter variations and uncertainties are treated as disturbances added to the nominal model;
- Development of an optimized current reference in order to mitigate the effect of the mutual coupling between the phases of the multiphase BLDC machine;
- Development of an experimental setup based on the FPGA system to investigate the control strategies applied to a prototype multiphase BLDC machine.

1.4. Structure of the work

This work presents theoretical, simulation and practical analysis that are structured into six chapters as the following: Chapter 2 provides an overview of the permanent magnet synchronous machine and it presents the concept of the six-phase fault-tolerant brushless DC machine. Chapter 3 presents the current controller strategies developed in the discrete time domain applied to the multiphase BLDC machine and their mathematical stability analysis. The continuous time sliding mode control is also presented in this chapter in order to provide the tools for the understanding and development of discrete time sliding mode techniques. The development of disturbance observers is carried out in Chapter 4. Simulation results are presented in Chapters 3 and 4 in order to verify the performance of the proposed controllers and disturbance observers. Chapter 5 presents an experimental investigation of the proposed strategies that are applied to the multiphase BLDC, as well as a description of the developed experimental setup. The results, general conclusions and suggestions for future work are included in Chapter 6.

2. Modelling of six-phase brushless DC machine

2.1. Permanent magnet machine

The use of permanent magnet motors has increased considerably in the last few decades, mainly in applications where high efficiency and high power density are needed. The great advances relating to magnetic materials has enabled the manufacturing of magnets with high energy density by using rare earth magnets, such Samarium Cobalt (SmCo) and Neodymium Iron Boron (NdFeb), at reasonable costs. Furthermore, the development of the power electronic semiconductor switches technology and digital signal processors has fomented the use of converters and hence the use of electronically commutated machines such as the brushless DC machine.

Permanent magnet motors present high efficiency compared with the conventional machines such as Induction Motors (IM) and brushed DC Motors. When compared with brushed DC motors, permanent magnet motors require reduced maintenance and have longer life due to the absence of the brushes. The presence of mechanical commutators and brushes is the main drawback of a brushed DC motor, as they require periodic maintenance, thereby providing lower speed range due to mechanical limitations.

Induction motors, which are technically more mature, are well accepted due to low cost, low torque ripple and the possibility to improve its dynamic performance that may reach the extended speed range by flux weakening. However, the rotor losses are significant, which requires cooling and restriction of the overload capacity.

Recently, the switched reluctance machine has aroused interest due to the fact that it has one phase decoupled from another ensuring high fault tolerance. It presents simple construction, low maintenance and power density and efficiency when compared with the induction motor. The main disadvantages of this machine are the presence of high torque ripple at low speeds and acoustic noise problems, while its control is intricate due to high nonlinearity [24].

The main advantage of the permanent magnet motor over other machines is its high-power density with reduced weight and volume, which happens to be ideal for applications with space restriction or in areas where the access is limited. It presents lower rotor inertia due to the arrangement of the permanent magnets on the rotor side and the windings on the stator side — all of which mitigate the electrical losses and allows better heat dissipation.

Permanent magnet motors are classified into permanent magnet synchronous motors (PMSM) and brushless DC motors (BLDC). The shape of the back electromotive force (back-emf) waveform distinguishes both machines, as presented in Figure 2.1. The PMSM presents a sinusoidal back-emf waveform and needs sinusoidal currents to produce a constant torque, while the shape of the back-emf waveform in the BLDC machine is trapezoidal and needs rectangular stator currents to produce constant electric torque. This difference between the two back-emf waveforms depends on the interconnection of coils in stator windings and the shape of magnets. This differentiation impacts the drive choice and the control structure [24].

The three-phase converter topology with MOSFETs or IGBTs with star connection, as shown in Figure 2.2, is adequate and commonly used in the three-phase BLDC machine. In this configuration two phases are conducting at the same time during 120 electrical degrees and one phase is non-energized during 60 electrical degrees. The rectangular pulses of the phase current must coincide with the crest of the back-emf in the corresponding phase, as shown in Figure 2.3. The drive operation of the BLDC motor must be synchronized with the rotor position to energize

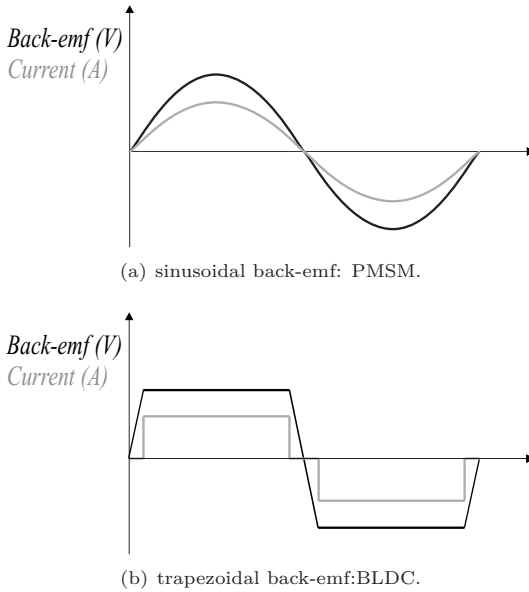


Figure 2.1.: Back-emf and phase current in the PMSM and in the BLDC machine.

the windings in the appropriate sequence. Usually, the position sensing is made by Hall effect sensors — one Hall effect sensor is used for each phase — which reduce the costs of the BLDC drive system in comparison with the PMSM that requires a high-resolution feedback system (encoder or resolver) which provides continuous and instantaneous rotor position feedback to supply the magnitude of sinusoidal currents and voltages [24, 25].

The BLDC motor needs the rotor-position feedback just at the commutation points — what means at every 60 electrical degrees in a three-phase motor — which results in six commutation sectors, as shown in Figure 2.3 [24, 26, 27].

In some applications, in order to reduce the cost and size of the motor, the sensor is undesirable and the rotor position can be obtained through sensorless techniques. The sensorless techniques applied to the brushless DC motor are widely investigated in the literature [28–31].

2. Modelling of six-phase brushless DC machine

Another advantage of the BLDC over the PMSM is that the power density of the former is 15% greater than that in the latter [32].

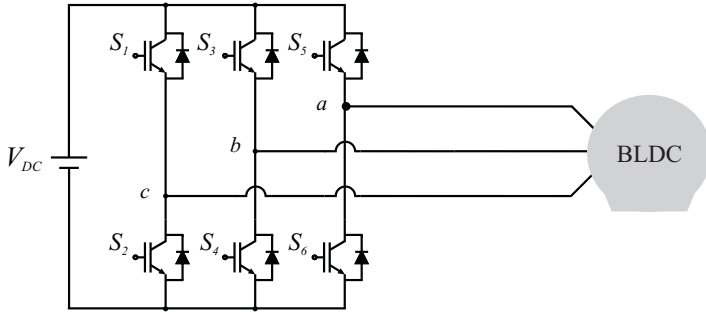


Figure 2.2.: Typical BLDC driver topology.

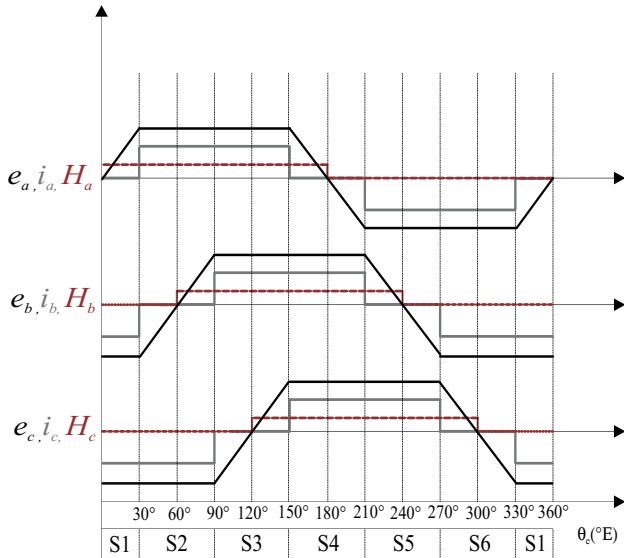


Figure 2.3.: Hall sensor, back-emf and phase currents in the BLDC machine.

Considering that the copper losses in the machine determine its power density, it is possible to obtain the relationship between them by equating the copper losses of the two machines.

$$P_{CPMSM} = P_{cBLDC} \quad (2.1)$$

$$3R_s I_{PMSM}^2 = 3R_s I_{BLDC}^2 \quad (2.2)$$

where I_{PMSM} and I_{BLDC} are RMS currents in each machine and are given by:

$$I_{PMSM} = \frac{I_{peakPMSM}}{\sqrt{2}} I_{BLDC} = \sqrt{\frac{2}{3}} I_{peakBLDC} \quad (2.3)$$

where $I_{peakPMSM}$ and $I_{peakBLDC}$ are the stator peak currents in the permanent magnet synchronous machine and in the brushless DC machine, respectively. Substituting (2.3) into (2.2), the relationship between the peak currents in the machines is obtained:

$$3R_s \left(\frac{I_{peakPMSM}}{\sqrt{2}} \right)^2 = 3R_s \left(\sqrt{\frac{2}{3}} I_{peakBLDC} \right)^2 \quad (2.4)$$

$$I_{peakBLDC} = \frac{\sqrt{3}}{2} I_{peakPMSM} \quad (2.5)$$

The peak of the back-emf is equal for both machines and denoted by E . In the BLDC motor only two phases conduct current at the same time, while in the PMSM all three phases conduct current for all time instants. Thus, the ratio between the power outputs in the machines can be determined by:

$$\frac{P_{BLDC}}{P_{PMSM}} = \frac{2EI_{peakBLDC}}{3 \frac{E}{\sqrt{2}} \frac{I_{peakPMSM}}{\sqrt{2}}} = \frac{2E \frac{\sqrt{3}}{2} I_{peakPMSM}}{3 \frac{E I_{peakPMSM}}{2}} = 1.154 \quad (2.6)$$

confirming that a three-phase BLDC machine can provide 15% more power density than a three-phase PMSM with the same stator resistance and the same frame size.

Considering that the relationship between power, electric torque and speed in a machine is given by:

$$P_{out} = \omega_r T_e \quad (2.7)$$

Comparing the machines with the same rated speed, it is possible to conclude mathematically that the BLDC machine also presents 15% more torque density than the PMSM. The higher torque density can be attributed to the interaction between the fundamental component of the rectangular current and the fundamental component of the trapezoidal back-emf in the BLDC machine [24].

Due to its advantages like high power and torque density, reduced volume and size, low maintenance and control simplicity, the use of the brushless DC motor has become interesting in many domestic, commercial and industrial applications. It has recently become interesting in the field of electrical and hybrid electrical vehicles due to environmental concerns.

A drawback of the BLDC machine is its high torque pulsations constituted by cogging torque and ripple torque. The cogging torque is produced by the interaction between the permanent magnet on the rotor and the stator slots, causing reluctance variations that depend on the angular position and it is independent of the current presence [33].

The ripple torque is produced by the interaction between the stator current and the back-emf when the waveform shape is non-ideal. The non-idealities of the back-emf waveforms — caused by the motor construction — can be reduced by an appropriate machine design, thereby making the crest of the back-emf be wide and flat as possible.

Another source of ripple torque in the BLDC machine is the commutation torque ripple that happens at each commutation point. To get the ideal rectangular currents, the commutations must be instantaneous; however, due to the electrical time constant of the motor windings, the current cannot immediately commutate and requires finite time [34].

One way to mitigate the torque pulsations is by increasing the number of phases [35,36]. According to [37], the lowest torque ripple component is proportional to $2n_f$, where n_f represents the number of phases, and therefore increasing the number of phases reduces the amplitude of the torque pulsation and increases the frequency of the torque pulsation.

Another advantage of the multiphase machine is the possibility to reduce the current per phase without increasing the voltage per phase beyond their fault tolerance and high-reliability characteristics. In a fault-tolerant motor drive, the system should continue to operate safely even after a fault occurs.

In high-performance applications where the high reliability of the system is crucial — such as electrical and hybrid vehicles, ship propulsion, or aerospace applications — the use of the multiphase fault-tolerant brushless DC machine can be a promising alternative, which would ensure a safety operation even after a failure occurs [3,38,39].

The more common faults that occur in a drive system are related to the machine, such as the winding open circuit and the winding short-circuit, or related to the power electronic converter, such as the inverter switch open circuit and the inverter switch short-circuit. A modification in the machine design can improve the fault tolerance ability of the system [7,40]. This is achieved by configuring the BLDC windings, similar to the configuration windings used in the switched reluctance motors. According to [7], considering each phase as a single module with minimal electrical, magnetic and thermal interaction between the phases improves the fault tolerance and increases the reliability of the system. A machine's design with concentrated windings around each tooth provides thermal and magnetic isolation between the coils, avoiding mutual coupling between the phases. Supplying each phase with a single-phase bridge, the number of switches and the volume of the drive unit will increase, as well as the number of drive signals that require a digital signal processor with high PWM and I/Os capacity. However, the electrical isolation between the phases is ensured.

When a failure occurs, the fault-tolerant system continues to operate but with a degraded performance. To improve the performance and ensure a torque with minimal oscillations, besides the fault-tolerant machine and driver design, a remedial control strategy should be adopted when a failure occurs in the system. Such a strategy basically modifies the current waveform of the operating phases by changing the current reference of each phase.

The choice of a fault-tolerant drive increases the system's costs and hence its use is economically justified in specific applications where a fault implies risks relating to human safety or loss of production.

This work presents a six-phase fault-tolerant BLDC machine, with each phase as a single module. The machine and driver characteristics are described in the following sections.

2.2. Six-phase brushless DC machine

The motor considered in this work is a prototype brushless DC machine with six independent phases used in electrical auxiliary systems for electric vehicles, such as oil pump systems. The machine configuration can also be extended to applications with higher power. It has eight poles (permanent magnets) on the rotor and 48 stator slots. As shown in the cross-section of the motor (Figure 2.4), it presents an outer rotor design, also called the inside-out motor [33], with an inner stator and the rotor magnets surrounding the stator.

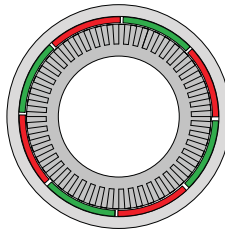


Figure 2.4.: Cross section of six-phase BLDC.

The magnetization of the permanent magnets and their displacement on the rotor are chosen in such a way that the back-emf shape is trapezoidal. Figure 2.5 shows the winding arrangement in the stator of the six-phase BLDC machine. Each phase winding is arranged in the stator in the form of wave winding, which means that the end of a coil is connected with the beginning of the next coil until the winding closes on itself. The wave winding configuration makes the machine construction more compact and its frame size is reduced, but it increases the mutual coupling among the phases. Six Hall effect sensors are embedded in the machine stator slots. The hall sensors are responsible for the rotor position sensing and the identification of the commutation points.

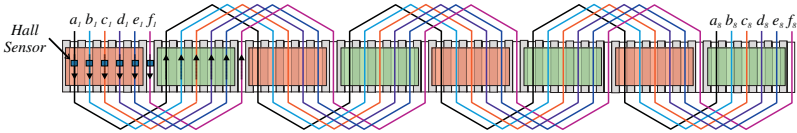


Figure 2.5.: Wave winding.

For an appropriate operation of a multiphase fault-tolerant machine each phase must be supplied by a separate H-bridge, ensuring the minimal electrical interaction between the phases and consequently improving the fault tolerance and reliability of the system, as shown in Figure 2.6 [7, 40].

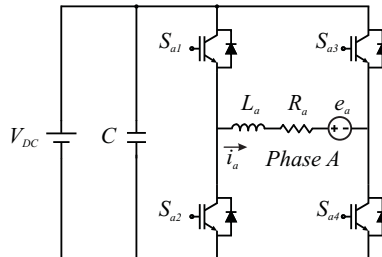


Figure 2.6.: One phase configuration of BLDC motor drive system.

2.2.1. Commutation of the six-phase BLDC machine

Due to the absence of brushes for commutation, the BLDC machine is electronically commutated and synchronized with the rotor position. Hence, the stator windings should be energized in a sequence.

The commutation sequence can be determined based on the combination of the six hall sensor signals. When the hall sensor changes its state from 0 to 1, the current should change its direction for negative to positive. For a machine with six phases and six hall sensor signals there are 12 commutation sectors for each electrical rotation.

In order to produce constant electromagnetic torque in the BLDC machine with trapezoidal back-emf, the phase currents must be rectangular and synchronized with the rotor position. As previously mentioned, the pulses of the phase current must coincide with the crest of the back-emf in the corresponding phase and the polarity of the current corresponds to that of the back-emf. Figure 2.7 shows the commutation sectors, with the hall sensor signals, phase current and back-emf.

The commutation in a six-phase BLDC occurs in every 30 electrical degree — each phase conducts during 150 electrical degrees and in each sector five phases conduct at the same time. This is presented in the Table 2.1.

Sector	Electrical Angle	Conducting Phases	Hall sensor state					
			Ha	Hb	Hc	Hd	He	Hf
S1	345°-15°	-B, -C, -D, -E, -F	1	0	0	0	0	0
S2	15°-45°	+A, -C, -D, -E, -F	1	1	0	0	0	0
S3	45°-75°	+A, +B, -D, -E, -F	1	1	1	0	0	0
S4	75°-105°	+A, +B, +C, -E, -F	1	1	1	1	0	0
S5	105°-135°	+A, +B, +C, +D, -F	1	1	1	1	1	0
S6	135°-165°	+A, +B, +C, +D, +E	1	1	1	1	1	1
S7	165°-195°	+B, +C, +D, +E, +F	0	1	1	1	1	1
S8	195°-225°	-A, +C, +D, +E, +F	0	0	1	1	1	1
S9	225°-255°	-A, -B, +D, +E, +F	0	0	0	1	1	1
S10	255°-285°	-A, -B, -C, +E, +F	0	0	0	0	1	1
S11	285°-315°	-A, -B, -C, -D, +F	0	0	0	0	0	1
S12	315°-345°	-A, -B, -C, -D, -E	0	0	0	0	0	0

Table 2.1.: Conducting phases in accordance with the operation sectors.

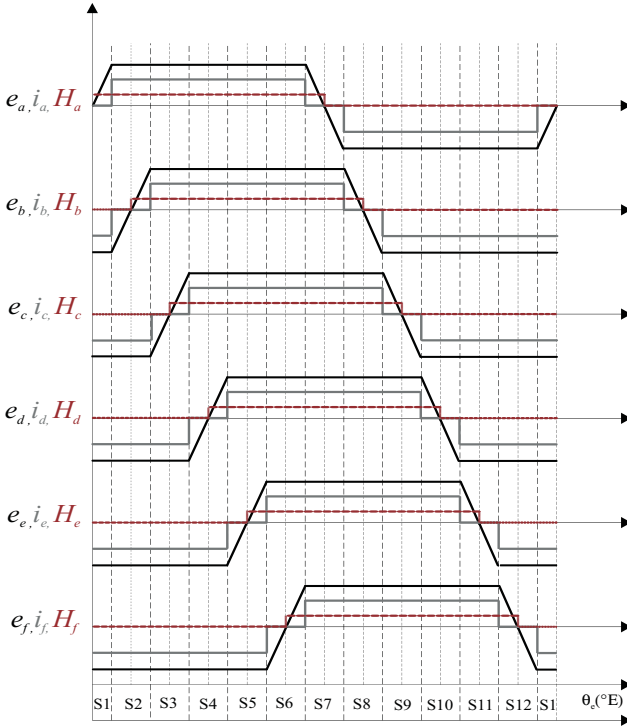


Figure 2.7.: Back-emf, Hall sensor signals and phase current waveforms in accordance with the electrical angle.

2.2.2. Six-phase BLDC model

This section presents the development of a phase variable model for the BLDC machine. Due to the trapezoidal back-emf, the use of the dq model does not eliminate the angle-dependent phase inductances and therefore does not offer many advantages. Other modelling methods such as harmonic modelling or methods based on finite element analysis are presented in the literature [38, 41–44]. These, however, require complex mathematical calculations and computation [45]. Hence, the phase variable approach is more adequate for this machine and will be used in this work [26]. It is

2. Modelling of six-phase brushless DC machine

considered that the BLDC has symmetrical phases distributed every 60° in the stator. The BLDC dynamic model can be obtained in accordance with the voltage equations in abc coordinates. This is shown in the following:

$$\begin{aligned}
 \begin{bmatrix} v_a \\ v_b \\ v_c \\ v_d \\ v_e \\ v_f \end{bmatrix} &= \begin{bmatrix} R_s & 0 & 0 & 0 & 0 & 0 \\ 0 & R_s & 0 & 0 & 0 & 0 \\ 0 & 0 & R_s & 0 & 0 & 0 \\ 0 & 0 & 0 & R_s & 0 & 0 \\ 0 & 0 & 0 & 0 & R_s & 0 \\ 0 & 0 & 0 & 0 & 0 & R_s \end{bmatrix} \begin{bmatrix} i_a \\ i_b \\ i_c \\ i_d \\ i_e \\ i_f \end{bmatrix} + \\
 &+ \begin{bmatrix} L_s & M_{ab} & M_{ac} & M_{ad} & M_{ae} & M_{af} \\ M_{ba} & L_s & M_{bc} & M_{bd} & M_{be} & M_{bf} \\ M_{ca} & M_{cb} & L_s & M_{cd} & M_{ce} & M_{cf} \\ M_{da} & M_{db} & M_{dc} & L_s & M_{de} & M_{df} \\ M_{ea} & M_{eb} & M_{ec} & M_{ed} & L_s & M_{ef} \\ M_{fa} & M_{fb} & M_{fc} & M_{fd} & M_{fe} & L_s \end{bmatrix} \frac{d}{dt} \begin{bmatrix} i_a \\ i_b \\ i_c \\ i_d \\ i_e \\ i_f \end{bmatrix} + \begin{bmatrix} e_a \\ e_b \\ e_c \\ e_d \\ e_e \\ e_f \end{bmatrix}
 \end{aligned} \tag{2.8}$$

where v_k is the phase voltage, i_k is the phase current, R_s is the stator resistance per phase, e_k is the phase back-emf, L_s is the self-inductance of each phase and M_{kl} is the mutual inductance between the phases k and l . Due to the winding symmetry, the mutual inductances can be defined as:

$$\begin{aligned}
 M_{ab} &= M_{bc} = M_{cd} = M_{de} = M_{ef} = M_{ba} = M_{cb} = M_{dc} = M_{ed} = M_{fe} = M_1 \\
 M_{ac} &= M_{bd} = M_{ce} = M_{df} = M_{ca} = M_{db} = M_{ec} = M_{fd} = M_2 \\
 M_{af} &= M_{fa} = -M_1 \\
 M_{ae} &= M_{bf} = M_{ea} = M_{fb} = -M_2 \\
 M_{ad} &= M_{be} = M_{cf} = M_{da} = M_{eb} = M_{fc} = M_3
 \end{aligned} \tag{2.9}$$

and (2.8) can be rewritten as:

$$\begin{aligned}
 \begin{bmatrix} v_a \\ v_b \\ v_c \\ v_d \\ v_e \\ v_f \end{bmatrix} &= \begin{bmatrix} R_s & 0 & 0 & 0 & 0 & 0 \\ 0 & R_s & 0 & 0 & 0 & 0 \\ 0 & 0 & R_s & 0 & 0 & 0 \\ 0 & 0 & 0 & R_s & 0 & 0 \\ 0 & 0 & 0 & 0 & R_s & 0 \\ 0 & 0 & 0 & 0 & 0 & R_s \end{bmatrix} \begin{bmatrix} i_a \\ i_b \\ i_c \\ i_d \\ i_e \\ i_f \end{bmatrix} + \\
 + \begin{bmatrix} L_s & M_1 & M_2 & M_3 & -M_2 & -M_1 \\ M_1 & L_s & M_1 & M_2 & M_3 & -M_2 \\ M_2 & M_1 & L_s & M_1 & M_2 & M_3 \\ M_3 & M_2 & M_1 & L_s & M_1 & M_2 \\ -M_2 & M_3 & M_2 & M_1 & L_s & M_1 \\ -M_1 & -M_2 & M_3 & M_2 & M_1 & L_s \end{bmatrix} \frac{d}{dt} \begin{bmatrix} i_a \\ i_b \\ i_c \\ i_d \\ i_e \\ i_f \end{bmatrix} + \begin{bmatrix} e_a \\ e_b \\ e_c \\ e_d \\ e_e \\ e_f \end{bmatrix}
 \end{aligned} \tag{2.10}$$

According to (2.10), one phase of the BLDC motor drive can be represented by Figure 2.8 as:

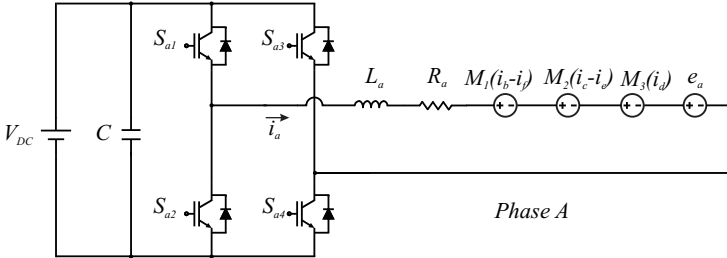


Figure 2.8.: Single phase bridge considering the mutual coupling in the model.

The instantaneous back-emf is assumed to be trapezoidal and can be expressed as:

$$\begin{aligned}
 e_a &= f_a(\theta_r) E \\
 e_b &= f_b(\theta_r) E \\
 e_c &= f_c(\theta_r) E \\
 e_d &= f_d(\theta_r) E \\
 e_e &= f_e(\theta_r) E \\
 e_f &= f_f(\theta_r) E
 \end{aligned} \tag{2.11}$$

According to [46], the functions f_k have the same shape as e_k , varying in accordance with the rotor position and with a maximum magnitude of $+/-1$. E represents the peak of the phase back-emf which is proportional to the rotor speed and is given by:

$$E = K_e \omega_r \tag{2.12}$$

where K_e is the back-emf factor and ω_r the rotor speed.

The electromagnetic torque is given by:

$$T_e = \frac{e_a i_a + e_b i_b + e_c i_c + e_d i_d + e_e i_e + e_f i_f}{\omega_r} \tag{2.13}$$

The equation of motion is expressed as:

$$\frac{d}{dt} \omega_r = \frac{T_e - T_L - b \omega_r}{J} \tag{2.14}$$

where J is the rotor inertia, b is the viscous damping coefficient and T_L the load torque.

The electrical rotor speed and the mechanical rotor speed are related by:

$$\omega_e = \frac{P}{2} \omega_r \tag{2.15}$$

where P is the number of pole pairs.

2.2.3. State-space model of six-phase BLDC machine

From the voltage equations of the six-phase BLDC machine in abc coordinates, as presented in (2.10), it is possible to obtain the model in state-space as:

$$\begin{cases} \dot{\mathbf{x}} = \mathbf{A}\mathbf{x} + \mathbf{B}\mathbf{u} + \mathbf{F}\mathbf{e} \\ \mathbf{y} = \mathbf{C}\mathbf{x} \end{cases} \quad (2.16)$$

The state vector \mathbf{x} is determined by:

$$\mathbf{x} = \begin{bmatrix} i_a & i_b & i_c & i_d & i_e & i_f \end{bmatrix}^T \quad (2.17)$$

The input vectors by:

$$\mathbf{u} = \begin{bmatrix} v_a & v_b & v_c & v_d & v_e & v_f \end{bmatrix}^T \quad (2.18)$$

$$\mathbf{e} = \begin{bmatrix} e_a & e_b & e_c & e_d & e_e & e_f \end{bmatrix}^T \quad (2.19)$$

Considering the inductance matrix given by:

$$\mathbf{\Gamma} = \begin{bmatrix} L_s & M_1 & M_2 & M_3 & -M_2 & -M_1 \\ M_1 & L_s & M_1 & M_2 & M_3 & -M_2 \\ M_2 & M_1 & L_s & M_1 & M_2 & M_3 \\ M_3 & M_2 & M_1 & L_s & M_1 & M_2 \\ -M_2 & M_3 & M_2 & M_1 & L_s & M_1 \\ -M_1 & -M_2 & M_3 & M_2 & M_1 & L_s \end{bmatrix} \quad (2.20)$$

and the resistance matrix:

$$\mathbf{R} = \begin{bmatrix} R_s & 0 & 0 & 0 & 0 & 0 \\ 0 & R_s & 0 & 0 & 0 & 0 \\ 0 & 0 & R_s & 0 & 0 & 0 \\ 0 & 0 & 0 & R_s & 0 & 0 \\ 0 & 0 & 0 & 0 & R_s & 0 \\ 0 & 0 & 0 & 0 & 0 & R_s \end{bmatrix} \quad (2.21)$$

The state matrix is determined by:

$$\mathbf{A} = -\mathbf{\Gamma}^{-1}\mathbf{R}^{-1} \quad (2.22)$$

and the input matrices are given by:

$$\mathbf{B} = \mathbf{\Gamma}^{-1} \quad (2.23)$$

$$\mathbf{F} = -\mathbf{\Gamma}^{-1} \quad (2.24)$$

The output matrix is defined as:

$$\mathbf{C} = \begin{bmatrix} 1 & 0 & 0 & 0 & 0 & 0 \\ 0 & 1 & 0 & 0 & 0 & 0 \\ 0 & 0 & 1 & 0 & 0 & 0 \\ 0 & 0 & 0 & 1 & 0 & 0 \\ 0 & 0 & 0 & 0 & 1 & 0 \\ 0 & 0 & 0 & 0 & 0 & 1 \end{bmatrix} \quad (2.25)$$

Denoting the disturbance of the system as $\boldsymbol{\xi} \in \mathfrak{R}^n$ and adding it to the model, the system can be rewritten as:

$$\begin{cases} \dot{\mathbf{x}} = \mathbf{A}\mathbf{x} + \mathbf{B}\mathbf{u} + \mathbf{F}\mathbf{e} + \boldsymbol{\xi}(\mathbf{x}, \mathbf{u}, \mathbf{e}, \mathbf{t}) \\ \mathbf{y} = \mathbf{x} \end{cases} \quad (2.26)$$

In this work, a scenario where the disturbances are composed by parameter uncertainties and by non-idealities of the system is considered. The non-idealities are basically related to the back-emf. The parameter uncertainties represent the variation in the stator resistance, in the self- and in the mutual inductances during the operation — these are not considered in the nominal model represented by (2.16). The back-emf non-idealities and the magnetic coupling between the phases will be described in a posteriorly section.

2.2.4. Discrete time state-space model of the six-phase BLDC machine

The discrete dynamic model of the machine is intended to the study of control techniques based on the sliding mode design and disturbance observers in discrete time domain. These techniques are applied to the six-phase brushless DC machine in order to overcome the disturbance added to the system, thereby ensuring a good performance of the system where the model is not exactly known.

Applying the Euler method for the discretization of (2.26) results in:

$$\begin{cases} \mathbf{x}(k+1) = (\mathbf{I} + \mathbf{A}t_s)\mathbf{x}(k) + \mathbf{B}t_s\mathbf{u}(k) + \mathbf{F}t_s\mathbf{e}(k) + \boldsymbol{\xi}t_s(k) \\ \mathbf{y}(k) = \mathbf{x}(k) \end{cases} \quad (2.27)$$

where t_s is the sampling time. And it can be rewritten as:

$$\begin{cases} \mathbf{x}(k+1) = \mathbf{G}\mathbf{x}(k) + \mathbf{H}\mathbf{u}(k) + \mathbf{W}\mathbf{e}(k) + \boldsymbol{\xi}_d(k) \\ \mathbf{y}(k) = \mathbf{x}(k) \end{cases} \quad (2.28)$$

where $\boldsymbol{\xi}_d$ represents the non-idealities and uncertainties intrinsic to the discrete time model.

This work considers the non-idealities and uncertainties as disturbances added to the nominal model.

2.2.5. Measurement of self- and mutual inductances

Due to the machine design, there is mutual coupling between the phases. Moreover, the self- and mutual inductances have nonlinear characteristics and are not constant as they depend on the rotor position and the current variation.

To get a better knowledge of the machine parameters, the dependence on the rotor angle at no-load of the self- and mutual inductances from one winding to the other five windings was measured, as shown in Figure 2.9. The self- and the mutual inductances of each phase were measured with a LCR meter (Wayne Kerr) at each 15 mechanical degree.

Figure 2.9 presents the mutual inductances between the phases. It should be noted that this measurement represents an approximated model. Although the variations in self- and mutual inductances, depending on rotor position, are measured, they are not enough to accurately describe the model. This is because such variations are also current-dependent and current variations are not considered for this measurement.

The fact that the model is only approximately known and is very complex to build an accurate model which describes exactly the machine, is a challenge for the control strategy that seeks to obtain a torque with minimal oscillations, despite the effect of the mutual inductances in the phase currents.

2.2.6. Measurement of back-emf

The ideal back-emf waveform in the BLDC machine is trapezoidal, as shown in Figure 2.7, however due to machine design the back-emf is non-ideal with oscillations in the crest of the waveform, where it should be constant.

To obtain the real back-emf waveform and measure the back-emf factor, a measurement of the no-load phase voltage for different speeds from zero until the rated speed is carried out. According to (2.12), it is possible to calculate the back-emf factor with the back-emf amplitude E and with the measured speed in rad/s . An average of these measurements is calculated, which gives the value 0.0198 Vs/rad for the back-emf factor, as shown in Table 2.2.

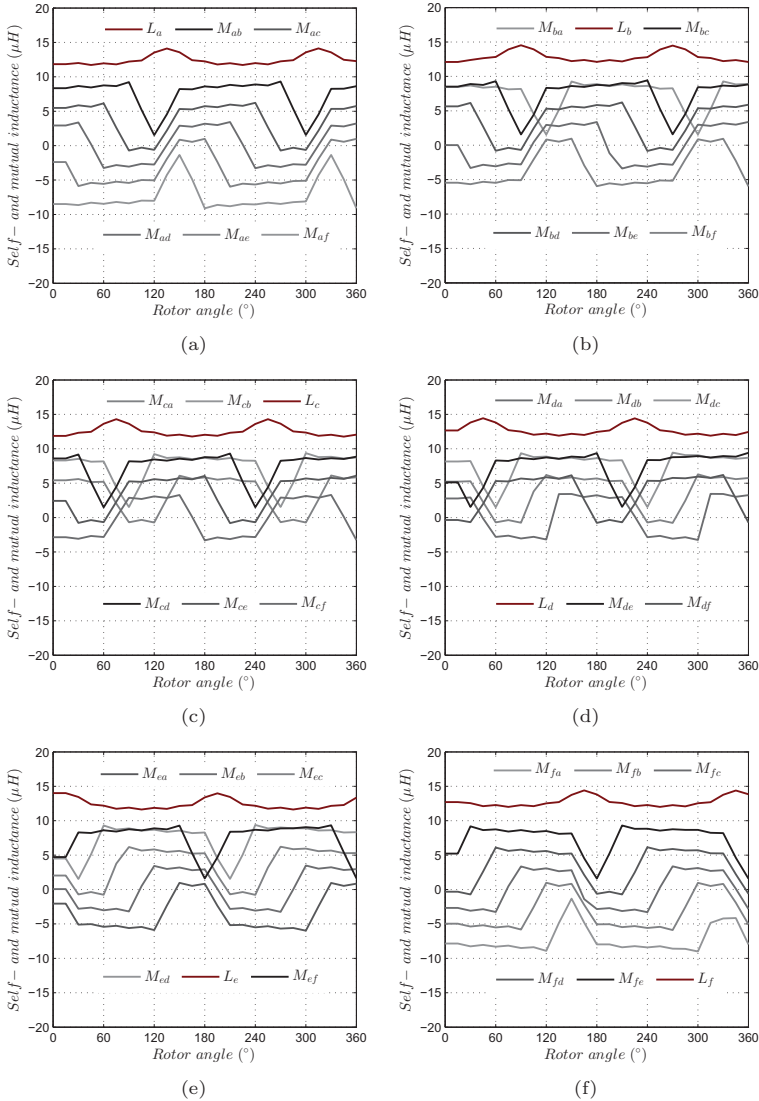


Figure 2.9.: (a) Self- and mutual inductances from phase A as a function of the rotor position, (b) self- and mutual inductances from phase B as a function of the rotor position, (c) self- and mutual inductances from phase C as a function of the rotor position, (d) self- and mutual inductances from phase D as a function of the rotor position. (e) self- and mutual inductances from phase E as a function of the rotor position. (f) self- and mutual inductances from phase F as a function of the rotor position.

2. Modelling of six-phase brushless DC machine

RPM	rad/s	Back-emf amplitude (E)	Back-emf factor (K_e)
400	41.8879	0.85	0.0203
600	62.8319	1.24	0.0197
700	73.3038	1.45	0.0198
800	83.7758	1.65	0.0197
900	94.2478	1.85	0.0196
2250	235.6194	4.7	0.0199
			0.01984286

Table 2.2.: Measurement of back-emf.

Figure 2.10 illustrates the linear dependence between the back-emf and the speed, where the inclination of the curve represents the back-emf factor.

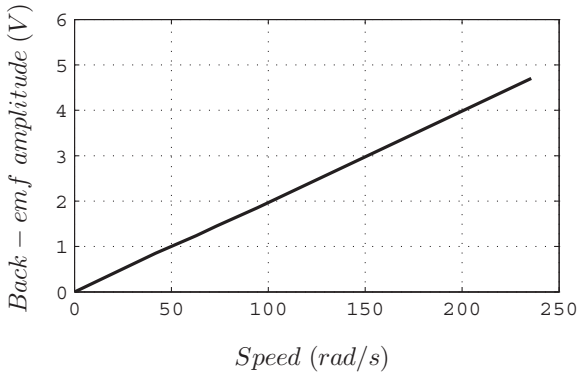


Figure 2.10.: Speed versus back-emf measurement for the back-emf factor determination.

Figure 2.11 shows the measured back-emf waveform for three of the six phases at the rated speed.

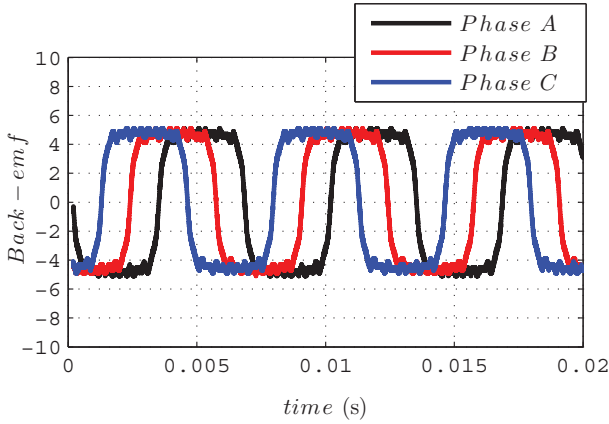


Figure 2.11.: Experimental back-emf from phase A, B and C of the six-phase BLDC motor at 2250 rpm.

From Figure 2.11 it is possible to verify that the back-emf is non-ideally trapezoidal and has oscillations in the crest of the waveform. The non-idealities of the back-emf are intrinsic to the machine design and affect the performance of the controller, thus contributing to the torque oscillations.

2.2.7. Summary

The particularities of the six-phase brushless DC model are presented in this chapter. A general concept of the permanent magnet motors and a comparison with the other machines have been provided here. The aim of the following chapter is to investigate the current control strategies that ensure a high performance operation of the machine with minimal torque oscillations under conditions of parameter uncertainties and strong magnetic coupling between the phases.

3. Current control strategies applied to the brushless DC machine

3.1. Introduction

Different control strategies have been considered for improving the performance of BLDC motors. The proportional-integral controller and hysteresis current control have been the most widely used control techniques for controlling the BLDC motor [17, 26, 47, 48]. However, the main drawback is the linear nature of classical PI controller that lacks robustness when facing an operation scenario where parameter variations and disturbances are added to the nominal model [49, 50].

To circumvent this problem and improve the BLDC response, this chapter proposes an investigation of robust controllers which are based on the sliding mode approach and developed in discrete time domain. The sliding mode control is an appropriate tool for solving problems of a nonlinear nature and overcomes the fact that the model is not exactly known.

The proposed current controllers are applied to the six-phase BLDC machine and described in state-space, considering the model in phase variable coordinates. This chapter will present firstly a classical proportional-integral current controller. Next, the main concepts of the sliding mode control theory will be introduced in order to provide a background to the development of the discrete time sliding mode control. Two discrete time sliding mode algorithms will be presented as well as their stability proof. Lastly, simulation results demonstrate the performance of controllers.

Usually, a cascade control structure is adopted for BLDC control. An external loop executes the speed control. The output of the speed controller, which acts as an input to the current controller, generates the current

reference for the six inner current controllers. The output of each current controller provides the duty cycle which will be used in the modulation to generate the PWM output signals to be applied through the six independent H-Bridges. The speed measurement is calculated from the Hall sensor period of each phase that represents the electrical period of the machine.

Figure 3.1 shows the proposed control diagram for the six-phase BLDC motor

3.2. Proportional-integral current controller

Proportional-integral is the most used control technique for current regulation in BLDC motors and hence its application in the six-phase brushless DC machine is presented in this work.

The control is developed in a phase variable model. Therefore, in each phase, one PI controller independent of the other phases is used in order to regulate the phase current, while one PI controller is used in the external loop to control the speed. The method to calculate the current and speed controller gains based on the bandwidth of the closed-loop system is shown in Appendices A.1 and A.2, respectively.

A simplified model for the electric dynamic of the BLDC machine, without the mutual inductances is considered in the design of PI current controller gains. The mutual inductances are treated as disturbances of the system.

Aiming to simplify the control, a compensation of the back-emf is carried out by a feedforward control. The amplitude of the back-emf is calculated by the measured speed, according to (2.12) and added to the output of the current PI controller. There is the possibility that the back-emf can only be partially cancelled by the feedforward control since just a constant value for the back-emf amplitude is calculated. If it is non-ideal with oscillations in the crest, this will not be compensated.

The proportional-integral current controller in a discrete time domain is defined by:

$$\begin{aligned}\mathbf{u}(k) &= \mathbf{emf}(k) + K_{Pdv} (\mathbf{y}^*(k) - \mathbf{y}(k)) + K_{Idv} \mathbf{x}_c(k-1) \\ \mathbf{x}_c(k) &= (\mathbf{y}^*(k) - \mathbf{y}(k)) + \mathbf{x}_c(k-1)\end{aligned}\quad (3.1)$$

where \mathbf{emf} represents the feedforward control and K_{Pdv} and K_{Idv} are the controller gains. The block diagram of the current control loop for one phase of the BLDC machine is shown in Figure 3.2.

Although PI control is well settled for the brushless DC machine, its poor robustness against parameter variations and model uncertainties does not ensure a good performance when the system model is not well known. This is the case of the six-phase brushless DC machine model presented in this work, which has the mutual inductance and the back-emf non-idealities as unknown parameters that are treated as disturbances added to the system.

In order to obtain an acceptable dynamic response over the whole operation range, the PI controller gains must be carefully tuned and adjusted again when an operation point is changed. Furthermore, owing to the limited bandwidth of the conventional classical PI control, a greater parameter variation may lead the control to instability.

The response of the six-phase BLDC machine to the PI current control has been simulated and will be posteriorly presented in this chapter.

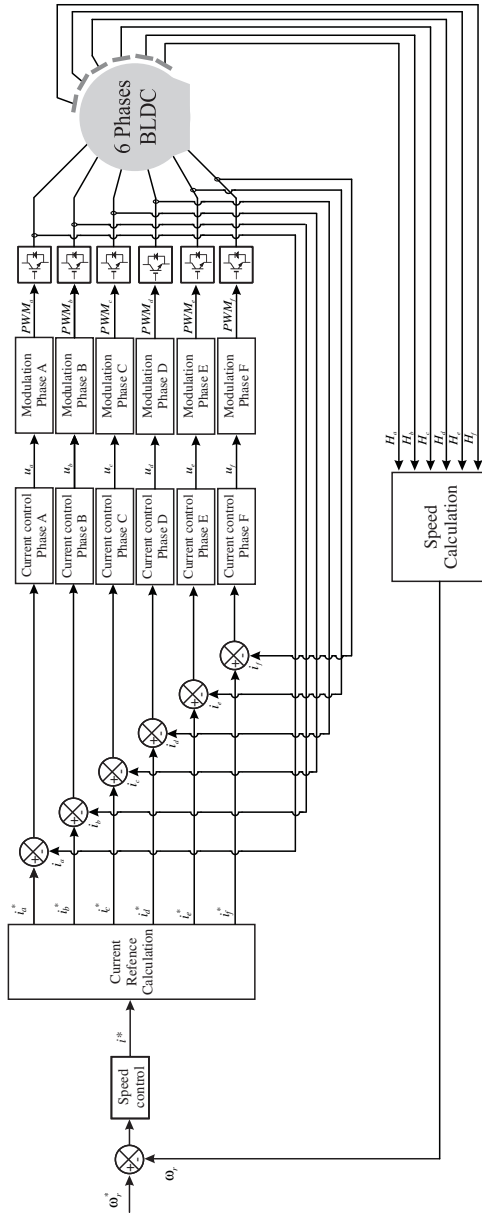


Figure 3.1.: Block diagram of the BLDC machine.

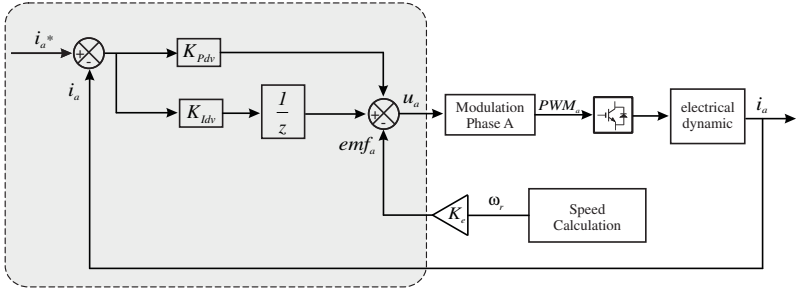


Figure 3.2.: Block diagram of PI current control with feedforward control for one phase of the multiphase BLDC machine.

3.3. Continuous time sliding mode controller

The sliding mode control (SMC) is a kind of variable structure control that changes its structure from one function to another in accordance with a switching function. The theory of continuous time sliding mode control and variable structure are deeply discussed in [12, 51, 52].

The study of sliding mode control started with Emelyanov in the 50s. Since then, the sliding mode is being used in different applications such as nonlinear, multivariable, discrete or stochastic systems. With the technological advance of the microprocessors and the circuits with high switching frequency, it has become possible to implement the SMC in several applications such as robot control, underwater vehicles, high-performance electric motors and aircraft control, among others [10].

Beyond the simple control design, the main property of this technique is its robustness or insensitivity to model uncertainties and external disturbances. Better than the robustness is its invariance property, found in the continuous time sliding mode control.

The sliding mode satisfies the invariance definition when the system is insensitive to parameters uncertainties and external disturbances applied to the nominal plant. In other words, the system trajectory in the sliding mode does not depend on the plant parameters [10].

In this work, the continuous time sliding mode is presented in order to provide a theoretical background of the sliding mode control and thus to aid the development of the discrete time sliding mode theory in the next section.

Essentially, the SMC uses a discontinuous control law with high-frequency switching control to orientate the system trajectory to a determined region in the state-space called sliding surface and remain it there for the subsequent time [51].

Considering a dynamic system such as represented by equation (2.16), the discontinuous feedback is given by:

$$u_i = \begin{cases} u_i^+(t,x), & \text{if } \sigma_i > 0 \\ u_i^-(t,x), & \text{if } \sigma_i < 0 \end{cases} \quad i = 1,2,\dots,m \quad (3.2)$$

where σ_i represents the i^{th} sliding surface.

The aim is to design a controller that carries the dynamic system to track the output control references. The design of the sliding mode control law is divided into two steps:

- I. Sliding surface design: the design of a sliding mode surface that represents a desired system dynamics and allows it, when in the sliding condition, to achieve the reference tracking.
- II. Controller design: the design of a discontinuous control law that satisfies the existence and reachability of the sliding modes in such a manner that any state outside the sliding surface is driven to reach the surface in finite time and remain there.

3.3.1. Sliding surface design

The sliding surface is projected so that the system in the surface $\sigma(x,t) = 0$ has a desirable behavior. In this case, the control problem is that the output tracks a predefined reference output.

Considering a sliding surface:

$$\sigma(x,t) = \begin{bmatrix} \sigma_1 & \sigma_2 & \dots & \sigma_m \end{bmatrix}^T \quad (3.3)$$

that is continuously differentiable. The design of each element of σ , for a system with relative degree equal one¹ [53], is done by the following equation:

$$\sigma_i = c(y_i - y_i^*) \quad i = 1, 2, \dots, m \quad (3.4)$$

where y_i is the output, y_i^* is the output reference, and c is a gain. When the system is in the sliding condition with $\sigma_i = 0$, (3.4) represents a linear dynamic of the output tracking error that converges to the origin.

Once the system is on the sliding surface ($\sigma_i = 0$), it becomes invariant against external disturbances, model uncertainties and parametric variations.

Considering the system described by equation (2.16) with order $n = 2$. The sliding surface behavior can be illustrated as a line in the phase plane with slope $-c$, as shown in Figure 3.3.

An ideal sliding mode, where the system follows exactly over the sliding surface ($\sigma = 0$), as represented in Figure 3.3, exists only when the state trajectory $\mathbf{x}(t)$ of the controlled plant satisfies $\sigma[\mathbf{x}(t)] = 0$ at every $t > t_0$ for some t_0 [11]. It requires that the control law switches instantly with infinite frequency, which is impracticable in real systems due to the inertias of actuators and sensors. It is more realistic to assume that the control law switches with a high finite frequency. As a consequence, the sliding motion oscillates in the neighbourhood of the sliding surface, as shown in Figure 3.4. This phenomenon, known as chattering, is inherent to the discontinuous control and is the major drawback in the sliding mode approach, since it may excite non-modelled dynamics and leads the system to instability [11–13, 54–57].

Techniques to mitigate or eliminate the chattering will be presented in a later section of this chapter.

¹When the relative degree of the output is one ($rd = 1$), it means that the control action appear explicitly in the first time derivative of the sliding surface.

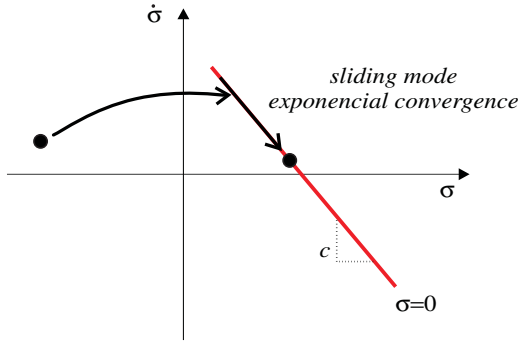


Figure 3.3.: Illustration of the sliding surface behavior.

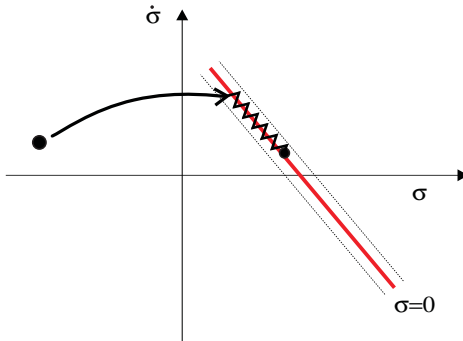


Figure 3.4.: Illustration of the chattering sliding surface behavior.

For the sake of simplicity, for the six-phase brushless DC machine sliding surface design, the parameter c will be considered equal 1 ($c = 1$). So considering the state-space BLDC model represented in (2.26), the sliding surface is defined in accordance with (3.4) as:

$$\sigma = [(\mathbf{y} - \mathbf{y}^*)]^T = \begin{bmatrix} \sigma_a & \sigma_b & \sigma_c & \sigma_d & \sigma_e & \sigma_f \end{bmatrix}^T = 0 \quad (3.5)$$

where \mathbf{y}^* represents the output reference vector and is given by:

$$\mathbf{y}^* = \left[i_a^* \quad i_b^* \quad i_c^* \quad i_d^* \quad i_e^* \quad i_f^* \right]^T \quad (3.6)$$

In this case, the sliding surface represents the dynamic of the phase current error which characterizes the control purpose that is to carry the current tracking error to zero.

3.3.2. Control law design

The control law design is based on the method of equivalent control approach, proposed by Utkin [58].

Considering the state-space BLDC model represented in (2.26) and assuming that the sliding surface has been designed in accordance with (3.4), the next step is to design a variable structure control in such a manner that any state outside the sliding surface is driven to reach the surface in finite time.

The control action \mathbf{u} is designed to bring the sliding surface σ to zero in a finite time and then to keep it there for all future time. The structure of the control is given by:

$$\mathbf{u} = \mathbf{u}_{\text{eq}} + \mathbf{u}_{\text{n}} \quad (3.7)$$

where \mathbf{u}_{eq} is the equivalent control component and represents the continuous component of the control, and \mathbf{u}_{n} is the discontinuous component.

The sliding surface dynamic equation is defined as:

$$\dot{\sigma} = \dot{\mathbf{y}} - \dot{\mathbf{y}}^* = \dot{\mathbf{x}} - \dot{\mathbf{x}}^* \quad (3.8)$$

The equivalent control is determined by assuming that all uncertainties are zero and that $\dot{\sigma} = 0$ is necessary to maintain the state trajectory on the sliding surface $\sigma = 0$.

Replacing (2.26) into (3.8):

$$\dot{\sigma} = (\mathbf{A}\mathbf{x} + \mathbf{B}\mathbf{u} + \mathbf{F}\mathbf{e} + \boldsymbol{\xi}) - \dot{\mathbf{x}}^* = 0 \quad (3.9)$$

Hence, solving (3.9) and considering $\xi = 0$, the equivalent control can be defined as:

$$\mathbf{u}_{eq} = (\mathbf{B})^{-1} (\dot{\mathbf{x}}^* - \mathbf{A}\mathbf{x} - \mathbf{F}\mathbf{e}) \quad (3.10)$$

where \mathbf{B} is non-singular for all time in the domain of interest.

To define the discontinuous control, the uncertainties must be accounted to the system. Under the assumption that ξ is limited, it is possible to design \mathbf{u}_n by choosing an appropriate Lyapunov function candidate in order to force the sliding surface to zero in accordance with the equation:

$$\mathbf{u}_n = (\mathbf{B})^{-1} (-K \text{sign}(\sigma)) \quad (3.11)$$

where $\text{sign}(\sigma)$ represents the sign function and $K > \|\xi(x,u,t)\|$.

Knowing the equivalent control and the discontinuous control term, it is possible to define the sliding mode control law as:

$$\mathbf{u} = (\mathbf{B})^{-1} (\dot{\mathbf{x}}^* - \mathbf{A}\mathbf{x} - \mathbf{F}\mathbf{e} - K \text{sign}(\sigma)) \quad (3.12)$$

Now, substituting (3.12) into (3.9), the sliding mode dynamics can be described as:

$$\dot{\sigma} = (\mathbf{A}\mathbf{x} + \mathbf{B} [(\mathbf{B})^{-1} (\dot{\mathbf{x}}^* - \mathbf{A}\mathbf{x} - \mathbf{F}\mathbf{e} - K \text{sign}(\sigma))] + \mathbf{F}\mathbf{e} + \xi) - \dot{\mathbf{x}}^* \quad (3.13)$$

$$\dot{\sigma} = -K \text{sign}(\sigma) + \xi \quad (3.14)$$

It should be noticed that the equivalent control component simplifies the system by cancelling the known terms from the nominal model and the discontinuous control term is responsible for overcoming the uncertainties of the system.

3.3.3. Stability proof of continuous time sliding mode

The second method of Lyapunov provides a natural setting for the sliding mode control stability analysis. Considering the following Lyapunov function candidate:

$$V(\boldsymbol{\sigma}) = \boldsymbol{\sigma}^T \mathbf{P} \boldsymbol{\sigma} \quad (3.15)$$

where \mathbf{P} is an identity matrix.

The derivative of V along the trajectories of $\boldsymbol{\sigma}$ is given by:

$$\dot{V}(\boldsymbol{\sigma}) = (\dot{\boldsymbol{\sigma}}^T \mathbf{P} \boldsymbol{\sigma}) + (\boldsymbol{\sigma}^T \mathbf{P} \dot{\boldsymbol{\sigma}}) \quad (3.16)$$

The stability of the system is proven if the negativity of V derivative is ensured.

Now, substituting (3.9) into (3.16):

$$\begin{aligned} \dot{V}(\boldsymbol{\sigma}) = & ((\mathbf{A}\mathbf{x} + \mathbf{F}\mathbf{e} + \mathbf{B}\mathbf{u} + \boldsymbol{\xi} - \dot{\mathbf{x}}^*)^T \mathbf{P} \boldsymbol{\sigma}) + \\ & + (\boldsymbol{\sigma}^T \mathbf{P} (\mathbf{A}\mathbf{x} + \mathbf{F}\mathbf{e} + \mathbf{B}\mathbf{u} + \boldsymbol{\xi} - \dot{\mathbf{x}}^*)) \end{aligned} \quad (3.17)$$

and the control law given in (3.12) into (3.17):

$$\begin{aligned} \dot{V}(\boldsymbol{\sigma}) = & ((\mathbf{A}\mathbf{x} + \mathbf{F}\mathbf{e} + \dot{\mathbf{x}}^* - \mathbf{A}\mathbf{x} - \mathbf{F}\mathbf{e} - K \text{sign}(\boldsymbol{\sigma}) + \boldsymbol{\xi} - \dot{\mathbf{x}}^*)^T \mathbf{P} \boldsymbol{\sigma}) + \\ & + (\boldsymbol{\sigma}^T \mathbf{P} (\mathbf{A}\mathbf{x} + \mathbf{F}\mathbf{e} + \dot{\mathbf{x}}^* - \mathbf{A}\mathbf{x} - \mathbf{F}\mathbf{e} - K \text{sign}(\boldsymbol{\sigma}) + \boldsymbol{\xi} - \dot{\mathbf{x}}^*)) \end{aligned} \quad (3.18)$$

$$\dot{V}(\boldsymbol{\sigma}) = ((-K \text{sign}(\boldsymbol{\sigma}) + \boldsymbol{\xi})^T \mathbf{P} \boldsymbol{\sigma}) + (\boldsymbol{\sigma}^T \mathbf{P} (-K \text{sign}(\boldsymbol{\sigma}) + \boldsymbol{\xi})) \quad (3.19)$$

(3.19) can be rewritten as:

$$\dot{V}(\boldsymbol{\sigma}) = -2K S_1 + 2S_2 \quad (3.20)$$

where:

$$S_1 = \left(\begin{array}{l} \sigma_a \text{sign}(\sigma_a) + \sigma_b \text{sign}(\sigma_b) + \sigma_c \text{sign}(\sigma_c) + \\ + \sigma_d \text{sign}(\sigma_d) + \sigma_e \text{sign}(\sigma_e) + \sigma_f \text{sign}(\sigma_f) \end{array} \right) \quad (3.21)$$

$$S_2 = \xi_a \sigma_a + \xi_b \sigma_b + \xi_c \sigma_c + \xi_d \sigma_d + \xi_e \sigma_e + \xi_f \sigma_f \quad (3.22)$$

The mathematical development of (3.19) to get to (3.20) is given in Appendix B.1.

Considering that:

$$-2KS_1 + 2S_2 < 0 \quad (3.23)$$

It results in:

$$K > S_2 S_1^{-1} \quad (3.24)$$

The negativity of \dot{V} is ensured if the condition given in (3.24) is satisfied, which means that the attractiveness of the sliding surface is guaranteed by keeping the system trajectories on the surface, since to leave the surface a positive derivative of V is required.

Taking the condition $\sigma=0$, it is possible to obtain the relationship between \mathbf{y} and \mathbf{y}^* by replacing the control \mathbf{u} in (2.26), as shown below:

$$\begin{cases} \dot{\mathbf{x}} = \mathbf{Ax} + \mathbf{B} \left((\mathbf{B})^{-1} (\dot{\mathbf{x}}^* - \mathbf{Ax} - \mathbf{Fe} - K \text{sign}(\sigma)) \right) + \mathbf{Fe} + \boldsymbol{\xi} \\ \mathbf{y} = \mathbf{x} \end{cases} \quad (3.25)$$

Considering that:

$$\dot{\mathbf{y}} = \dot{\mathbf{x}} \quad (3.26)$$

Replacing (3.25) into (3.26):

$$\dot{\mathbf{y}} = \mathbf{Ax} + \mathbf{B} \left((\mathbf{B})^{-1} (\dot{\mathbf{x}}^* - \mathbf{Ax} - \mathbf{Fe} - K \text{sign}(\sigma)) \right) + \mathbf{Fe} + \boldsymbol{\xi} \quad (3.27)$$

with $\sigma=0$ it becomes:

$$\dot{\mathbf{y}} = \dot{\mathbf{x}}^* + \boldsymbol{\xi} \quad (3.28)$$

which equals to:

$$\dot{\mathbf{y}} = \dot{\mathbf{y}}^* + \boldsymbol{\xi} \quad (3.29)$$

Assuming that $\boldsymbol{\xi}=0$:

$$\dot{\mathbf{y}} = \dot{\mathbf{y}}^* \quad (3.30)$$

According to the previous equation, when $\boldsymbol{\sigma}=0$ and $\boldsymbol{\xi}=0$, the output system has the same dynamics from the reference.

3.3.4. Chattering

The main drawback of the sliding mode approach is the chattering effect that appears due to the limited sampling frequency of the system, the delay in the control law calculations and the inertia of the actuators. This effect is negative and can result in oscillations with significant amplitude that excites non-modelled dynamics in the system. Moreover, the chattering decreases the lifetime of the actuator and components. Some approaches have been developed to eliminate or to reduce the chattering [13, 59].

The more common way to reduce the chattering is the continuation approach [13, 60] on the basis of a substitution to the discontinuous control in the neighbourhood of the sliding surface by a continuous control or a dead zone which is called boundary layer.

The discontinuous control will be applied just when the system trajectory is out of the region limited by $\pm\vartheta$, as shown in Figure 3.5.

In a classic sliding mode control, the discontinuous control is implemented by using the sign function. The use of boundary layer involves alteration of the control structure and it is, therefore, necessary to define new mathematical functions that would allow the use of the continuation approach. Thus, two switching functions for the continuation approach are defined: the saturation function and the dead zone. Hereafter, the sign function, as well as the functions for the boundary layer, is presented.

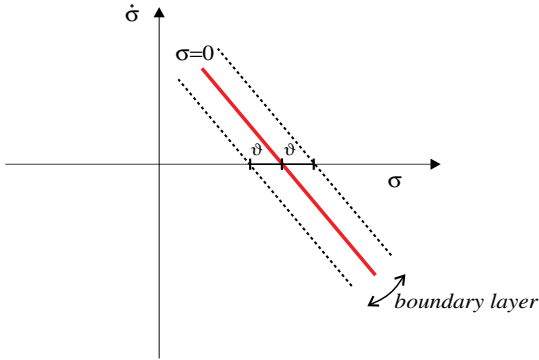


Figure 3.5.: Boundary layer.

a. Sign Function

With the sign function, the invariance property is maintained. The sign function takes the sign of the sliding surface and is defined below:

$$\text{sign}(\sigma) = \begin{cases} 1 & \sigma(x,t) > 0 \\ 0 & \sigma(x,t) = 0 \\ -1 & \sigma(x,t) < 0 \end{cases} \quad (3.31)$$

The sign function is represented in Figure 3.6:

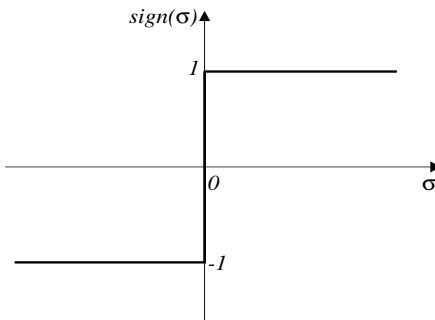


Figure 3.6.: Sign function.

b. Continuation approach: saturation function

The saturation function is given by:

$$sat(\sigma) = \begin{cases} 1 & -\vartheta < \sigma(x,t) \\ \frac{\sigma}{\vartheta} & -\vartheta \leq \sigma(x,t) \leq \vartheta \\ -1 & \sigma(x,t) > \vartheta \end{cases} \quad (3.32)$$

where ϑ defines the boundary layer. The sign function acts outside the boundary layer and inside it acts a linear function, as shown in Figure 3.7.

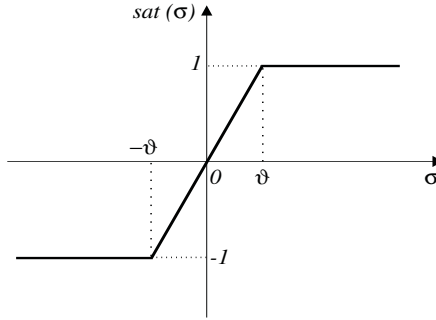


Figure 3.7.: Chattering reduction: saturation function.

c. Continuation approach: dead zone

With the dead zone, the sign function acts outside the boundary layer while inside it does not act the discontinuous control, as shown in Figure 3.8. The function that introduces a dead zone inside the boundary layer is given by:

$$sat(\sigma) = \begin{cases} 1 & -\vartheta < \sigma(x,t) \\ 0 & -\vartheta \leq \sigma(x,t) \leq \vartheta \\ -1 & \sigma(x,t) > \vartheta \end{cases} \quad (3.33)$$

According to [13], the chattering does not exist on the boundary layer. However, the invariance property is lost, but the system is still robust

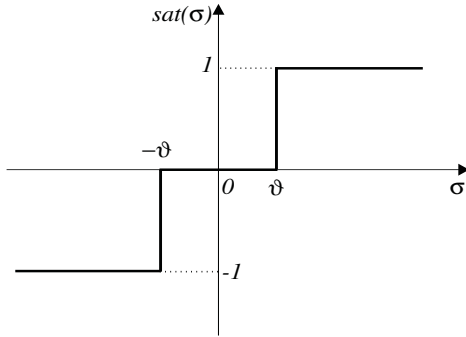


Figure 3.8.: Chattering reduction: dead zone function.

concerning the disturbance and uncertainties if the boundary layer is sufficiently small. The boundary layer width implies a compromise between the precision and chattering reduction.

Another way to eliminate the chattering effect, without loss robustness and precision, is the high-order sliding mode approach [13, 61, 62]. The principal idea is to consider the discontinuity introduced by the control in high-order dynamics, instead of the first-order dynamics. A second-order sliding mode with the super-twisting algorithm will be presented posteriorly in this chapter.

This section presented the basic concepts of the sliding mode. The theoretical background of the continuous time sliding mode control is widely presented and well established in the literature. This kind of control is inherent a continuous time technique and it requires that the discontinuous part of the control works with high frequency to lead the system to the sliding surface and keep it there. However, the implementation and control of most systems are nowadays based on using digital microcontrollers (such as DSPs and FPGAs), which encumbers the application of the continuous time sliding mode control as the limited sampling rate deteriorates the response of the discontinuous control and may lead the system to instability. It must be taken in consideration that the stability proofs of the continuous time sliding mode control are not valid in case of discrete implementation.

For this reason, a discrete time formulation of the sliding mode control will be presented in the next section.

3.4. Discrete time sliding mode controller

The practical engineering constraints of the continuous time sliding mode control and the development of microprocessors that facilitate the implementation of discrete time techniques constituted a motivation to start the studies about the discrete time sliding mode control. The study of the discrete time sliding mode starts with the study of Milosavljevic [63]. After that, important contributions to the development and consolidation of the discrete time sliding mode control appeared [15, 64–67].

The mere discretization of the continuous time sliding mode formulation is not sufficient to define a discrete time sliding mode [63]. The proofs of the continuous time sliding mode stability are not valid in the discrete time domain and therefore the control is updated just at each sampling time — the discontinuous control part changes its state with a limited sampling rate which deteriorates the robustness of the system and can lead it to instability [68]. Due to these factors, an appropriate sliding mode design based on discrete mathematical tools is needed. For the controller design, the continuous plant to be controlled should also have its dynamics represented in the discrete time domain.

The procedure to design the discrete time sliding mode control has two steps. First, the sliding surface is designed and then the control design is established. This procedure is similar to the one used to the continuous time sliding mode control design. However, to ensure the stability of a system in the discrete time sliding mode, the reaching condition must be modified in relation to continuous time.

Considering that the control law can be changed just at sampling instants, an ideal sliding mode does not occur in a discrete system. However, the closed loop control moves around the sliding surface in a quasi-sliding mode band. Hence, the invariance property is lost in the discrete time sliding mode control. However, significant robustness is maintained, which means

that the system is even able to withstand uncertainties and disturbances added to the model.

Different reaching laws to the sliding mode design in discrete time systems have been developed and are presented in the literature.

The reaching law proposed by [66] ensures necessary and sufficient conditions obtained from the Lyapunov stability analysis to ensure a stable convergence. The condition is defined by:

$$|\sigma_i(k+1)| < |\sigma_i(k)| \quad (3.34)$$

Considering the discrete time sliding surface as a Lyapunov candidate:

$$V(k) = \sigma^2(k) \quad (3.35)$$

$$\Delta V(k) = \sigma^2(k+1) - \sigma^2(k) \quad (3.36)$$

$$\Delta V(k) = (\sigma(k+1) + \sigma(k))(\sigma(k+1) - \sigma(k)) \quad (3.37)$$

Multiplying (3.37) by $sign(\sigma)$,

$$\Delta V(k) = (\sigma(k+1) + \sigma(k))(\sigma(k+1) - \sigma(k))(sign(\sigma(k))) \quad (3.38)$$

Condition (3.34) can be divided into two inequalities:

$$(\sigma(k+1) - \sigma(k))(sign(\sigma(k))) < 0 \quad (3.39)$$

$$(\sigma(k+1) + \sigma(k))(sign(\sigma(k))) \geq 0 \quad (3.40)$$

where the inequality (3.39) represents the necessary condition and inequality (3.40) represents the sufficient condition in relation to the existence of a discrete time sliding surface. These conditions define the upper and lower limits of the control law, which is different to the stability analysis

in continuous time where just one limit is established to the control law, as shown in 3.24.

The study [15] presents a discrete reaching law where it is required that the state trajectory would cross the sliding surface at every sampling instant by defining a quasi-sliding mode band around the surface.

The papers [67] and [69] propose a reaching law where it is not necessary that the system should cross the sliding surface in each control step and just needs to remain in a small band around it. In this case, the control strategy can be linear, avoiding the chattering effect caused by the discontinuous control part.

This work follows the reaching law approach developed by [15] in which the state trajectory should present the following properties in order to define a discrete time sliding mode and the reaching condition:

- a. *Starting from any initial state, the trajectory will move monotonically around the switching plane and cross it in finite time.*
- b. *Once the trajectory has crossed the switching plane for the first time, it will cross the plane again in every successive sampling period, resulting in a zigzag motion about the switching plane.*
- c. *The size of each successive zigzag step does not increase and the trajectory stays within a specified band.*

If the controlled systems satisfy these properties, given in [15], they are designed in a quasi-sliding mode. From this point, it is possible to design a discrete control law.

3.4.1. Discrete time sliding mode controller using Gao's approach applied to the six-phase BLDC machine

The design of the discrete time control law applied to the six-phase BLDC machine is presented in this section.

Considering that the sliding surface is defined as:

$$\sigma(k) = (\mathbf{y}(k) - \mathbf{y}^*(k)) = (\mathbf{x}(k) - \mathbf{x}^*(k)) \quad (3.41)$$

and according to [15], the reaching law is given by:

$$\boldsymbol{\sigma}(k+1) - \boldsymbol{\sigma}(k) = -qt_s\boldsymbol{\sigma}(k) - \varepsilon t_s \text{sign}(\boldsymbol{\sigma}(k)) \quad (3.42)$$

with $\varepsilon > 0$, $q > 0$, $1 - qt_s > 0$.

Substituting (3.41) into (3.42):

$$-qt_s\boldsymbol{\sigma}(k) - \varepsilon t_s \text{sign}(\boldsymbol{\sigma}(k)) = \mathbf{x}(k+1) - \mathbf{x}^*(k+1) + \mathbf{x}^*(k) - \mathbf{x}(k) \quad (3.43)$$

Replacing (2.28) into (3.43), the following control law is achieved:

$$\mathbf{u}(k) = (\mathbf{H})^{-1} \begin{bmatrix} \mathbf{x}^*(k+1) - \mathbf{x}^*(k) + \mathbf{x}(k) - \mathbf{G}\mathbf{x}(k) - \\ -\mathbf{W}\mathbf{e}(k) - qt_s\boldsymbol{\sigma}(k) - \varepsilon t_s \text{sign}(\boldsymbol{\sigma}(k)) \end{bmatrix} \quad (3.44)$$

In order to obtain the response of the system to the developed controller, the control law gives in (3.44) is replaced into (2.28) and it becomes:

$$\begin{aligned} \mathbf{x}(k+1) &= \mathbf{G}\mathbf{x}(k) + \mathbf{W}\mathbf{e}(k) + \boldsymbol{\xi}_d(k) + \\ &+ \mathbf{H} \left((\mathbf{H})^{-1} \begin{bmatrix} \mathbf{x}^*(k+1) - \mathbf{x}^*(k) + \mathbf{x}(k) - \mathbf{G}\mathbf{x}(k) - \mathbf{W}\mathbf{e}(k) + \\ -qt_s\boldsymbol{\sigma}(k) - \varepsilon t_s \text{sign}(\boldsymbol{\sigma}(k)) \end{bmatrix} \right) \end{aligned} \quad (3.45)$$

According to the discrete state-space model given in (2.28), it is possible to write:

$$\mathbf{y}(k+1) = \mathbf{x}(k+1) \quad (3.46)$$

Replacing (3.45) into (3.46):

$$\begin{aligned} \mathbf{y}(k+1) &= \mathbf{G}\mathbf{x}(k) + \mathbf{W}\mathbf{e}(k) + \boldsymbol{\xi}_d(k) + \\ &+ \mathbf{H} \left((\mathbf{H})^{-1} \begin{bmatrix} \mathbf{x}^*(k+1) - \mathbf{x}^*(k) + \mathbf{x}(k) - \mathbf{G}\mathbf{x}(k) - \mathbf{W}\mathbf{e}(k) + \\ -qt_s\boldsymbol{\sigma}(k) - \varepsilon t_s \text{sign}(\boldsymbol{\sigma}(k)) \end{bmatrix} \right) \end{aligned} \quad (3.47)$$

(3.47) can be rewritten as:

$$\mathbf{y}(k+1) = \boldsymbol{\xi}_d(k) + \mathbf{y}^*(k+1) + \boldsymbol{\sigma}(k) - qt_s \boldsymbol{\sigma}(k) - \varepsilon t_s \text{sign}(\boldsymbol{\sigma}(k)) \quad (3.48)$$

In order to obtain the posterior value of \mathbf{y}^* , $(k+1)$, the variable \mathbf{y}^* is replaced by its filtered value \mathbf{y}_f^* :

$$\frac{\mathbf{y}_f^*(k+1)}{\mathbf{y}^*(k+1)} = F(z) = \frac{1-p}{z-p} \quad (3.49)$$

with $p \ll 1$.

So, (3.48) can be rewritten as:

$$\mathbf{y}(k+1) = \boldsymbol{\xi}_d(k) + \mathbf{y}_f^*(k+1) + \boldsymbol{\sigma}(k)(1-qt_s) - \varepsilon t_s \text{sign}(\boldsymbol{\sigma}(k)) \quad (3.50)$$

From (3.50) it is possible to conclude that the response of the system depends on the quasi-sliding mode band, on the filtered reference and on the disturbances.

From (3.50), the sliding mode dynamic can be written as:

$$\boldsymbol{\sigma}(k+1) = \boldsymbol{\xi}_d(k) + \boldsymbol{\sigma}(k)(1-qt_s) - \varepsilon t_s \text{sign}(\boldsymbol{\sigma}(k)) \quad (3.51)$$

According to the quasi-sliding mode definition, the sign of $\boldsymbol{\sigma}(k+1)$ must be opposite to the signal of $\boldsymbol{\sigma}(k)$ and the region where every state satisfies this condition constitutes the quasi-sliding mode band. This region is defined by:

$$|\boldsymbol{\sigma}(k)| < \frac{\varepsilon t_s}{1-qt_s} \quad (3.52)$$

The relationship shown in (3.52) represents the magnitude of the oscillations of $\boldsymbol{\sigma}(k)$ around zero. Thus, the width of the quasi-sliding mode band is given by:

$$2\Delta = 2 \frac{\varepsilon t_s}{1-qt_s} \quad (3.53)$$

and, in steady space, when $\sigma(k) = 0$, the region that constitutes the quasi-sliding mode band is given by:

$$|\sigma(k)| < \varepsilon t_s \quad (3.54)$$

From the definition of the quasi-sliding mode band in steady-states, as shown in (3.54), it can be concluded that the width of the boundary layer may be reduced by using a smaller ε and/or reducing the sampling period. In other words, the robustness is improved by decreasing the sampling period and hence the smaller is the sampling time, the smaller is the effect of the sampling in the system.

Bartoszewicz considers in [70] that the quasi-sliding mode band in the steady space developed by Gao, shown in (3.54), is too conservative and proposes a new quasi-sliding mode band definition when the system is in the steady state. This is given by:

$$\sigma(k) \leq \frac{\varepsilon t_s}{2 - qt_s} \quad (3.55)$$

or

$$\sigma(k) = \frac{\varepsilon t_s}{2 - qt_s}$$

The new definition of the quasi-sliding mode band in (3.55) shows that the bandwidth in steady state depends not only on ε and t_s but also on the parameter q .

The dynamic performance of the Gao controller will be analyzed by the simulation results and posterior by experimental investigations.

3.4.2. Stability proof of the discrete time sliding mode controller on the basis of a Lyapunov function

The Lyapunov stability theory is used to analyze the stability of the current controller by establishing a necessary and sufficient condition to ensure a stable convergence. First, the stability analysis is carried out without considering the disturbance in the model.

Considering the positive definite function:

$$V(k) = \boldsymbol{\sigma}^T(k) \mathbf{P} \boldsymbol{\sigma}(k) \quad (3.56)$$

and

$$V(k+1) = \boldsymbol{\sigma}^T(k+1) \mathbf{P} \boldsymbol{\sigma}(k+1) \quad (3.57)$$

From (3.56) and (3.57):

$$\Delta V(k) = V(k+1) - V(k) \quad (3.58)$$

$$\Delta V(k) = (\boldsymbol{\sigma}^T(k+1) \mathbf{P} \boldsymbol{\sigma}(k+1)) - (\boldsymbol{\sigma}^T(k) \mathbf{P} \boldsymbol{\sigma}(k)) \quad (3.59)$$

Considering that there are not disturbances in the system and replacing (3.51) into (3.59), it becomes:

$$\Delta V(k) = \begin{bmatrix} \boldsymbol{\sigma}(k) - qt_s \boldsymbol{\sigma}(k) - \\ -\varepsilon t_s \text{sign}(\boldsymbol{\sigma}(k)) \end{bmatrix}^T \mathbf{P} \begin{bmatrix} \boldsymbol{\sigma}(k) - qt_s \boldsymbol{\sigma}(k) - \\ -\varepsilon t_s \text{sign}(\boldsymbol{\sigma}(k)) \end{bmatrix} - (\boldsymbol{\sigma}^T(k) \mathbf{P} \boldsymbol{\sigma}(k)) \quad (3.60)$$

(3.60) can be rewritten as:

$$\Delta V(k) = S_3(k) (qt_s (-2 + qt_s)) + S_1(k) (2\varepsilon t_s (-1 + qt_s)) + \varepsilon^2 t_s^2 \quad (3.61)$$

where:

$$S_1(k) = \begin{pmatrix} \sigma_a(k) \text{sign}(\sigma_a(k)) + \sigma_b(k) \text{sign}(\sigma_b(k)) + \\ + \sigma_c(k) \text{sign}(\sigma_c(k)) + \sigma_d(k) \text{sign}(\sigma_d(k)) + \\ + \sigma_e(k) \text{sign}(\sigma_e(k)) + \sigma_f(k) \text{sign}(\sigma_f(k)) \end{pmatrix} = \quad (3.62)$$

$$= |\sigma_a(k)| + |\sigma_b(k)| + |\sigma_c(k)| + |\sigma_d(k)| + |\sigma_e(k)| + |\sigma_f(k)|$$

$$S_3(k) = (\sigma_a^2(k) + \sigma_b^2(k) + \sigma_c^2(k) + \sigma_d^2(k) + \sigma_e^2(k) + \sigma_f^2(k)) \quad (3.63)$$

The mathematical development of (3.60) to get to (3.61) is given in Appendix B.2.

In order to ensure the convergence of the controlled system to the sliding surface, the rate of change ΔV in (3.61) must be negative. Hence, it is necessary to define the limits of the controller parameters in such a manner that ΔV is negative.

Rewriting (3.61) as:

$$\Delta V(k) = \Delta V_1(k) + \Delta V_2(k) + \Delta V_3(k) \quad (3.64)$$

where:

$$\Delta V_1(k) = S_3(k) (qt_s (-2 + qt_s)) \quad (3.65)$$

$$\Delta V_2(k) = S_1(k) (2\epsilon t_s (-1 + qt_s)) \quad (3.66)$$

$$\Delta V_3(k) = \epsilon^2 t_s^2 \quad (3.67)$$

Considering that $S_1(k)$ and $S_3(k)$ are always positive, the negativity of the term ΔV_1 is ensured if the following condition is satisfied:

$$q < \frac{2}{t_s} \quad (3.68)$$

However, the negativity of ΔV_2 is ensured if it satisfies the condition:

$$q < \frac{1}{t_s} \quad (3.69)$$

$$|\Delta V_1(k) + \Delta V_2(k)| > |\Delta V_3(k)| \quad (3.70)$$

Hence, in order to ensure simultaneously the negativity of ΔV_1 and ΔV_2 , the limits for the parameter q should satisfy the condition given in (3.69) which is equivalent to the condition for the reaching law defined by Gao

in [15]. It should be considered that the negativity of ΔV is ensured if the following condition is satisfied:

$$(\boldsymbol{\sigma}(k+1) - \boldsymbol{\sigma}(k)) (\text{sign} \boldsymbol{\sigma}(k))^T < 0 \quad (3.71)$$

After that, the limits for the term ε should be also defined in such a manner that the negativity of ΔV is maintained. It is important to note that a bigger value for ε can lead the system to instability because it becomes more difficult to maintain the negativity of ΔV as the term $\varepsilon^2 t_s^2$ is high.

Considering the lower limit inequality given in (3.39) and replacing (3.51) on it, the lower limit of ε is defined by:

$$[-\boldsymbol{\sigma}(k)qt_s - \varepsilon t_s \text{sign}(\boldsymbol{\sigma}(k))] \text{sign}(\boldsymbol{\sigma}(k))^T < 0 \quad (3.72)$$

that becomes:

$$\varepsilon > -qS_1(k) \quad (3.73)$$

The mathematical development of (3.72) to get to (3.73) is given in Appendix B.3.

From (3.73), the negativity of ε is always ensured for all values of q and $S_1(k)$.

Considering the upper limit inequality given in (3.40) and replacing (3.51) on it, it becomes:

$$[\boldsymbol{\sigma}(k) - \boldsymbol{\sigma}(k)qt_s - \varepsilon t_s \text{sign}(\boldsymbol{\sigma}(k)) + \boldsymbol{\sigma}(k)] (\text{sign}(\boldsymbol{\sigma}(k)))^T \geq 0 \quad (3.74)$$

Solving the inequality:

$$\begin{aligned} 2\boldsymbol{\sigma}(k)(\text{sign}(\boldsymbol{\sigma}(k)))^T - \boldsymbol{\sigma}(k)qt_s(\text{sign}(\boldsymbol{\sigma}(k)))^T - \\ -\varepsilon t_s \text{sign}(\boldsymbol{\sigma}(k)) (\text{sign}(\boldsymbol{\sigma}(k)))^T \geq 0 \end{aligned} \quad (3.75)$$

and rewritten it as:

$$2S_1(k) - qt_s S_1(k) \geq \varepsilon t_s \quad (3.76)$$

The upper limit of ε is given by:

$$\varepsilon \leq \frac{S_1(k)(2 - qt_s)}{t_s} \quad (3.77)$$

The mathematical development of (3.75) to get to (3.76) is given in Appendix B.4.

It can be concluded that the superior limit of ε is inversely proportional to the sampling time. The lower the sampling time, the greater the upper limit — ensuring the stability of the control law. The limit conditions for the control parameters are established without having to consider disturbances in the model. The next subsection will present the stability analysis by considering a system where disturbances are added to the model.

3.4.3. Stability proof of the discrete time sliding mode controller on the basis of a Lyapunov function considering disturbance in the system.

The stability of the system by considering disturbances in the nominal model will be analyzed in this section following the Lyapunov stability theory.

Replacing (3.51) into (3.59):

$$\begin{aligned} \Delta V(k) = & \left[\begin{array}{c} \xi_d(k) + \sigma(k)(1 - qt_s) - \\ -\varepsilon t_s \text{sign}(\sigma(k)) \end{array} \right]^T \mathbf{P} \left[\begin{array}{c} \xi_d(k) + \sigma(k)(1 - qt_s) - \\ -\varepsilon t_s \text{sign}(\sigma(k)) \end{array} \right] - \\ & - (\sigma^T(k) \mathbf{P} \sigma(k)) \end{aligned} \quad (3.78)$$

(3.78) can be rewritten as:

$$\begin{aligned} \Delta V(k) = & 2\varepsilon t_s S_1(k)(qt_s - 1) + 2S_2(k)(1 - qt_s) + \\ & + qt_s S_3(k)(-2 + qt_s) + S_4(k) - 2\varepsilon t_s S_5(k) + \varepsilon^2 t_s^2 \end{aligned} \quad (3.79)$$

where $S_1(k)$ and $S_3(k)$ are defined in (3.62) and (3.63), respectively, and:

$$S_2(k) = \xi_{da}(k)\sigma_a(k) + \xi_{db}(k)\sigma_b(k) + \xi_{dc}(k)\sigma_c(k) + \xi_{dd}(k)\sigma_d(k) + \xi_{de}(k)\sigma_e(k) + \xi_{df}(k)\sigma_f(k) \quad (3.80)$$

$$S_4(k) = \xi_{da}^2(k) + \xi_{db}^2(k) + \xi_{dc}^2(k) + \xi_{dd}^2(k) + \xi_{de}^2(k) + \xi_{df}^2(k) \quad (3.81)$$

$$S_5(k) = \xi_{da}(k)\text{sign}(\sigma_a(k)) + \xi_{db}(k)\text{sign}(\sigma_b(k)) + \xi_{dc}(k)\text{sign}(\sigma_c(k)) + \xi_{dd}(k)\text{sign}(\sigma_d(k)) + \xi_{de}(k)\text{sign}(\sigma_e(k)) + \xi_{df}(k)\text{sign}(\sigma_f(k)) \quad (3.82)$$

The mathematical development of (3.78) to get to (3.79) is given in Appendix B.5.

Rewriting (3.79) as:

$$\Delta V(k) = \Delta V_1(k) + \Delta V_2(k) + \Delta V_3(k) + \Delta V_4(k) \quad (3.83)$$

where $\Delta V_1(k)$, $\Delta V_2(k)$, $\Delta V_3(k)$ are defined in (3.65), (3.66), and (3.67), and $\Delta V_4(k)$ is given by:

$$\Delta V_4(k) = 2S_2(k)(1 - qt_s) + S_4(k) - 2\epsilon t_s S_5(k) \quad (3.84)$$

The negativity of $\Delta V_1(k)$ and $\Delta V_2(k)$ is ensured following the condition defined in (3.69).

Considering that $\Delta V_3(k)$ is always positive and $\Delta V_4(k)$ has a complex definition due to its disturbance dependence, it could be assumed that the negativity of $\Delta V(k)$ is ensured if:

$$|\Delta V_1(k) + \Delta V_2(k)| > |\Delta V_3(k) + \Delta V_4(k)| \quad (3.85)$$

The parameter ϵ should be large enough to overcome the disturbances in the term $\Delta V_4(k)$ and to ensure Condition (3.85). However, the use of a large value for ϵ can add chattering to the system, which is undesirable. For this reason, the development of a disturbance observer is a good alternative in order to estimate and compensate the disturbance of the

system. Hence, the value of ε must not be very large to guarantee the negativity of $\Delta V(k)$. The association of a disturbance observer with the discrete time sliding mode based on Gao's approach will be presented in Chapter 4.

3.5. Discrete time super-twisting controller

Considering that the boundary layer approach used in order to reduce the chattering in the first-order sliding mode degrades the robustness of the control, the high-order sliding mode control emerges like an alternative to eliminate the chattering, maintaining the accuracy and robustness of the control. The high-order sliding mode (HOSM) concept was introduced by Levant [57].

In the standard sliding mode control, also called first-order sliding mode control, the discontinuous control action appears in the first total derivative of the sliding surface ($\dot{\sigma}$). For the high-order sliding mode with order r^{st} , the discontinuous control appears in the $(r - 1)$ time derivative of the sliding surface and hence the control input is continuous. Consequently, the chattering is removed and the robustness of the control is maintained. Therefore, the order of the HOSM is given by the number of total time derivatives that are needed until the appearance of the discontinuous control [71].

The main idea of HOSM is to reduce to zero not only the sliding surface but also its high order derivatives. So, the r -order sliding mode must satisfy the condition:

$$\sigma = \dot{\sigma} = \ddot{\sigma} = \dots = \sigma^{(r-1)} = 0 \quad (3.86)$$

The major disadvantage of the HOSM approach is the increased information demand — for example, a second-order sliding mode needs the information about the first-time derivative of the sliding surface which is often unavailable. One exception is the super-twisting algorithm that is a second-order sliding mode controller and does not require any information about the sliding surface time derivative ($\dot{\sigma}$). The super-twisting algo-

rithm is applied to the system with relative degree 1 in order to avoid the chattering effect without losing the accuracy. It requires low information demand and present implementation simplicity, and for this reason, it is widely used in practical applications. This algorithm is characterized by describing a spiral trajectory in the phase plane $(\sigma - \dot{\sigma})$, as shown in Figure 3.9.

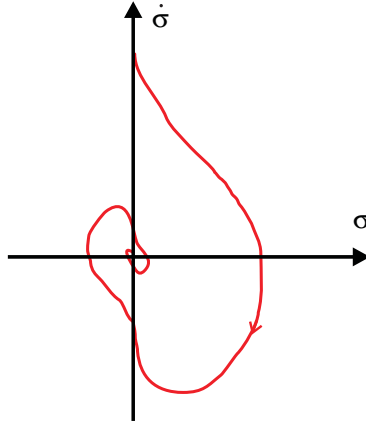


Figure 3.9.: Super-twisting trajectory in the phase plane.

The continuous time super-twisting algorithm is defined by:

$$\begin{aligned} \mathbf{u}_{st} &= -\lambda_1 |\sigma|^{1/2} \text{sign}(\sigma) + \mathbf{u}_1 \\ \dot{\mathbf{u}}_1 &= -\lambda_2 \text{sign}(\sigma) \end{aligned} \quad (3.87)$$

From (3.87) it is possible to notice that the super-twisting algorithm does not require the time derivative of the sliding variable [11].

The super-twisting algorithm was originally developed in continuous time. However, the practical implementation in digital microprocessors must be considered. The discrete time super-twisting approach is not well established in the literature, with few articles addressing this issue.

As an important scientific contribution, this section presents the formulation and stability analysis of a discrete time super-twisting algorithm applied to a six-phase BLDC machine.

In this work, a discrete time formulation of the super-twisting algorithm is based on Euler discretization. The same approach is used in [72, 73] for different applications.

The discretization issues of HOSM are examined in [74] by Levant, where it is ensured that the accuracy of the output-feedback HOSM technique is preserved if its digital implementation in controlling continuous time systems is based on the simple zero order hold control and internal one-step Euler integration.

3.5.1. Discrete time super-twisting controller applied to the six-phase BLDC machine

Considering the sliding surface defined in accordance with (3.41), the first time derivative of the sliding surface is given by:

$$\sigma(k+1) - \sigma(k) = (\mathbf{x}(k+1) - \mathbf{x}^*(k+1)) - (\mathbf{x}(k) - \mathbf{x}^*(k)) \quad (3.88)$$

Replacing the discrete dynamic model of the brushless DC machine given in (2.28) into (3.88):

$$\sigma(k+1) = (\mathbf{H}\mathbf{u}(k) + \mathbf{G}\mathbf{x}(k) + \mathbf{W}\mathbf{e}(k) + \boldsymbol{\xi}_d(k) - \mathbf{x}^*(k+1)) \quad (3.89)$$

The equivalent control concept will be applied here to define the control law:

$$\mathbf{u}(k) = \mathbf{u}_{\text{eq}}(k) + \mathbf{u}_n(k) \quad (3.90)$$

where \mathbf{u}_{eq} is the equivalent control component and represents the continuous component of the control, and \mathbf{u}_n is the super-twisting algorithm term.

To define the equivalent control term, it should be considered that $\sigma(k+1) = 0$ and the disturbances of the system are null ($\xi_d(k) = 0$). Hence, applying these conditions to (3.89) is given in the following:

$$\mathbf{u}_{\text{eq}}(k) = \mathbf{H}^{-1} (\mathbf{x}^*(k+1) - \mathbf{G}\mathbf{x}(k) - \mathbf{W}\mathbf{e}(k)) \quad (3.91)$$

Defining \mathbf{u}_{n} as:

$$\mathbf{u}_{\text{n}}(k) = \mathbf{H}^{-1} (-\mathbf{u}_{\text{st}}(k)) \quad (3.92)$$

So, replacing (3.91) and (3.92) into (3.90), the control law can be defined as:

$$\mathbf{u}(k) = \mathbf{H}^{-1} (\mathbf{x}^*(k+1) - \mathbf{G}\mathbf{x}(k) - \mathbf{W}\mathbf{e}(k) - \mathbf{u}_{\text{st}}(k)) \quad (3.93)$$

where \mathbf{u}_{st} represents the discrete super-twisting term that is defined by the Euler discretization of the continuous super-twisting algorithm — given in (3.87) — as:

$$\begin{aligned} \mathbf{u}_{\text{st}}(k) &= -\lambda_1 |\sigma(k)|^{1/2} \text{sign}(\sigma(k)) + \mathbf{u}_1(k) \\ \mathbf{u}_1(k+1) &= \mathbf{u}_1(k) - t_s \lambda_2 \text{sign}(\sigma(k)) \end{aligned} \quad (3.94)$$

Now, replacing equation (3.93) into (3.89) gives the dynamic response of the system:

$$\sigma(k+1) = \left(\begin{array}{l} \mathbf{H} [\mathbf{H}^{-1} (\mathbf{x}^*(k+1) - \mathbf{G}\mathbf{x}(k) - \mathbf{W}\mathbf{e}(k) - \mathbf{u}_{\text{st}}(k))] + \\ + \mathbf{G}\mathbf{x}(k) + \mathbf{W}\mathbf{e}(k) + \xi_d(k) - \mathbf{x}^*(k+1) \end{array} \right) \quad (3.95)$$

$$\sigma(k+1) = (-\mathbf{u}_{\text{st}}(k) + \xi_d(k)) \quad (3.96)$$

(3.96) represents the dynamics of the sliding surface. The dynamics of the sliding surface converges to zero in finite time, depending on the disturbance and on the super-twisting action.

3.5.2. Stability proof of the discrete time super-twisting controller on the basis of a Lyapunov function considering disturbance in the system.

The study of the discrete time super-twisting is still not well established in the literature. Only a few authors have presented the theoretical background of this technique and its stability proofs. The stability analysis of the discrete time super-twisting algorithm has been developed in this work based on the approach presented by [73], where the stability of the discrete super-twisting algorithm is analyzed with a quadratic Lyapunov function while the stability conditions are achieved by a linear matrix inequality. Considering the system given in (2.28) and the back-emf as a disturbance added to the system, the dynamic model can be rewritten as:

$$\mathbf{x}(k+1) = \mathbf{G}\mathbf{x}(k) + \mathbf{H}\mathbf{u}(k) + \boldsymbol{\eta}_d(k) \quad (3.97)$$

with $\boldsymbol{\eta}_d = \mathbf{W}\mathbf{e}(k) + \boldsymbol{\xi}_d(k)$ and $\boldsymbol{\eta}_d \in \mathfrak{R}^n$.

Replacing the control law given in (3.94) into the plant given in (3.97):

$$\mathbf{x}(k+1) = \mathbf{G}\mathbf{x}(k) + \mathbf{H}\lambda_1|\boldsymbol{\sigma}(k)|^{1/2}\text{sign}(\boldsymbol{\sigma}(k)) + \mathbf{H}\mathbf{u}_1(k) + \boldsymbol{\eta}_d(k) \quad (3.98)$$

Considering that there is an upper bound for the disturbances:

$$\|\boldsymbol{\eta}_d(k)\| \leq \boldsymbol{\Pi}^+ \quad (3.99)$$

The proof is developed by combining an n-order dynamic system given in (3.98) with the control law equations given in (3.94) in a unique $2n$ -dimensional system. This is given by:

$$\boldsymbol{\psi}(k+1) = \mathbf{J}\boldsymbol{\psi}(k) + \mathbf{L}(k)\text{sign}(\boldsymbol{\sigma}(k)) \quad (3.100)$$

with: $\boldsymbol{\psi}(k+1) \in \mathfrak{R}^{2n}$, $\mathbf{J} \in \mathfrak{R}^{2n \times 2n}$, $\mathbf{L}(k) \in \mathfrak{R}^{2n \times n}$. In this application $n = 6$.

According to [73], considering the nonlinear system given in (3.100), with gains $\lambda_1 > 0$ and $\lambda_2 > 0$ and if the LMI given by $[A^T(\mathbf{P} + \mathbf{P}\mathbf{A})A -$

$(1 - \varsigma)\mathbf{P} + \mathbf{Q} \leq 0$ has a positive solution, then the dynamic system converges asymptotically to a ball centred at the origin with a radius given by:

$$R = \frac{\Theta}{1 - \varsigma} \quad (3.101)$$

The proof of the discrete time super-twisting control stability is presented in detail in Appendix B.6.

3.6. Simulation results

In this section, the performances of the proposed current controllers developed in this chapter and applied to the six-phase brushless DC machine are qualitatively analyzed by the simulation results.

The simulations are carried out with the software MATLAB[®], where the algorithms are implemented with a sampling frequency of 50 kHz, with exception of the continuous time sliding mode simulations that are carried out with the software Simulink that has the appropriate functions to perform a continuous simulation.

The parameters of the machine used in the simulations are shown in Table 3.1.

Number of phases	6
Pole pairs - P	4
Number of stator slots	48
Number of turns	5
Phase resistance - R_s	38 $m\Omega$
Phase inductance - L_s	10.5 μH
Back-emf constante - K_e	0.0198 Vs/rad
Rated torque - T_e	2.5 Nm
Rated power	0.6 kW
DC link voltage - V_{DC}	12 V
Rated speed	2250 rpm
Rated phase current	25 A

Table 3.1.: Motor specification.

It is assumed that the self- and mutual inductances of the model vary in accordance with the measurements presented in Chapter 2, in Figure 2.9.

It is considered that the back-emf is known and its effect is completely cancelled through the feedforward control for all presented controllers; therefore, the disturbances applied to the model in these simulations are only the self- and mutual inductances variations.

The main aim of the simulations is to demonstrate that the proposed controllers based on the sliding mode approach can provide robustness with respect to parameter variations.

In the simulations, it is possible to analyze the controller dynamic response by the simulated phase current versus the reference phase current. It is important to verify if the controller is able to overcome the uncertainties and parameter variations to ensure the convergence of the phase current to the desired trajectories.

The final aim of the phase current control is to ensure a resultant electrical torque in the machine with minimal oscillations, despite the non-idealities of the model.

This section will also present the simulations results for the speed control carried out with the software Simulink.

3.6.1. Discrete time proportional-integral controller

For the simulation, it is considered the discrete dynamic model of the machine described as in (2.28).

The amplitude of the current reference is determined by the output of the speed controller. The current reference is null in the points where the back-emf is not constant; it is positive if the hall sensor signal is 0 and negative if the signal is 1.

Figure 3.10 shows the simulation results of the discrete proportional-integral current controller for an operation point with 2250 rpm speed and 1 Nm Load Torque. Figure 3.10 (a) shows the convergence of the current to the current reference, while Figure 3.10 (b) shows the tracking error for the phase current control. Figure 3.10 (c) shows the output of the current controller, Figure 3.10 (d) the resultant electrical torque and Figure 3.10 (e) the zoom of the electrical torque.

Through the simulation results an oscillatory response in the current and consequently in the electrical torque is noted, although it is assumed that the back-emf is known, due to the magnetic coupling between the phases and the poor robustness of the conventional PI controller.

As the speed increases, the current controller should react rapidly so that the controller gain should be adjusted, but owing to the limited bandwidth, a greater parameter variation can lead the control to instability.

Therefore, we can conclude that the PI controller presents a slow response time which reduces the operation range of the BLDC drive [48] and is not robust to lead with the parameter variations and the non-idealities from the machine model.

3.6.2. Continuous time sliding mode controller

The simulations for the continuous time sliding mode controller are carried out with the software Simulink for an operation point with 2250 rpm speed and 1 Nm Load Torque. The dynamic model of the machine is simulated in accordance the model represented in (2.26). To verify the robustness issues of the sliding mode control, it is assumed that the self- and mutual inductances in the model are dependent on rotor angles and they behave as presented in Chapter 2, in Figure 2.9. Figure 3.11 (a) presents the phase current A versus the current reference; Figure 3.11 (b) presents the tracking error for the current in phase A; Figure 3.11 (c) shows the output of the sliding mode controller for phase A; Figure 3.11 (d) shows the total electrical torque that is generated in the machine and Figure 3.11 (e) presents the zoom of the electrical torque.

In the simulations, the chattering phenomenon is reduced with the use of the boundary layer. Even considering the model with self- and mutual inductances varying with the rotor angle, the controller ensures a good dynamic response against parameter variations and a good current reference tracking, thereby proving the robustness of a system where the model is not exactly known.

The problem with this kind of control is that its implementation should be realized in continuous time domain to be valid. Many works use the

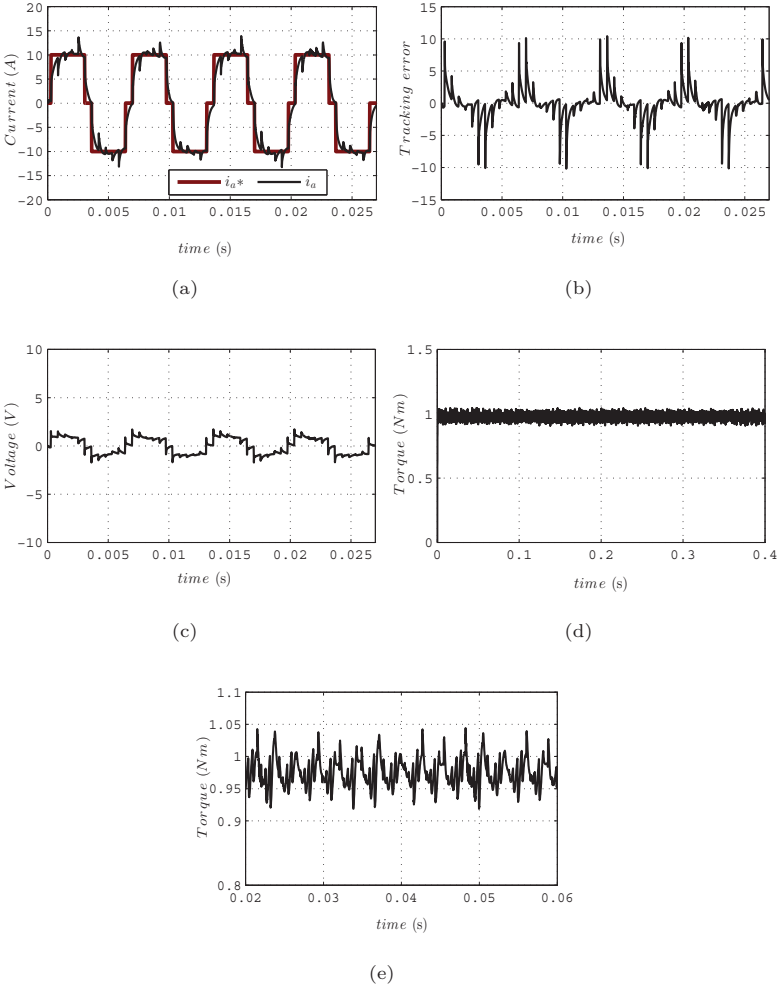


Figure 3.10.: Discrete time proportional-integral control. (a) Current reference (i_a^*) versus measured current (i_a) for phase A; (b) tracking error for phase A; (c) output of phase A current controller; (d) electrical torque; (e) zoom of electrical torque.

continuous time formulation of the sliding mode in a digital implementation, but the stability proofs applied to a continuous time sliding mode controller cannot be extended to a discrete implementation. The test bench for the experimental results for this work uses a digital implementation in a FPGA system and hence experimental tests of the continuous time sliding mode control were not implemented. The continuous time sliding mode control was presented in this chapter to provide the basic understanding of the sliding mode technique concepts and facilitate the development of the discrete time sliding mode approach.

3.6.3. Discrete time sliding mode controller: Gao's approach

The simulations are carried out to validate the discrete time sliding mode control law developed in this chapter and to demonstrate that it is possible to overcome model uncertainties and external disturbances by using a discrete algorithm.

In the six-phase machine simulated model, it is considered that the self- and mutual inductances have the behavior described in Chapter 2, in Figure 2.9, and also that the back-emf from each phase is ideal and known.

The figure below shows the response of the discrete time sliding mode at the rated speed (2250 rpm) and 1 Nm Load Torque. Figure 3.12 (a) presents the phase current A versus the current reference; Figure 3.12 (b) presents the tracking error for the current in phase A; Figure 3.12 (c) shows the output of the discrete time sliding mode controller for phase A; Figure 3.12 (d) shows the total electrical torque that is generated in the machine and Figure 3.12 (e) presents the zoom of the electrical torque.

By the simulations results it is possible to verify that the dynamic response of the current is improved with the discrete time sliding mode controller, in comparison with a classical proportional-integral controller. Moreover, with the discrete time sliding mode control, it is not necessary to adjust the controller gain for different operation points. The controller tries to compensate the effect of the mutual inductances, which can be verified in the output of the controller in Figure 3.12 (c). However, its

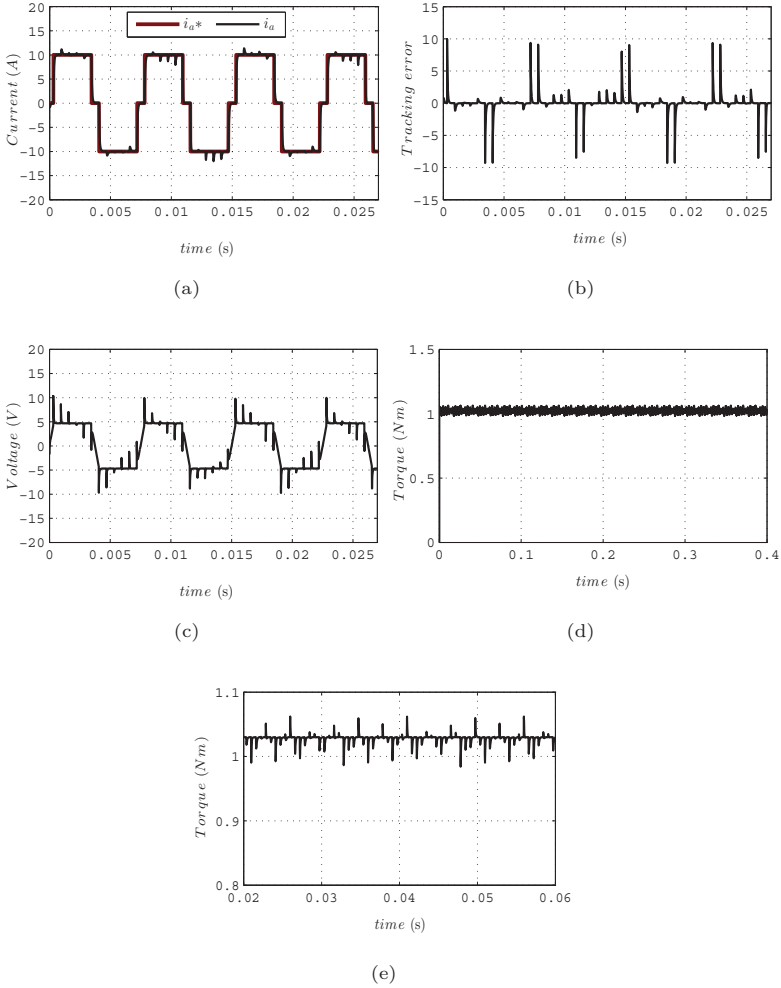


Figure 3.11.: Continuous time sliding mode control. (a) Current reference (i_a^*) versus measured current (i_a) for phase A; (b) tracking error for phase A; (c) output of phase A current controller; (d) electrical torque; (e) zoom of electrical torque.

effort is not sufficient to compensate all the non-idealities in the model, and there are oscillations in the phase current and in the electrical torque related to the magnetic coupling. The oscillation torque is defined as the average of the difference between the maximum and the minimum values of torque which, in this case, is about 9%.

In the simulations presented in this chapter, it is assumed that the back-emf is totally known, but actually the back-emf cannot be directly measured and it can only be observed. It is possible to know partially the amplitude of the back-emf by (2.12), but this does not reproduce the non-idealities from the back-emf of each phase, as shown in Figure 2.11. It is concluded that the discrete time sliding mode controller cannot overcome all the disturbances present in the model and therefore a disturbance observer in combination with the discrete time sliding mode controller is proposed in the next chapter to ensure a good dynamic response for the system under parameter variations.

3.6.4. Discrete time sliding mode controller: super-twisting approach

The simulation results for the discrete time super-twisting sliding mode control, considering that the self- and mutual inductances vary in accordance with the rotor position and that the back-emf from each phase is ideal and known, are shown in this section.

Figure 3.13 presents the response of the discrete super-twisting sliding mode control at the rated speed and 1 Nm Load Torque. Figure 3.13 (a) presents the phase current A versus the current reference; Figure 3.13 (b) presents the tracking error for the current in phase A; Figure 3.13 (c) shows the output of the discrete time sliding mode controller for phase A; Figure 3.13 (d) shows the total electrical torque and Figure 3.13 (e) presents the zoom of the electrical torque.

The super-twisting controller presents a dynamic response even faster than the discrete time sliding mode controller, which is the characteristic of the second-order sliding mode controller as well as of the chattering reduction. Similarly to the simulation results presented for the discrete

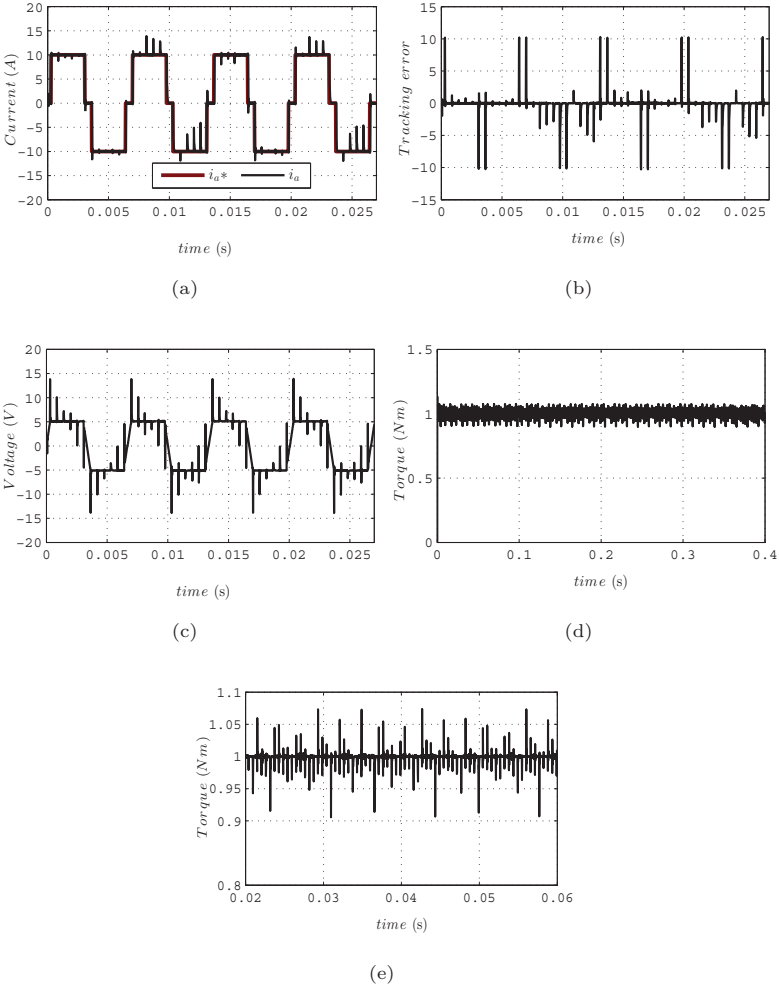


Figure 3.12.: Discrete time sliding mode control. (a) Current reference (i_a^*) versus measured current (i_a) for phase A; (b) tracking error for phase A; (c) output of phase A current controller; (d) electrical torque; (e) zoom of electrical torque.

time sliding mode controller, the super-twisting controller cannot overcome all the effects of the coupling between the phases and a torque oscillation about 9% is present. It is important to remark that the effect of the mutual inductances in the phase current takes place with very fast dynamic and that even a controller with a high dynamic response, such as the super-twisting controller, is not enough to remove the effect of the non-idealities at 50 kHz sampling frequency.

3.6.5. Speed control

The control structure of the BLDC machine has an internal loop for current control and an external loop for speed control (Figure 3.1). The speed control is carried out with a classical proportional-integral controller. Since the mechanical dynamic is slower than the electrical dynamic and has to deal just with the load torque variation, the classical PI controller seems to be adequate.

The simulation was carried out with the software Simulink, considering a continuous plant and a discrete control implementation with a sampling frequency of 50 kHz. Figure 3.14 shows the speed tracking for a speed reference that varies from 0 to 104.72 rad/s (1000 rpm) from 0s–1s and keeps at 104.72 rad/s from 1s–5s, increases again from 104.72 rad/s to 209.44 rad/s (2000 rpm) from 5s–6s and remains at 209.44 rad/s from 6s–10s. A torque load of 2.25 Nm is applied to the system from 7s–10s.

Figure 3.14 (a) presents measured speed versus the speed reference; Figure 3.14 (b) presents the speed tracking error; Figure 3.14 (c) shows the output of proportional-integral speed controller and Figure 3.14 (d) shows the load torque applied to the system.

The speed tracks the trajectory reference with a good dynamic response even when a load torque is applied to the system. The output of the speed controller in Figure 3.14 (c) defines the amplitude of the current reference.

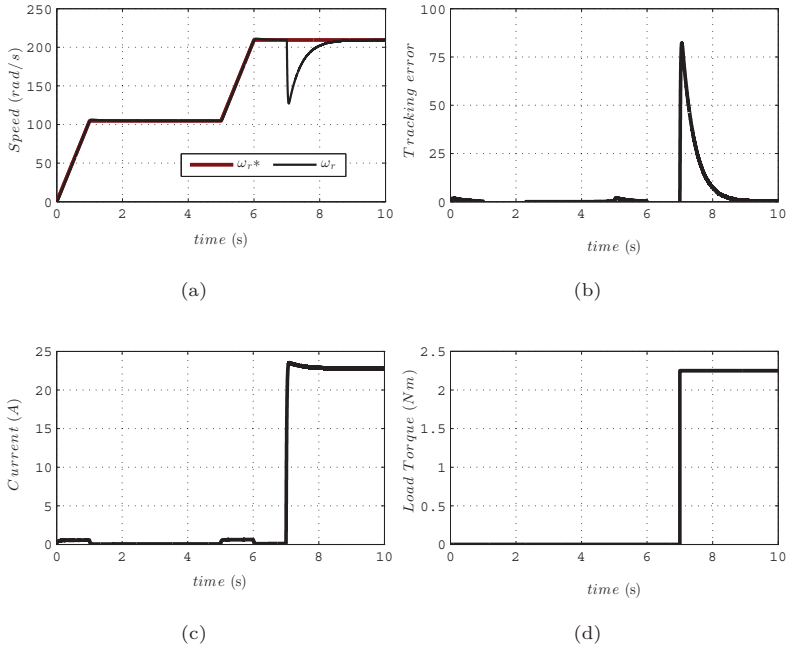


Figure 3.14.: (a) Speed reference versus measured speed; (b) speed tracking error; (c) speed controller output; (d) load torque.

3.6.6. Summary

In this chapter, different current control strategies are presented in order to ensure a good performance of the six-phase brushless DC machine. Firstly, a standard proportional-integral controller was introduced for being one of the most common used controllers in the industry. A sliding mode controller was developed in the continuous time domain in order to provide the basic concepts of the sliding mode technique. After that, two discrete time sliding mode controllers have been presented: a first-order sliding mode and a second-order sliding mode based on a super-twisting algorithm. The controllers and the stability proofs are developed in the discrete time

domain aiming the practical experimentation. The simulations are carried out to show the performance of the controllers presented in this chapter.

With the simulation results, it is concluded that the proposed discrete controllers are not capable of overcoming all the effects of the mutual inductances in the phase currents. To solve this issue, the next chapter presents a disturbance observer in combination with the proposed discrete time sliding mode controllers. The next chapter also proposes a new current reference to minimize the effect of the coupling between the phases.

4. Discrete time disturbance observer applied to the brushless DC machine

4.1. Introduction

The continuous time sliding mode control stands out for its invariance property, control simplicity and robustness against parameter uncertainties and external disturbances. However, there is a practical limitation of the continuous time sliding mode control owing to the fact that most of the practical implementations are carried out by using digital signal processors, which deteriorates the discontinuous control response and may lead the system to the instability. For this reason, a discrete time sliding mode approach has been developed in this work. In the discrete time sliding mode control the system is kept in a quasi-sliding mode band around the sliding surface and the control law is changed only at discrete instants. Hence, the invariance property is not achieved by discrete time sliding mode controllers but remains a satisfying robustness property. Nevertheless, the chattering appears in the presence of large varying disturbances.

According to the simulation results presented in the last chapter, it can be concluded that the proposed discrete time sliding mode controllers are not robust enough to overcome the unknown disturbances added to the system, such as the back-emf non-idealities and the parameter variations related to the mutual coupling between the phases of the six-phase brushless DC machine.

To improve the tracking accuracy in the presence of internal and external disturbances and to remove the chattering, a control scheme, that combines a discrete time sliding mode controller and a disturbance estimator, is proposed. Many applications presented in the literature, such as [16–23], have shown that the use of the sliding mode controller that in-

cludes a disturbance observer improves the robustness and the disturbance attenuation.

Since the uncertainties and the external disturbances are estimated by the disturbance observer, the discrete time sliding mode controllers are designed considering the nominal plant and as a consequence, the zigzag motion in the quasi-sliding mode band around the surface substantially reduces, which relieves the chattering problem.

The purpose of the disturbance observer is to compensate the effect of the disturbance by a feedback control by forcing the real plant to behave as the nominal plant.

The control law (\mathbf{u}) will be composed by two terms, one relative to the discrete time controller (\mathbf{u}_{smc}) and another to the observed disturbance ($\hat{\xi}_d$). This chapter proposes two different disturbance observer approaches, combined with the discrete time sliding mode control based on Gao's approach, and one disturbance observer approach combined with the discrete super-twisting controller in order to reject the disturbance of the system and track a given current reference.

Figure 4.1 shows a block diagram of the control scheme with the controller combined with a disturbance observer.

The design of the disturbance observer is carried out, considering that only the output of the system, in case the phase currents, are measured and no additional sensors are needed. In the next sections, two different disturbance observers, which are combined with discrete time sliding mode controllers and applied to the six-phase brushless DC machine model, will be presented.

4.2. Discrete time sliding mode control with decoupled variable structure disturbance observer

This work proposes a discrete time disturbance observer, combined with the discrete time sliding mode controller based on Gao's approach presented in the previous chapter. The design of the disturbance observer is also based on the variable structure concept and follows the formulation presented in [75]. The aim is to develop a disturbance observer with the disturbance

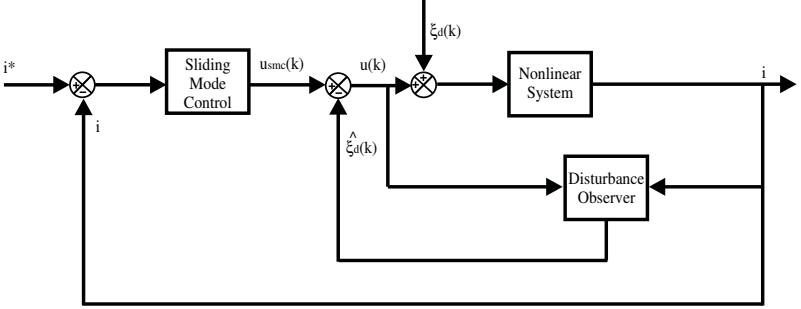


Figure 4.1.: System structure with nonlinear disturbance observer.

estimation dynamic decoupled from the controller tracking error dynamic so that it becomes possible to independently regulate both dynamics. This disturbance observer can be described by the following system:

$$\hat{\xi}_d(k) = \hat{\xi}_d(k-1) + \Lambda (\sigma(k) - qt_s \sigma(k-1) + \epsilon t_s \text{sign}(\sigma(k-1))) \quad (4.1)$$

The study [75] proposes a modification in the Gao's sliding surface dynamic that is given by:

$$\sigma(k+1) = \tilde{\xi}_d(k) + qt_s \sigma(k) - \epsilon t_s \text{sign}(\sigma(k)) \quad (4.2)$$

The estimation error is defined as:

$$\tilde{\xi}_d(k) = \xi_d(k) - \hat{\xi}_d(k) \quad (4.3)$$

and it can be rewritten as:

$$\tilde{\xi}_d(k+1) = \xi_d(k+1) - \hat{\xi}_d(k+1) \quad (4.4)$$

Replacing (4.1) into (4.4):

$$\tilde{\xi}_d(k+1) = \xi_d(k+1) - \hat{\xi}_d(k) - \Lambda \sigma(k+1) + \Lambda qt_s \sigma(k) - \Lambda \epsilon t_s \text{sign}(\sigma) \quad (4.5)$$

and (4.2) into (4.5):

$$\begin{aligned} \tilde{\xi}_d(k+1) = & \xi_d(k+1) - \hat{\xi}_d(k) - \Lambda \tilde{\xi}_d(k) - \Lambda q t_s \sigma(k) + \\ & + \Lambda \varepsilon t_s \text{sign}(\sigma(k)) + \Lambda q t_s \sigma(k) - \Lambda \varepsilon t_s \text{sign}(\sigma(k)) \end{aligned} \quad (4.6)$$

it results in:

$$\tilde{\xi}_d(k+1) = \xi_d(k+1) - \hat{\xi}_d(k) - \Lambda \tilde{\xi}_d(k) \quad (4.7)$$

Replacing (4.3) into (4.7):

$$\tilde{\xi}_d(k+1) = \xi_d(k+1) - \xi_d(k) + (1 - \Lambda) \tilde{\xi}_d(k) \quad (4.8)$$

and considering that:

$$\Delta \xi_d(k+1) = \xi_d(k+1) - \xi_d(k) \quad (4.9)$$

(4.8) can be rewritten as:

$$\tilde{\xi}_d(k+1) = \Delta \xi_d(k+1) + (1 - \Lambda) \tilde{\xi}_d(k) \quad (4.10)$$

(4.10) represents the dynamic of the estimated error. With an appropriate choice of the gain Λ , and following the condition $(1 - \Lambda) < 1$, the disturbance estimation error converges to zero in finite time, depending on the disturbance variation, independent of the initial condition — which means that the disturbance observer is asymptotically stable. It is assumed that this variation is very small for high sampling frequencies.

Combining the discrete time sliding mode control with the proposed disturbance observer, the control law is defined as:

$$\mathbf{u}(k) = \mathbf{u}_{\text{smc}}(k) - \mathbf{H}^{-1} \hat{\xi}_d(k) \quad (4.11)$$

where $\mathbf{u}_{\text{smc}}^1$ represents the discrete time controller term based on Gao's approach defined in (3.44).

¹From this point, the discrete time control law based on Gao's approach defined in (3.44) will be represented by \mathbf{u}_{smc} .

Replacing the control law given into (4.11) and the term related to the discrete time sliding mode control based in Gao's approach given in (3.44) in the dynamic model presented in (2.28), it results in:

$$\mathbf{x}(k+1) = \mathbf{G}\mathbf{x}(k) + \mathbf{W}\mathbf{e}(k) + \boldsymbol{\xi}_d(k) + \mathbf{H} [\mathbf{u}_{\text{smc}}(k) - \mathbf{H}^{-1}\hat{\boldsymbol{\xi}}_d(k)] \quad (4.12)$$

$$\mathbf{x}(k+1) = \mathbf{x}^*(k+1) + \boldsymbol{\sigma}(k)(1 - qt_s) - \varepsilon t_s \text{sign}(\boldsymbol{\sigma}(k)) + \tilde{\boldsymbol{\xi}}_d(k) \quad (4.13)$$

According to (3.41), (4.13) can be rewritten as:

$$\boldsymbol{\sigma}(k+1) = \boldsymbol{\sigma}(k)(1 - qt_s) - \varepsilon t_s \text{sign}(\boldsymbol{\sigma}(k)) + \tilde{\boldsymbol{\xi}}_d(k) \quad (4.14)$$

(4.14) represents the dynamic of the controller combined with the disturbance observer. The system slides asymptotically to the equilibrium point when the estimation error tends to zero or is small in a sampling period.

4.3. Discrete time sliding mode control with reduced order disturbance observer

In this section, a combination of the Gao's approach controller with a reduced order discrete disturbance observer is presented. The proposed disturbance observer follows the formulation developed by [76], which is the discrete version of the continuous time disturbance observer presented in [77].

The disturbance estimator can be described by the following equation:

$$\hat{\boldsymbol{\xi}}_d(k) = \Lambda(\mathbf{x}(k) - \mathbf{z}(k)) \quad (4.15)$$

where the variable \mathbf{z} is defined as:

$$\mathbf{z}(k+1) = \mathbf{z}(k) + (\mathbf{G} - \mathbf{I})\mathbf{x}(k) + \mathbf{H}\mathbf{u}(k) + \mathbf{W}\mathbf{e}(k) + \hat{\boldsymbol{\xi}}_d(k) \quad (4.16)$$

Considering that the estimation error is given by:

$$\tilde{\xi}_a(k) = \xi_a(k) - \hat{\xi}_a(k) \quad (4.17)$$

and it can be rewritten as:

$$\tilde{\xi}_a(k+1) = \xi_a(k+1) - \hat{\xi}_a(k+1) \quad (4.18)$$

Replacing (4.15) into (4.17):

$$\tilde{\xi}_a(k+1) = \xi_a(k+1) - \Lambda(\mathbf{x}(k+1) - \mathbf{z}(k+1)) \quad (4.19)$$

Now, considering the discrete BLDC dynamic model given in (2.28) and replacing it into (4.19):

$$\tilde{\xi}_a(k+1) = \xi_a(k+1) - \Lambda(\mathbf{G}\mathbf{x}(k) + \mathbf{H}\mathbf{u}(k) + \mathbf{W}\mathbf{e}(k) + \xi_a(k) - \mathbf{z}(k+1)) \quad (4.20)$$

and replacing (4.16) into (4.20), it becomes:

$$\tilde{\xi}_a(k+1) = \xi_a(k+1) - \Lambda\xi_a(k) + \Lambda\mathbf{z}(k) - \Lambda\mathbf{x}(k) + \Lambda\hat{\xi}_a(k) \quad (4.21)$$

Considering (4.9), (4.15) and (4.17), (4.21) can be rewritten as:

$$\tilde{\xi}_a(k+1) = \Delta\xi_a(k+1) + (1-\Lambda)\tilde{\xi}_a(k) \quad (4.22)$$

The disturbance estimation error follows the dynamics presented in (4.22). From (4.22) it can be verified that the disturbance observer presented in (4.15) and (4.16) is asymptotically stable with an appropriate choice of Λ and following the condition $(1-\Lambda) < 1$, and thus, the estimated disturbance is able to track the disturbance of the system.

It is possible to note that the estimation error dynamic is related to the disturbance variation $\Delta\xi_a(k+1)$. So the observer completely estimates constant disturbances and work well with slowly varying disturbances, which means that within one sampling period the disturbance variation

should not be too large since it difficulties the convergence of the error to zero [78].

In the scenario presented in this work, the disturbance variation is associated with the phase voltages applied to the machine and its variation is related to the frequency of the mechanical shaft speed.

From the combination of the discrete time sliding mode control with the proposed disturbance observer, the control law can be defined as:

$$\mathbf{u}(\mathbf{k}) = \mathbf{u}_{\text{smc}}(k) - \mathbf{H}^{-1} \hat{\boldsymbol{\xi}}_d(k) \quad (4.23)$$

Replacing the control law given in (4.23) and the term related to the discrete time sliding mode control based on Gao's approach given in (3.44) in the dynamic model presented in (2.28), it becomes:

$$\mathbf{x}(k+1) = \mathbf{x}^*(k+1) + \boldsymbol{\sigma}(k)(1 - qt_s) - \epsilon t_s \text{sign}(\boldsymbol{\sigma}(k)) + \tilde{\boldsymbol{\xi}}_d(k) \quad (4.24)$$

According to (3.41), (4.24) can be rewritten as:

$$\boldsymbol{\sigma}(k+1) = \boldsymbol{\sigma}(k)(1 - qt_s) - \epsilon t_s \text{sign}(\boldsymbol{\sigma}(k)) + \tilde{\boldsymbol{\xi}}_d(k) \quad (4.25)$$

(4.25) represents the dynamic of the controller combined with the disturbance observer. The convergence of the sliding surface to zero depends not only on the controller parameters (q , ϵ) and the sampling period as well as on the disturbance observer error.

4.4. Discrete time super-twisting control with reduced order disturbance observer

Combining the discrete super-twisting controller whose control law is shown in (3.93) with the disturbance observer proposed in Section (4.3), the control law becomes:

$$\mathbf{u}(k) = \mathbf{u}_{\text{DSTC}}(k) - \mathbf{H}^{-1} \hat{\boldsymbol{\xi}}_d(k) \quad (4.26)$$

where $\mathbf{u}_{\text{DSTC}}^2$ represents the super-twisting control law given in (3.93).

Replacing (3.93) into (4.26), the super-twisting control law combined with the disturbance observer can be designed as:

$$\mathbf{u}(k) = \mathbf{H}^{-1} (\mathbf{x}^*(k+1) - \mathbf{G}\mathbf{x}(k) - \mathbf{W}\mathbf{e}(k) - \mathbf{u}_{\text{st}}(k)) - \mathbf{H}^{-1}\hat{\boldsymbol{\xi}}_d(k) \quad (4.27)$$

Now, replacing the control law given in (4.27) into the dynamic model presented in (3.95) it becomes:

$$\begin{aligned} \mathbf{x}(k+1) &= \mathbf{G}\mathbf{x}(k) + \mathbf{W}\mathbf{e}(k) + \boldsymbol{\xi}_d(k) + \\ &+ \mathbf{H} \left[\mathbf{H}^{-1} (\mathbf{x}^*(k+1) - \mathbf{G}\mathbf{x}(k) - \mathbf{W}\mathbf{e}(k) - \mathbf{u}_{\text{st}}(k)) - \mathbf{H}^{-1}\hat{\boldsymbol{\xi}}_d(k) \right] \end{aligned} \quad (4.28)$$

$$\mathbf{x}(k+1) = \mathbf{x}^*(k+1) - \mathbf{u}_{\text{st}}(k) + \tilde{\boldsymbol{\xi}}_d(k) \quad (4.29)$$

According to (3.41), (4.29) can be rewritten and the dynamic of the controller combined with the disturbance observer can be represented by the following equations:

$$\begin{cases} \boldsymbol{\sigma}(k+1) = -\mathbf{u}_{\text{st}}(k) + \tilde{\boldsymbol{\xi}}_d(k) \\ \tilde{\boldsymbol{\xi}}_d(k+1) = \Delta\boldsymbol{\xi}_d(k) + (1-\Lambda)\tilde{\boldsymbol{\xi}}_d(k) \end{cases} \quad (4.30)$$

From (4.30) it can be concluded that the convergence of the sliding surface to zero depends on the super-twisting law and the disturbance observer error.

4.5. Current reference optimization

According to the voltage equation of the six-phase brushless DC machine presented in (2.10), it is possible to note that the inductance matrix is related to the time derivatives of the phase currents.

²From this point, the discrete time super-twisting control law defined in (3.93) will be represented by \mathbf{u}_{DSTC} .

Commonly in brushless DC motors, it is desirable that the phase currents present a square waveform so that the combination between all the phase currents generate a constant torque in the machine, as described in Section (2.2.1). However, the derivative of the square waveform results in the rising and falling edges points towards in a very high signal which, multiplied by the mutual inductances, increases considerably the effect of the coupling inductance between the phases contributing to torque oscillations.

For this reason, this section proposes an optimization in the phase current reference calculation, which has an inclination (Φ) in the rising and falling edges of the signal so that its time derivative becomes softer and consequently the effect of the magnetic coupling in the system is reduced, thereby making the achievement of a torque with minimal oscillations easier.

In order to obtain a constant torque by the interaction between the phase current and the trapezoidal back-emf, the inclination in one phase should be compensated in the other five phases and for hence the optimized current reference is given in accordance with Figure 4.2.

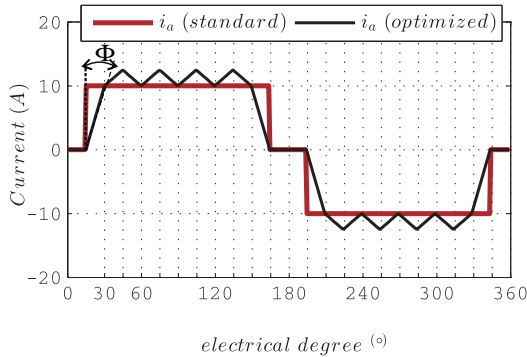


Figure 4.2.: Optimized phase current reference versus standard phase current reference.

The greater the slope of the current reference, the lower is the effect of mutual inductance, but the maximum value for this inclination is an angle of 15 electrical degrees.

The optimized phase currents, with a slope of $\Phi = 15^\circ$, the respective back-emf signals for all the six phases and the resultant electrical torque, are shown in Figure 4.3.

4.6. Simulation results

In this section, the performance of the proposed disturbance observers, combined with the current controllers and applied to the six-phase brushless DC machine, is qualitatively investigated by the simulation results carried out with the software MATLAB[®], where the algorithms are implemented with a sampling frequency of 50 kHz. The parameters of the machine used in the simulations are shown in Table 3.1.

The effect of the coupling inductances between the phases and its variation in accordance with the rotor position and the non-idealities in the back-emf are considered disturbances added to the model, which should be estimated and compensated by the disturbance observers.

It is assumed that the back-emf amplitude, calculated by the relationship between measured speed and back-emf constant, is known and compensated by a feed-forward control. This simplifies the task of the observers that should estimate just the non-idealities of the back-emf. In these simulations a scenario is considered, where 10% parameter uncertainty and a random oscillation in the crest are added to the back-emf signal as non-idealities.

Simulations with the standard current reference and the optimized current reference are presented in order to compare both these approaches.

The purpose of the simulations is to show that the proposed observers are able to estimate and compensate the disturbances present in the model. Hence, the current controller does not have to lead with high uncertainties, improving the controller dynamic response and ensuring a resultant electrical torque with minimal oscillations.

All the simulations presented in this section are performed at nominal speed (2250 rpm) and half load (1 Nm).

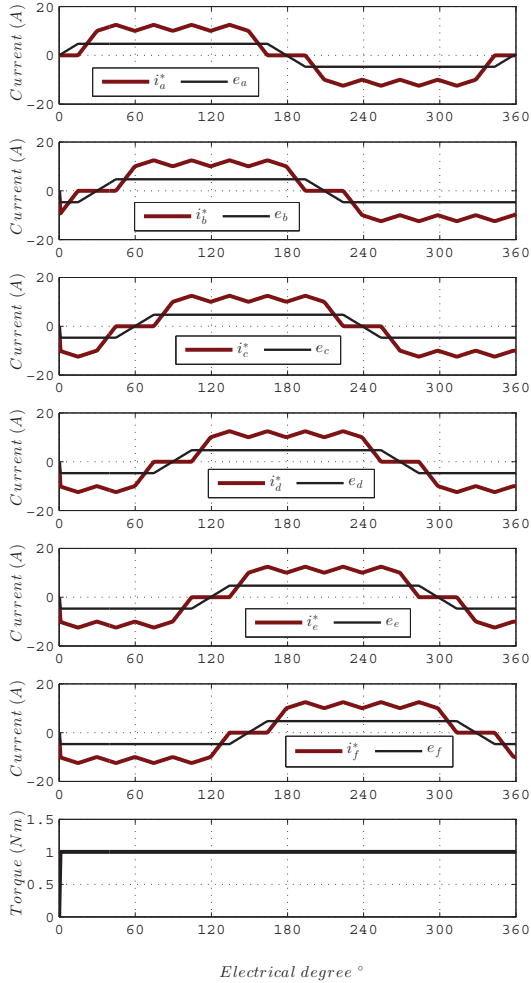


Figure 4.3.: Optimized phase currents references, phase back-emf and resultant electrical torque.

4.6.1. Discrete time sliding mode control with decoupled variable structure disturbance observer

The performance of the discrete time sliding mode control combined with a variable structure disturbance observer, is analyzed by simulation results in this section. It is very important to verify if the estimated disturbance tracks the disturbance added to the system and if it is compensated.

Figure 4.4 (a) presents the phase current A versus the standard current reference; Figure 4.4 (b) presents the tracking error for the current in phase A; Figure 4.4 (c) shows the output of the controller in combination with the observer; Figure 4.4 (d) shows the observed disturbance versus the disturbance and Figure 4.4 (e) and (f) present the electrical torque and its zoom.

Due to the discrete implementation, the control law information is actualized at each sampling period and hence the disturbance observer does not react instantly. Thus, there is a small delay between the observed value and the disturbance in the system, as verified in Figure 4.4 (d).

As investigated in the formulation of the decoupled disturbance observer, it presents a good performance when disturbances with relatively slow variation are considered since the dynamics of the observer is related to the disturbance error, as shown in (4.14). However, the disturbance associated with the magnetic coupling between the phases results in disturbances with fast variation when the standard current reference is used. For this reason, the disturbance of the system is not perfectly observed and not totally compensated and hence the oscillations in the phase currents and in the electrical torque are not reduced. In this case, the torque oscillation is about 11%.

It should be considered that as the observer in question follows a variable structure approach, an increase in the observer's gain in an attempt to improve the disturbance tracking could result in chattering to the system.

The phase current tracking error varies between $11.458A$ and $-11.5541A$. It is expected that with the use of the optimized current reference, the effect of the mutual coupling between the phases gets minimized, thereby reducing the current tracking error and improving the observer's performance.

4. Discrete time disturbance observer applied to the BLDC machine

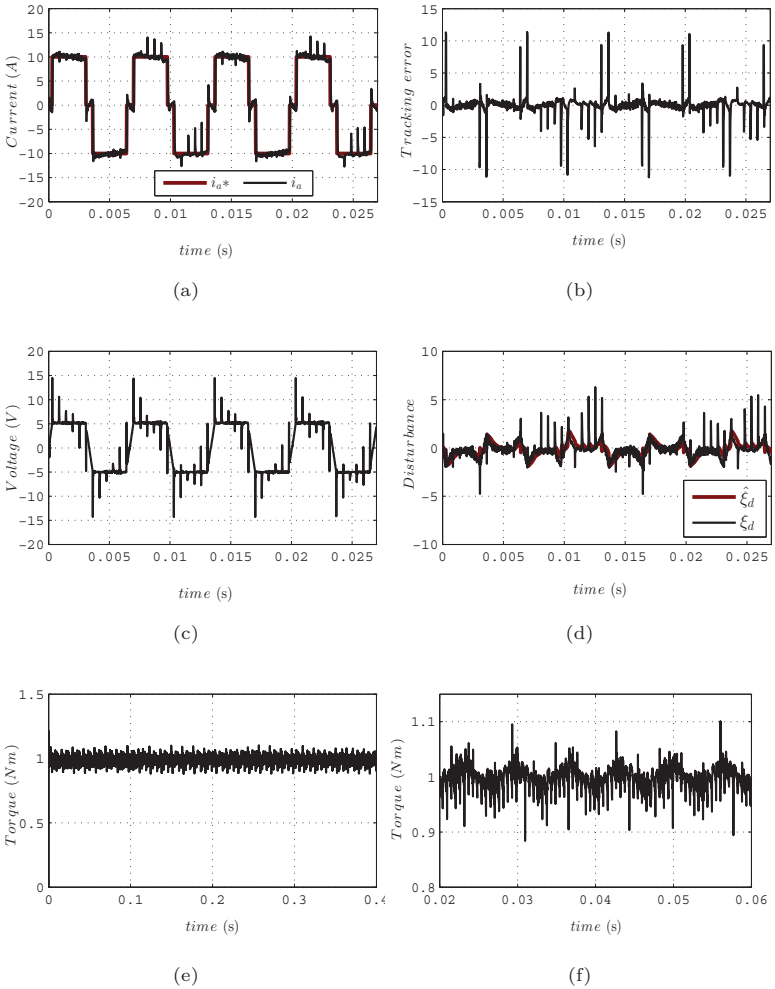


Figure 4.4.: Discrete time sliding mode control with decoupled variable structure disturbance observer. (a) Current reference (i_a^*) versus measured current (i_a) for phase A; (b) tracking error for phase A; (c) output of the current controller in combination with the disturbance observer; (d) disturbance versus estimated disturbance; (e) electrical torque; (f) zoom of electrical torque.

4.6.2. Discrete time sliding mode control with reduced order disturbance observer

Simulation results for the discrete time sliding mode control combined with a reduced order disturbance observer are shown in this section. Figure 4.5 (a) presents the phase current A versus the standard current reference; Figure 4.5 (b) presents the phase current tracking error; Figure 4.5 (c) shows the output of the controller in combination with the observer; Figure 4.5 (d) shows the observed disturbance versus the disturbance and Figure 4.5 (e) and (f) present the electrical torque and its zoom.

In this case, the difficulty to overcome the effect caused by the mutual coupling between the phases, when the standard current reference is used, is still present, as in the approach previously presented. The torque oscillation is about 10.5%. In Figure 4.5 (d), a good disturbance tracking from the disturbance observer is noted. However, it can be concluded that the control does not react fast enough to compensate the disturbances and there are oscillations in the phase currents, as shown in Figure 4.5 (a).

4.6.3. Discrete time super-twisting control with reduced order disturbance observer

The simulation results of the discrete super-twisting control, combined with a reduced order disturbance observer is analyzed in this section. Figure 4.6 (a) presents the phase current A versus the standard current reference; Figure 4.6 (b) presents the phase current tracking error; Figure 4.6 (c) shows the output of the controller in combination with the observer; Figure 4.6 (d) shows the observed disturbance versus the disturbance and Figure 4.6 (e) and (f) present the electrical torque and its zoom.

The results are very similar to the results from the discrete time sliding mode controller combined with the reduced order disturbance observer. However, the super-twisting control presents a faster dynamic response in such a manner that the discrete time sliding mode controller and the disturbances are better observed and compensated, when compared with the other presented approaches. Nevertheless, the effect of the mutual

4. Discrete time disturbance observer applied to the BLDC machine

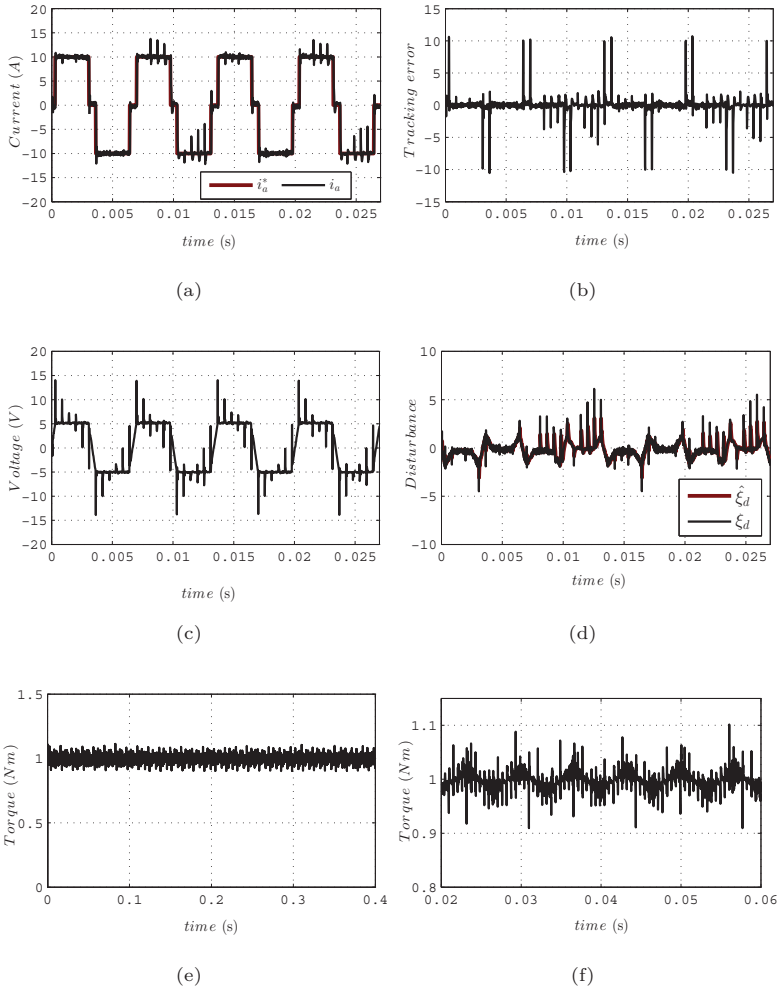


Figure 4.5.: Discrete time sliding mode control with reduced order disturbance observer. (a) Current reference (i_a^*) versus measured current (i_a) for phase A; (b) tracking error for phase A; (c) output of the current controller in combination with the disturbance observer; (d) disturbance versus estimated disturbance; (e) electrical torque; (f) zoom of electrical torque.

inductances in the phase current can be considered a very quick disturbance variation that deteriorates the performance of the observer. An alternative to making the disturbance variation in the system slower and improving the performance of the observer is the use of the optimized current reference.

Furthermore, as is noted in Figure 4.4 (b), Figure 4.5 (b) and Figure 4.6 (b), the phase current tracking error varies between 10.7 A and $-10.7A$. This error is associated with an abrupt modification in the standard current reference (from zero until 10A, in this case) and it is expected that the use of the optimized current reference contributes to a reduction in the tracking error. The results of the proposed controller combined with disturbance observers and using an optimized current reference will be shown in the next sections.

4.6.4. Discrete time sliding mode control with decoupled variable structure disturbance observer and optimized current reference

This section presents the simulation results for the discrete time sliding mode control combined with a variable structure disturbance observer and using the optimized current reference. A slope of 15° electrical degree for the calculation of the new current reference is considered.

Figure 4.7 (a) presents the phase current A versus the optimized current reference; Figure 4.7 (b) presents the phase current tracking error; Figure 4.7 (c) shows the output of the controller in combination with the observer; Figure 4.7 (d) shows the observed disturbance versus the disturbance and Figure 4.7 (e) and (f) present the electrical torque and its zoom.

Analysing the response of the current in Figure 4.7 (a) and the current tracking error in the Figure 4.7 (b), it is verified that the effect of the magnetic coupling between the phases is substantially minimized and results in a phase current tracking error varying between 2.74A and 2.92A. In Figure 4.7 (d), a reduction in the disturbance is also noted and the resulting torque oscillation is about 6%, thereby proving the efficiency of the proposed optimized current reference. There is a delay between the

4. Discrete time disturbance observer applied to the BLDC machine

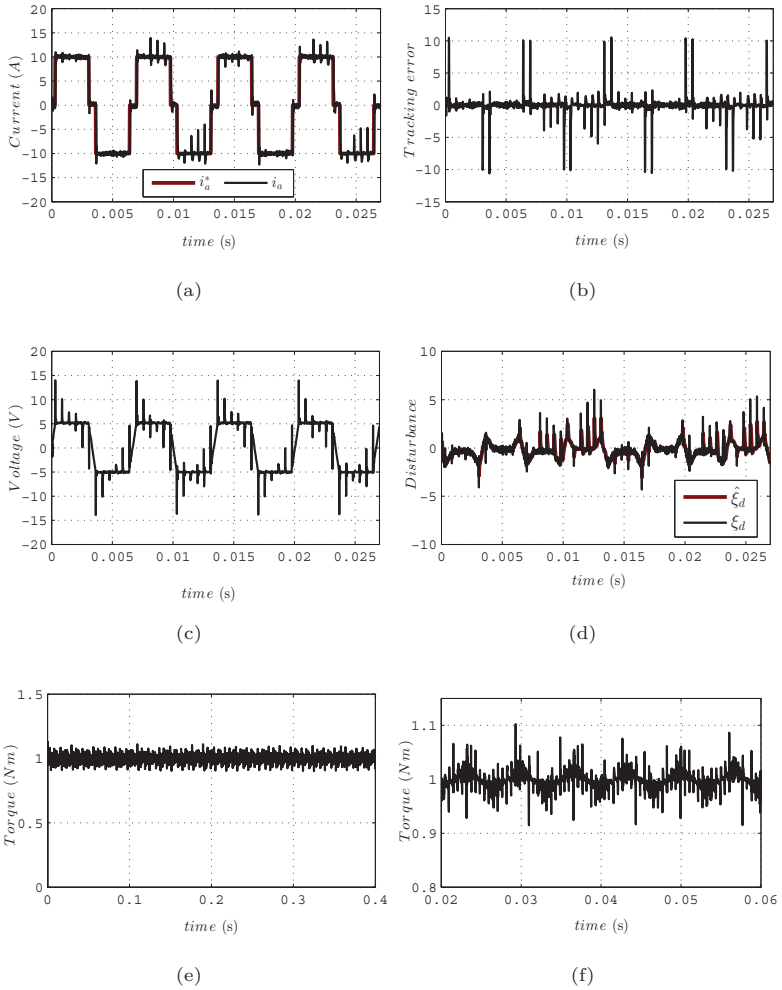


Figure 4.6.: Discrete time super-twisting control with reduced order disturbance observer. (a) Current reference (i_a^*) versus measured current (i_a) for phase A; (b) tracking error for phase A; (c) output of the current controller in combination with the disturbance observer; (d) disturbance versus estimated disturbance; (e) electrical torque; (f) zoom of electrical torque.

disturbance and the observed disturbance, but that does not compromise the observer performance.

4.6.5. Discrete time sliding mode control with reduced order disturbance observer and optimized current reference

This section analyzes the simulation results for the discrete time sliding mode control combined with the reduced order disturbance observer and the optimized current reference. Figure 4.8 (a) presents the phase current A versus the optimized current reference; Figure 4.8 (b) presents the phase current tracking error; Figure 4.8 (c) shows the output of the controller in combination with the observer; Figure 4.8 (d) shows the response of the observed disturbance versus the disturbance and Figure 4.8 (e) and (f) present the electrical torque and its zoom.

With the use of the optimized current reference there is an improvement in the performance of the controller combined with the observer, resulting in a torque with reduced oscillations — in this case about 5% — even in a system where the model is not well known. It is concluded that the new current reference reduces the effect of the coupling inductance between the phases, or, in other words, it reduces the disturbance in the system related to this coupling as observed in Figure 4.8 (d). The disturbance tracking carried out by the proposed observer presents a good response, estimating both disturbances relating to the back-emf as well as to the magnetic coupling.

4.6.6. Discrete time super-twisting control with reduced order disturbance observer and optimized current reference

This section presents the simulation results for the discrete time super-twisting control combined with the reduced order disturbance observer and the optimized current reference.

4. Discrete time disturbance observer applied to the BLDC machine

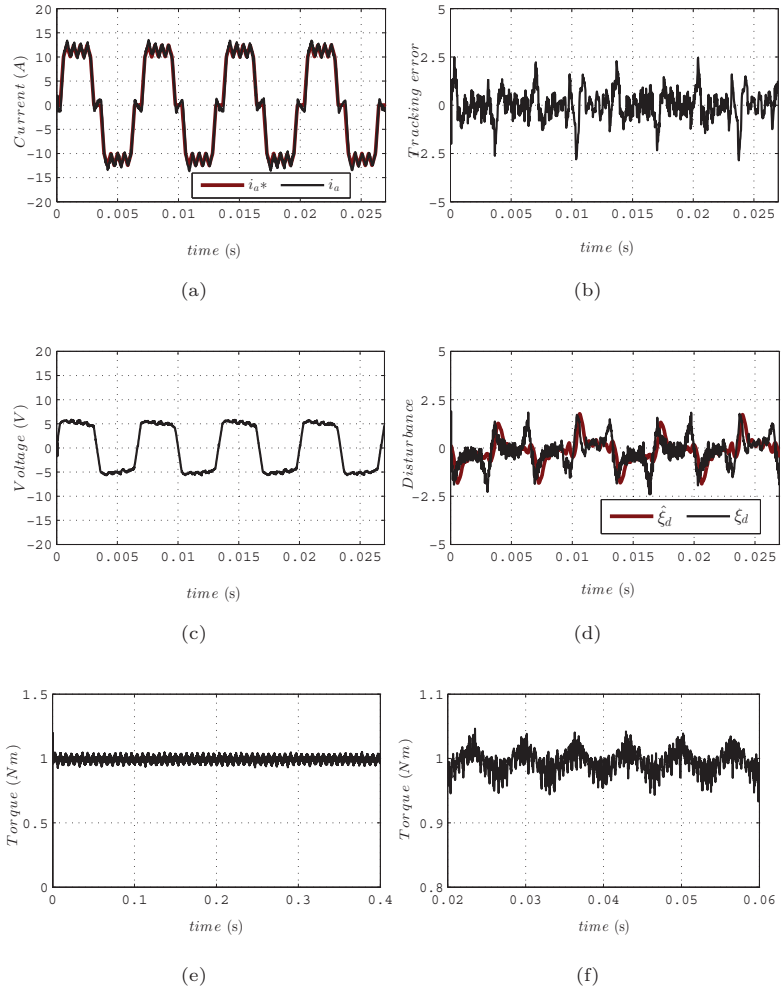


Figure 4.7.: Discrete time sliding mode control with decoupled variable structure disturbance observer and optimized current reference. (a) Current reference (i_a^*) versus measured current (i_a) for phase A; (b) tracking error for phase A; (c) output of the current controller in combination with the disturbance observer; (d) disturbance versus estimated disturbance; (e) electrical torque; (f) zoom of electrical torque.

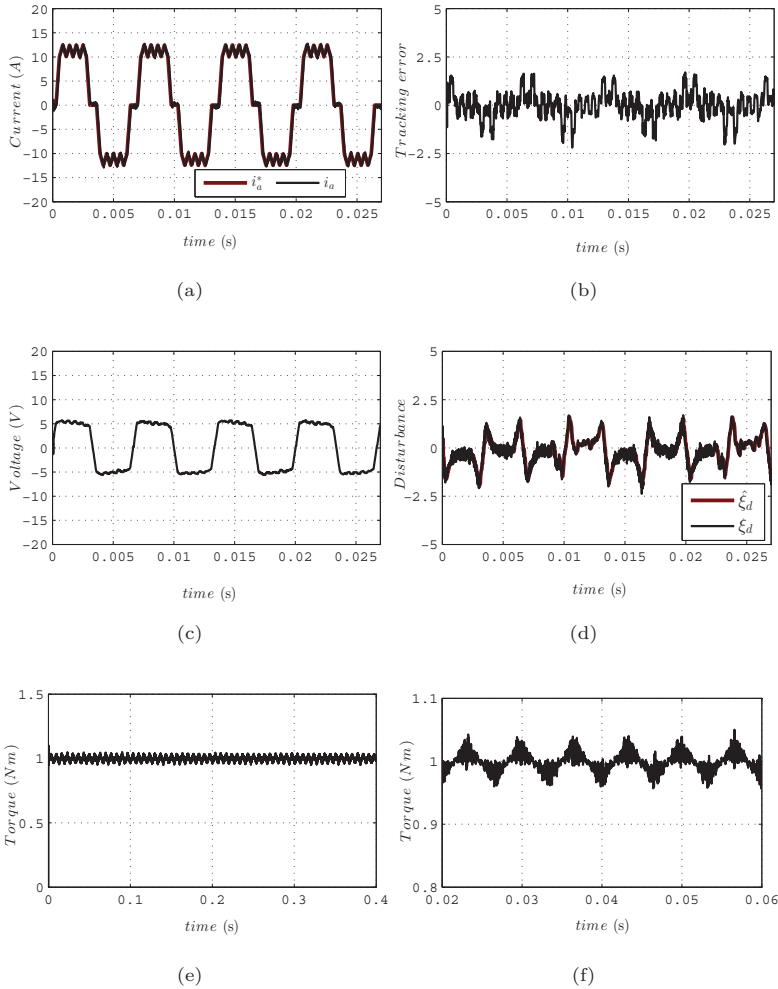


Figure 4.8.: Discrete time sliding mode control with reduced order disturbance observer and optimized current reference. (a) Current reference (i_a^*) versus measured current (i_a) for phase A; (b) tracking error for phase A; (c) output of the current controller in combination with the disturbance observer; (d) disturbance versus estimated disturbance; (e) electrical torque; (f) zoom of electrical torque.

Figure 4.9 (a) presents the phase current A versus the optimized current reference; Figure 4.9 (b) presents the phase current tracking error; Figure 4.9 (c) shows the output of the controller in combination with the observer and Figure 4.9 (d) shows the response of the observed disturbance versus the disturbance. Figure 4.9 (e) and (f) present the electrical torque and its zoom.

The results using the discrete time super-twisting control combined with the disturbance observer are very similar to the results presented for the first-order discrete time sliding mode control that is based on the Gao's approach combined with the same disturbance observer, with a torque oscillation of about 5.5%. The advantage of the use of the discrete time super-twisting control is a faster dynamic response and absence of the chattering effect.

4.6.7. Summary

This chapter presented the formulation and analysis in the discrete time domain of two proposed observers, combined with discrete time sliding mode controllers, in order to improve the controller robustness, thereby ensuring an electrical torque with minimal oscillations for a system where the plant is not totally known. The purpose of the observers is to estimate the disturbance in the system and to compensate this disturbance in the control law. Furthermore, an optimized current reference is introduced in order to minimize the effect of the magnetic coupling between the phases, thereby reducing the resultant disturbances in the system. With the use of the optimized current, a reduction of about 5% in the torque oscillation is obtained as well a reduction in the tracking error. With a standard current reference, the tracking error varies between $10A$ and $-10A$; with the optimized current, a variation from $2A$ to $-2A$ in the current tracking error is obtained. The simulation results are carried out to verify the efficiency of the proposed control techniques. In the next chapter, an experimental investigation of the control strategies applied to the six-phase BLDC machine will be presented to prove the practical effectiveness of the proposed techniques.

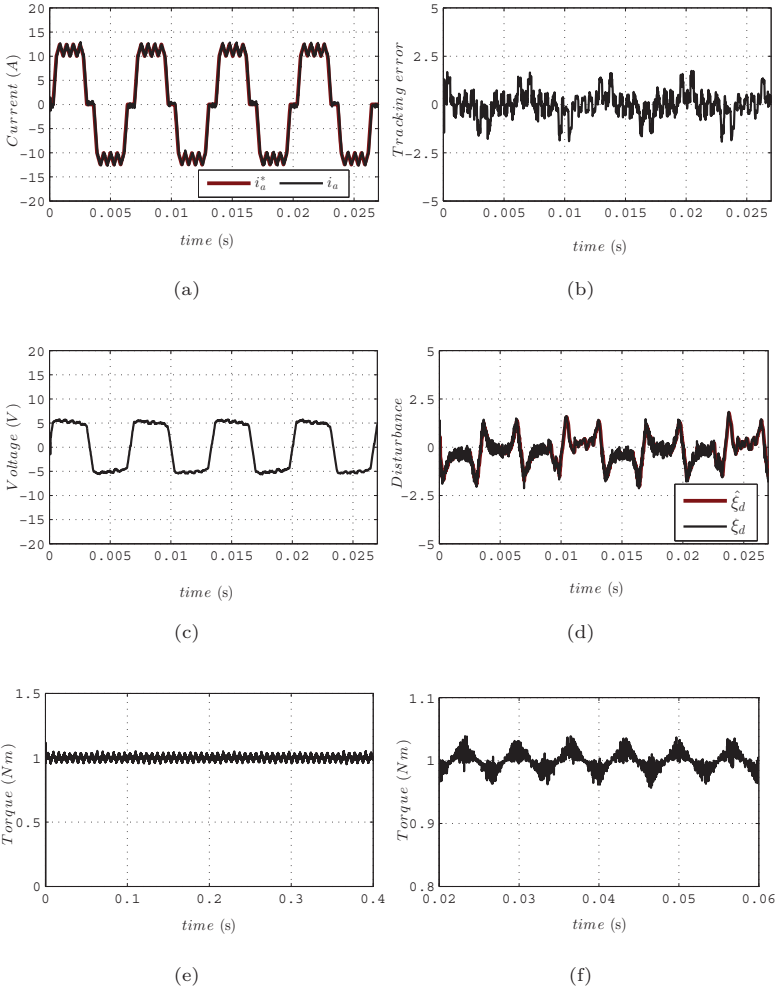


Figure 4.9.: Discrete time super-twisting control with reduced order disturbance observer and optimized current reference. (a) Current reference (i_a^*) versus measured current (i_a) for phase A; (b) tracking error for phase A; (c) output of the current controller in combination with the disturbance observer; (d) disturbance versus estimated disturbance; (e) electrical torque; (f) zoom of electrical torque.

5. Experimental Results

In this chapter the experimental investigation of the proposed discrete time sliding mode controllers combined with the disturbance observers will be presented to validate the theoretical analysis developed in the previous chapters. Furthermore, this chapter describes the experimental setup built to verify the performance of the control strategies proposed in this work.

5.1. Description of the experimental setup

The purpose of this work is to investigate the performance of the controllers based on the sliding mode approach applied to a fault-tolerant six-phase BLDC machine. A prototype BLDC machine, shown in Figure 5.1, is used in this experimental investigation and its main specifications are given in Table 3.1. The machine was constructed by Krebs und Aulich GmbH with the design and concept developed by [79–81].



Figure 5.1.: Six-phase BLDC machine.

The experimental setup developed to investigate the application of the control strategies to the six-phase BLDC machine is shown in Figure 5.2.

The components of the experimental setup are identified with numbers from 1 to 7 in the figure.

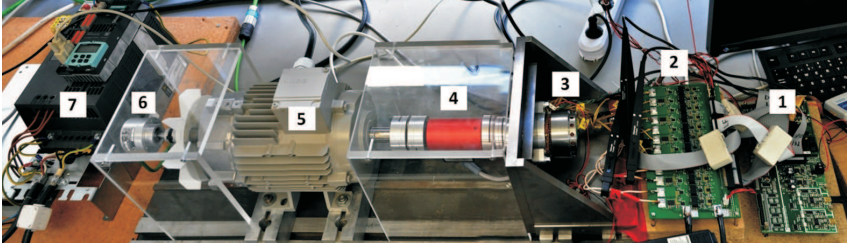


Figure 5.2.: Experimental setup for the investigation of control strategies applied to the six-phase BLDC machine.

The six-phase brushless DC machine (3) is connected with a 2.2 kW asynchronous machine (5) employed as load machine and powered by a Siemens converter (7). The control of the asynchronous machine is carried out with a specific tool from the Siemens System (Control Unit) and the angular position is measured by an incremental encoder (6). The machines are connected by a mechanical shaft adapter (4), where a torquemeter is installed to measure the resultant torque and the speed of the system.

The aim is to generate with the load machine a braking torque on the BLDC machine. To track the desired speed and maintain it in the value defined in the speed control loop, the BLDC machine control generates a torque in opposition to the braking torque generated by the asynchronous machine. The resultant torque between both machines is measured with a torquemeter and shown in an oscilloscope. Through the measurement of the resultant torque of the system, the performance of the proposed controllers would be verified.

Both machines are controlled separately. While the asynchronous machine is controlled through the Siemens control unit connected with a computer by a RS232 transmission protocol, the BLDC machine drive is controlled by an FPGA system (1).

The FPGA board, shown in Figure 5.3, was developed by the KDEE group (Centre of Competence for Distributed Electrical Power Technology).

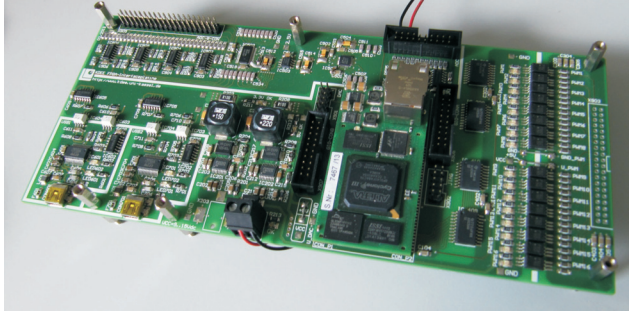


Figure 5.3.: FPGA Board.

The motivation for using an FPGA system was the high numbers of drive signals required in this application for measurements and command signals, as the IOs and PWM units needed to feed the six-phase H-bridge converter.

Furthermore, considering that the mathematical operations in the control law involve the multiplication of a 6×6 matrix (\mathbf{G} , \mathbf{H} , \mathbf{W}) by 6×1 vector, the microprocessor should present a high computation capability.

Another factor that motivates the implementation in an FPGA system is that the performance of the discrete time sliding mode control depends on the sampling period, since the quasi-sliding mode bandwidth is related to the sampling period. In this application, the implementation of the proposed control strategies with 50 kHz sampling frequency have been achieved by programming the FPGA system in VHDL code. The software development was carried out with the support of the Digital Technology Group from the University of Kassel.

According to the control structure of the BLDC machine, as shown in Figure 3.1, in the external loop the speed control is carried out, while the internal loop controls the phase current. In order to control the speed, the speed measurement is needed. The speed measurement is carried out through the Hall sensor signals. The six Hall sensor signals generated by

the sensors embedded into the machine are digital signals and, for this reason, are read by IOs ports in the FPGA. Detecting the rising edge of the Hall sensor signal, its period is achieved and it corresponds to the electrical period in the machine, as shown in Figure 5.4.

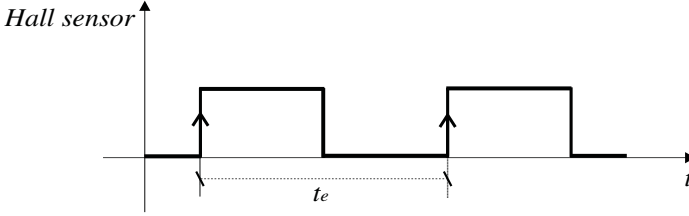


Figure 5.4.: Hall sensor period.

With the Hall sensor signal period it is possible to calculate the angular speed from the machine by the equation:

$$n_{rpm} = \frac{60}{P t_e} \quad (5.1)$$

where P is the number of pole pairs and t_e is the electrical period.

For a better resolution, the mean value of the six Hall sensor signal's periods are considered in the speed calculation.

Besides being used for the speed measurement, the Hall sensor signals are very important to define the block commutation sequence, as was presented in Table 2.1.

For the current control, each phase current is measured by a current sensor from Allegro (ACS710) and these values are read by the ADC channels of the FPGA board. An algorithm is developed in VHDL code to generate the optimized current reference by using the speed control output and the Hall sensor signal from phase A.

To ensure the fault tolerance of the system, each phase is considered as a single module and a multiphase converter was developed to attend this requirement. The multiphase converter (2) is composed by six H-bridges that feed each phase from the BLDC machine. The multiphase converter is shown in Figure 5.5. The converter topology for one phase is shown in

5. Experimental Results

Figure 2.8 and it is the same for all the other five phases. The switches used in this application are MOSFETS (IRFH5250PbF) from International Rectifier. Moreover, 12V has been applied to the DC link voltage.

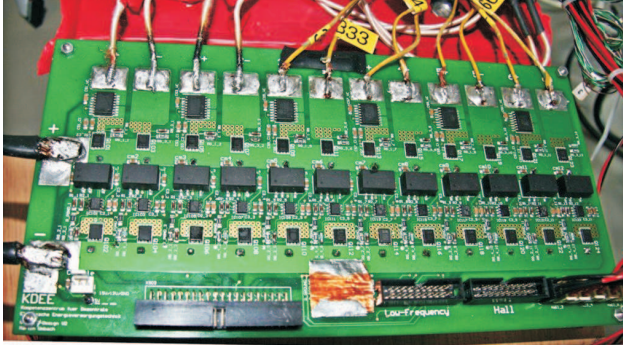


Figure 5.5.: Six-phase H-Bridge converter.

At those points where the back-emf is not constant, the phase current should be zero. This can be realized by the control, but an easy way to bring the current to zero is to open all the H-bridge switches at the points of non-constant back-emf. For this purpose, a reset signal is generated for each phase at those points where the current should be zero. So, according to Figure 5.6, if the reset signal is high, the four switches are open and no current flows through the phase H-bridge.

As mentioned before, the Hall sensor signals are very important to define the commutation sequence in the BLDC machine. However, the Hall sensor's signal changes its state only if the machine rotates. Therefore, the machine must be started in an open loop from standstill until a desired speed and so it should be switched to a closed loop. Furthermore, there is another situation where the machine is not in the open loop and not in the closed loop but in a failure mode. In the failure mode, if a fault is detected — for example, an overcurrent in a phase — the PWM signals of all switches are disabled and no current flows through the converter and the machine so that the system goes to standstill. To control it again, the machine should be started once more in the open loop. The three

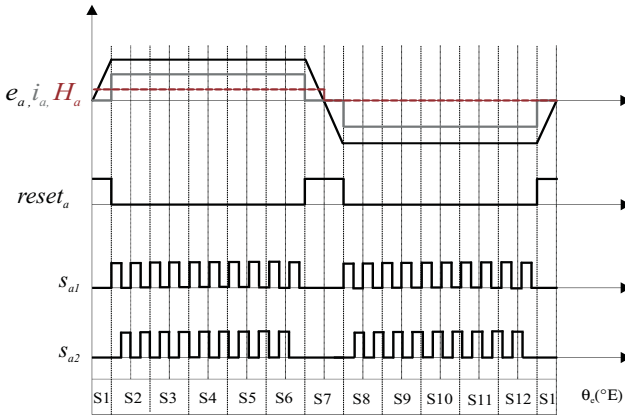


Figure 5.6.: Reset signal from phase A.

modes (open loop, closed loop and failure mode) are programmed as state machine in VHDL code in the FPGA, as shown in the diagram below:

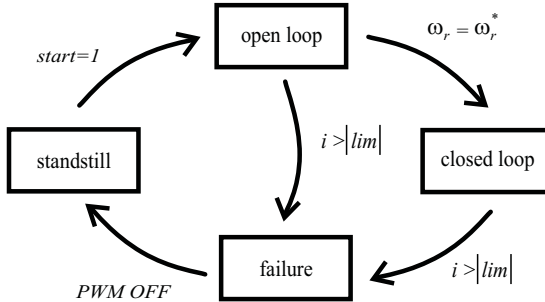


Figure 5.7.: State machine for the six-phase BLDC machine control.

5.1.1. Unipolar four-quadrant PWM technique

A unipolar four quadrant PWM modulation approach is chosen for this application. Considering that the machine inductance is very low, a high switching frequency is needed in order to avoid a high ripple in the phase

currents. A carrier wave with 50 kHz sampling frequency is employed for the modulation.

The main motivation for the application of this modulation technique relating to the six-phase brushless machine is that it doubles the frequency seen by the machine.

Considering the full bridge converter shown in Figure 2.8, the pulse signals for the switches s_{a2} and s_{a4} are complementary signals of the pulse signals s_{a1} and s_{a3} , respectively. The dead time between each complementary signal is $1\mu\text{s}$.

The triangular carrier wave varies from -1 to 1. It is important to consider that the left (s_{a1} and s_{a3}) and the right (s_{a2} and s_{a4}) PWM duty cycles must be equal, but with opposite polarity — what means that these signals are shifted one from another in 180° . Figure 5.8 shows the carrier wave, duty cycles and gate signals generated by the modulation, considering 0.5 duty cycle for the switches of the left converter side and -0.5 for the switches of the right converter side.

From Figure 5.8, considering t_1 the period of the carrier wave and t_2 the period of signal seen by the machine, it is possible to notice that the signal seen by the machine has a duty cycle of 0.5 (or 50%) and double PWM frequency, obtained from the combination of the left and right converter side gate signals. Even if the machine sees the double PWM frequency (100 kHz in this case), the switches still switch with the frequency of the carrier wave (50 kHz), not producing many losses in the converter.

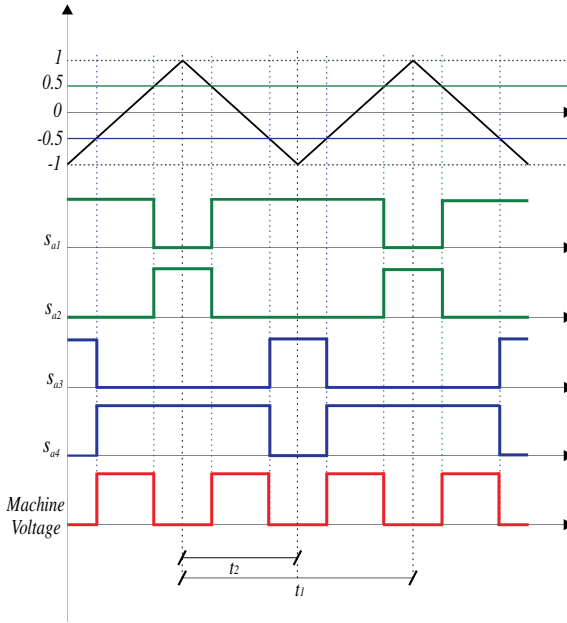


Figure 5.8.: Unipolar four-quadrant PWM technique.

Hereafter, the experimental results of the proposed current control strategies, investigated when the system is in the closed loop, will be presented. The measurements are carried out at 400 rpm and half load in order to investigate the controller performance at low speed. But also, as considered in the simulations, the performance of the controllers will be analyzed at a nominal speed and half load.

Most of the experimental results presented in this chapter use the optimized current reference with 15° slope, since, according to the simulation results, the best performance is achieved with the optimized current reference.

In the experimental investigation, it is also assumed that the back-emf amplitude, calculated by the relationship between the measured speed and the back-emf constant, is known and is compensated by a feedforward control, even when the current controller is combined with a disturbance

observer, simplifying the task of the observers that should estimate only the non-idealities of the back-emf.

The aim is to verify by the experimental measurements the dynamic response of the proposed current controllers and whether the proposed observers are able to estimate and compensate the disturbances present in the model.

A qualitative comparison of the resultant electrical torque between the presented strategies is carried out in order to verify which strategy is more adequate for the application in the six-phase brushless DC machine, ensuring a torque with minimal oscillations, even considering the fact that the model that describes the machine is just approximately known.

5.2. Discrete time proportional-integral current controller

In this section, the performance of the classical proportional-integral controller applied to the multiphase brushless DC machine is experimentally investigated. Figure 5.9 shows the measurements carried out with the optimized current reference at 400 rpm and half load. The gain parameters are defined in accordance with the approach presented in Appendix A.1. Figure 5.9 (a) shows the measured currents in phases A, B and C; while Figure 5.9 (b) shows the measured current versus the optimized current reference for phase A and Figure 5.9 (c) shows the tracking error for the phase current in phase A. Also, Figure 5.9 (d) shows the output of the current controller and Figure 5.9 (e) the resultant electrical torque.

It can be concluded that the performance of the proportional-integral controller with an optimized current reference is satisfactory at low speeds, despite the low dynamic response of the controller. The next measurements presented in Figure 5.10 show the results for the PI current controller at a nominal speed and half load.

Despite a good reference track at low speeds, at nominal or at higher speeds, for a same controller gain, the dynamic of PI controller is not fast enough to track the current references. At high speeds, the current controller should react rapidly so that a variation of the controller gain design would be appropriate. For the results presented in Figure 5.11,

an adaptation in the gain parameter is carried out in order to make the dynamic response faster at nominal speed.

It is noticed that an adjustment in the gain parameters improves the performance of the PI controller and, therefore the use of an adaptive gain parameter in the PI controller could be a good alternative. However, it should be considered the fact that the classical PI controller has a limited bandwidth with a poor stability margin and, hence an increase in the control parameters could make the control response more oscillatory and consequently, leads the control to the instability.

Despite the improvement in the reference tracking achieved with the gain adjustment, the PI controller presents a poor dynamic response, which reduces the operation range of the BLDC drive. Furthermore, due to the linear nature of classical PI controller, this kind of controller is not robust enough to lead with the parameter variations and with the non-idealities added to the nominal model.

Given the fact that the machine model is just approximately known and is very complex for building an accurate model; which exactly describes the machine, the use of a robust controller based on the sliding mode design that is an appropriate tool for solving problems of a nonlinear nature and is not affected by the parameter variation and uncertainties in the model seems to be adequate.

5. Experimental Results

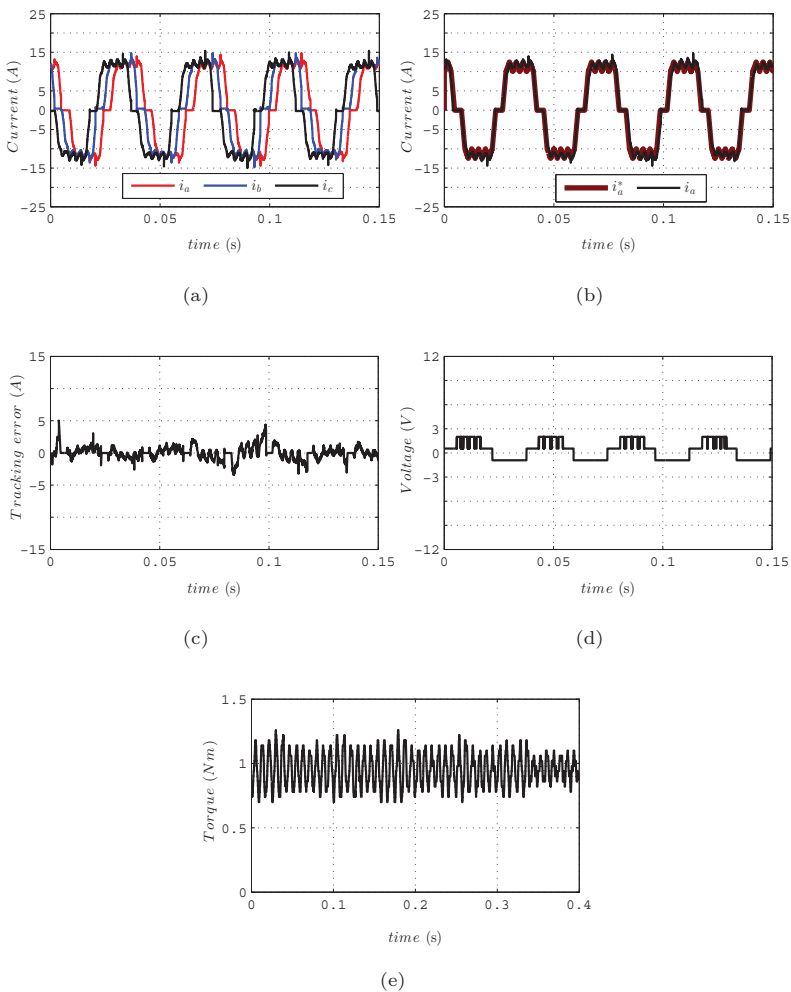


Figure 5.9.: Measurements with PI current controller and optimized current reference at 400 rpm/1Nm. (a) Measured current for phase A, B and C; (b) current reference (i_a^*) versus measured current (i_a) for phase A; (c) tracking error for phase A; (d) output of phase A current controller; (e) electrical torque.

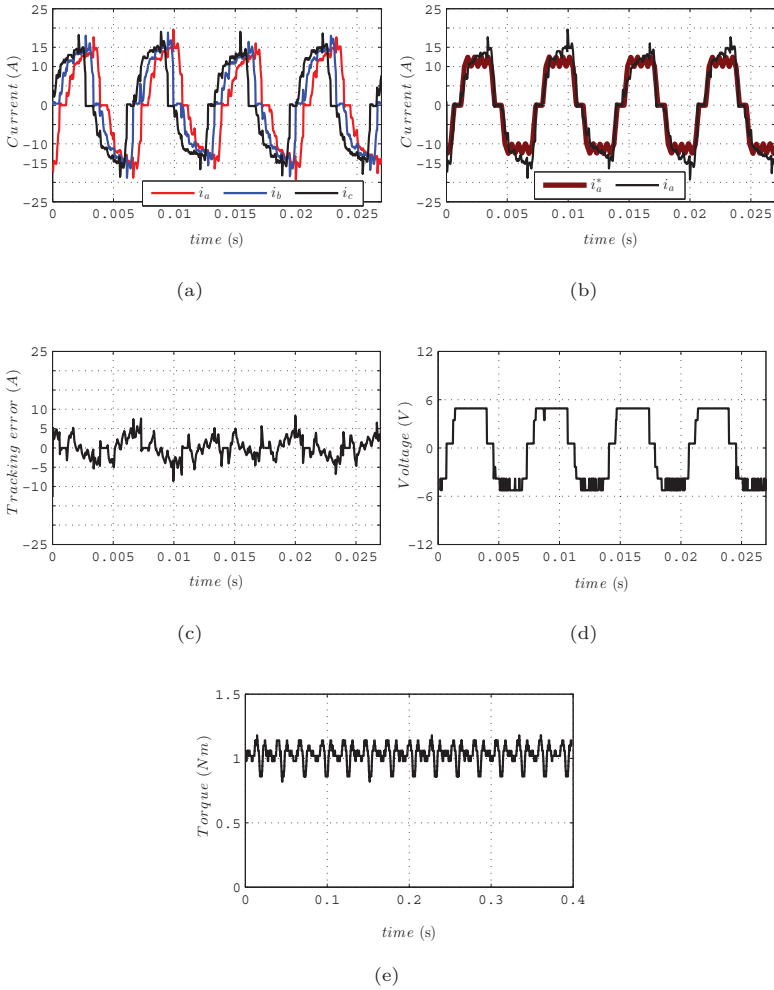


Figure 5.10.: Measurements with PI current controller and optimized current reference at 2250 rpm/1Nm. (a) Measured current for phase A, B and C; (b) current reference (i_a^*) versus measured current (i_a) for phase A; (c) tracking error for phase A; (d) output of phase A current controller; (e) electrical torque.

5. Experimental Results

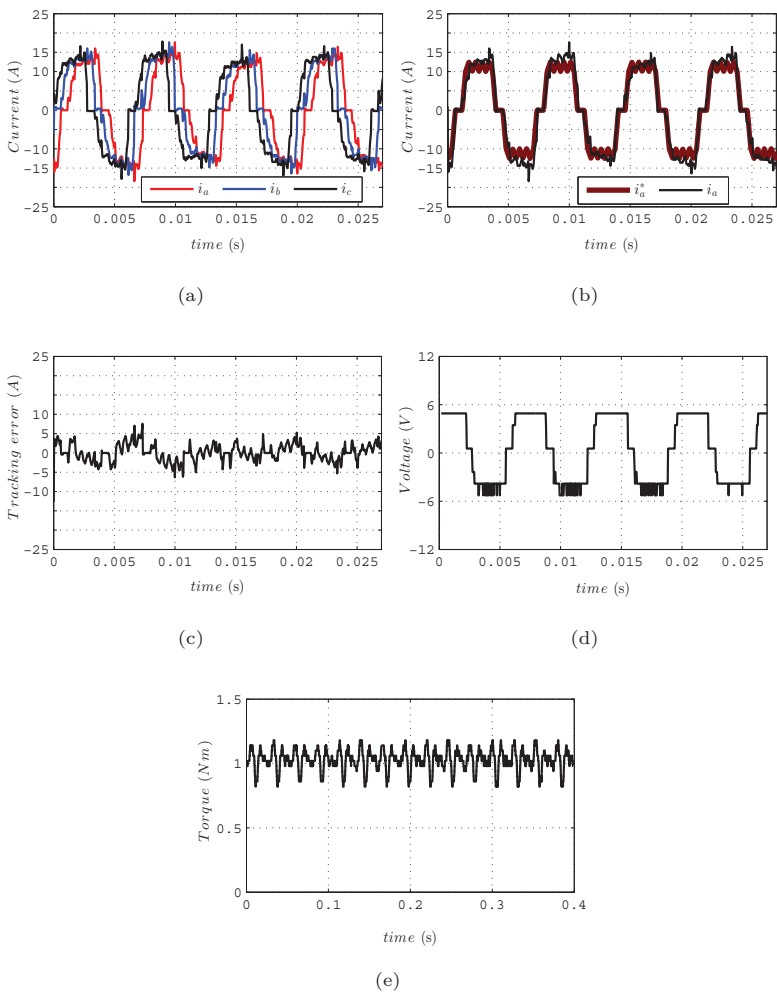


Figure 5.11.: Measurements with PI current controller and optimized current reference at 2250 rpm/1Nm with gain parameter adjustment. (a) Measured current for phase A, B and C; (b) current reference (i_a^*) versus measured current (i_a) for phase A; (c) tracking error for phase A; (d) output of phase A current controller; (e) electrical torque.

5.3. Discrete time sliding mode controller based on Gao's approach

The aim of the first experimental investigations is to verify the performance of the proposed discrete time sliding mode controller, without considering the disturbance observers. This section will present the experimental results of the discrete time sliding mode controller, based on Gao's approach, applied to the multiphase BLDC machine. For the sake of comparison, the experimental results with the standard current reference are shown in Figure 5.12.

Figure 5.12 (a) shows the measured currents in phases A, B and C; Figure 5.12 (b) shows the measured current versus the standard current reference for phase A and Figure 5.12 (c) presents the tracking error for the phase current in phase A. Figure 5.12 (d) shows the output of the current controller and Figure 5.12 (e) the resultant electrical torque.

A fast dynamic response and a good reference tracking with the sliding mode based controller are noticed. However, the effect of the coupling between the phases is evident in the peaks in the phase currents, resulting in oscillations in the electrical torque — which is not desired. Moreover, the current peaks contribute to increase the converter losses and consequently the temperature, thereby decreasing the BLDC drive efficiency.

Figure 5.13 shows the results of the same case presented before in Figure 5.12 but with the optimized current reference.

The measurements presented in Figure 5.13 confirms the effectiveness of the optimized current reference when compared with the results presented in Figure 5.12. It is verified that the tracking error is considerably reduced with the use of the optimized current reference, since it minimizes the effect of the mutual inductance in the phase currents. At low speeds, the performance of the controller presents a good dynamic response and good reference tracking. It is also noticed that being a controller based on sliding mode approach, the chattering effect is not present by using the appropriate gains for the control parameters. Considering that the aim is to achieve a satisfactory performance in the entire operation range, the results at a nominal speed are shown in Figure 5.14.

5. Experimental Results

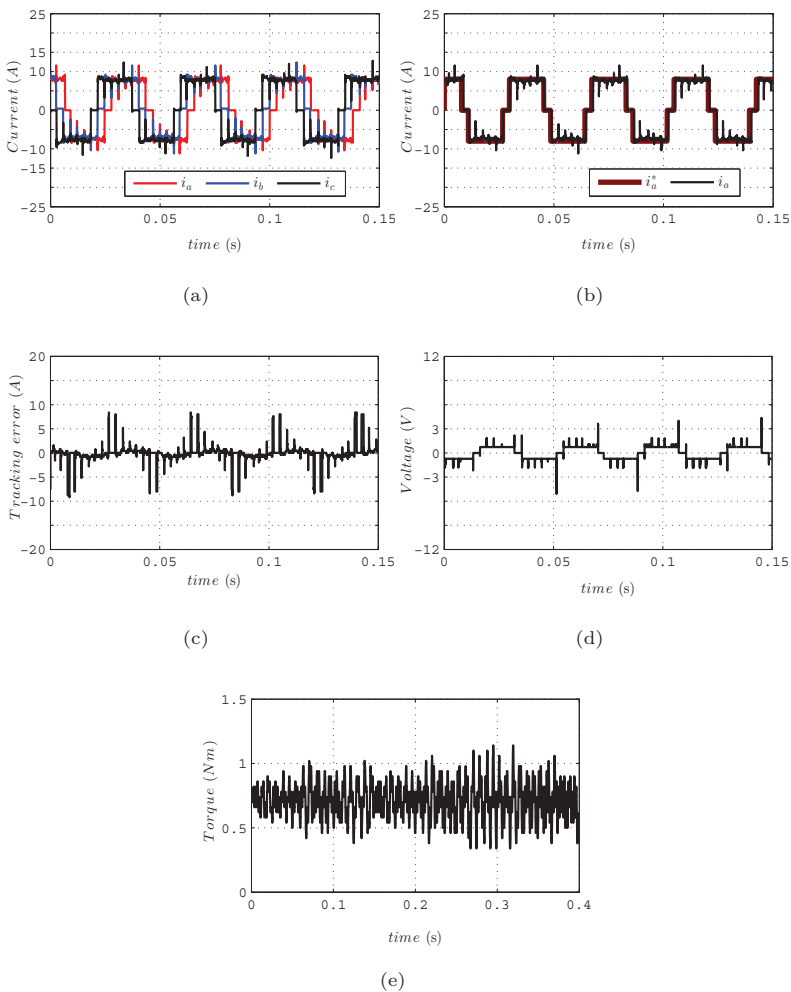


Figure 5.12.: Measurements with discrete time sliding mode current controller at 400 rpm/0.75Nm, with standard current reference. (a) Measured current for phase A, B and C; (b) current reference (i_a^*) versus measured current (i_a) for phase A; (c) tracking error for phase A; (d) output of phase A current controller; (e) electrical torque.

5.3. Discrete time sliding mode controller based on Gao's approach

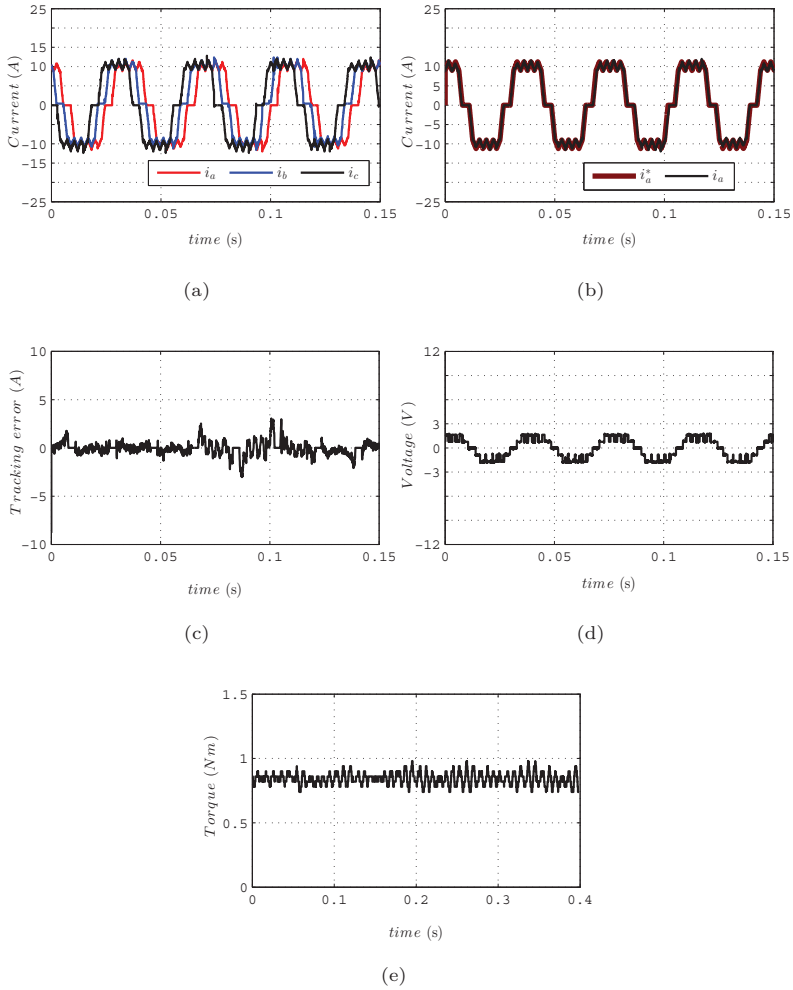


Figure 5.13: Measurements with discrete time sliding mode current controller at 400 rpm/0.85 Nm, with optimized current reference. (a) Measured current for phase A, B and C; (b) current reference (i_a^*) versus measured current (i_a) for phase A; (c) tracking error for phase A; (d) output of phase A current controller; (e) electrical torque.

It can be concluded that the performance of the discrete time sliding mode controller is satisfactory — both on low speeds as on high speeds — even without the disturbance observer. In this case, the back-emf is not observed and only its amplitude that is calculated with the information about the speed and the back-emf constant is compensated. Despite the model uncertainties, a good control performance is noted and it ensures a resultant torque with few oscillations, as shown in Figure 5.14 (e). It is expected with the combination of the controller with a disturbance observer, an improvement in the reference tracking and in the dynamic response, since all the back-emf non-idealities and uncertainties of the system are observed and compensated in this manner.

5.4. Discrete time super-twisting sliding mode controller

The experimental investigation of the discrete time second-order sliding mode control based on the super-twisting algorithm and applied to the multiphase brushless DC machine is carried out in this section.

Also, in this case, no disturbance observer is used. The aim is to verify the robustness of the proposed controller against uncertainties in the model. A very fast dynamic behavior, good reference tracking and no chattering are expected with the use of the second-order sliding mode algorithm.

The first measurement is carried out at low speeds. Figure 5.15 (a) shows the measured currents in phases A, B and C; Figure 5.15 (b) presents the measured current versus the optimized current reference for phase A and Figure 5.15 (c) depicts the tracking error for the phase current in phase A. Also, Figure 5.15 (d) shows the output of the current controller and Figure 5.15 (e) the resultant electrical torque.

The measurement results at nominal speed and half load are shown in Figure 5.16.

A good control performance with very fast dynamic response even in the model with uncertainties is verified by Figure 5.16 (a) and (b). The gain parameters are adjusted in order to ensure a good correspondence between the current reference and measured current and there is no chattering in the system even with high gain parameters.

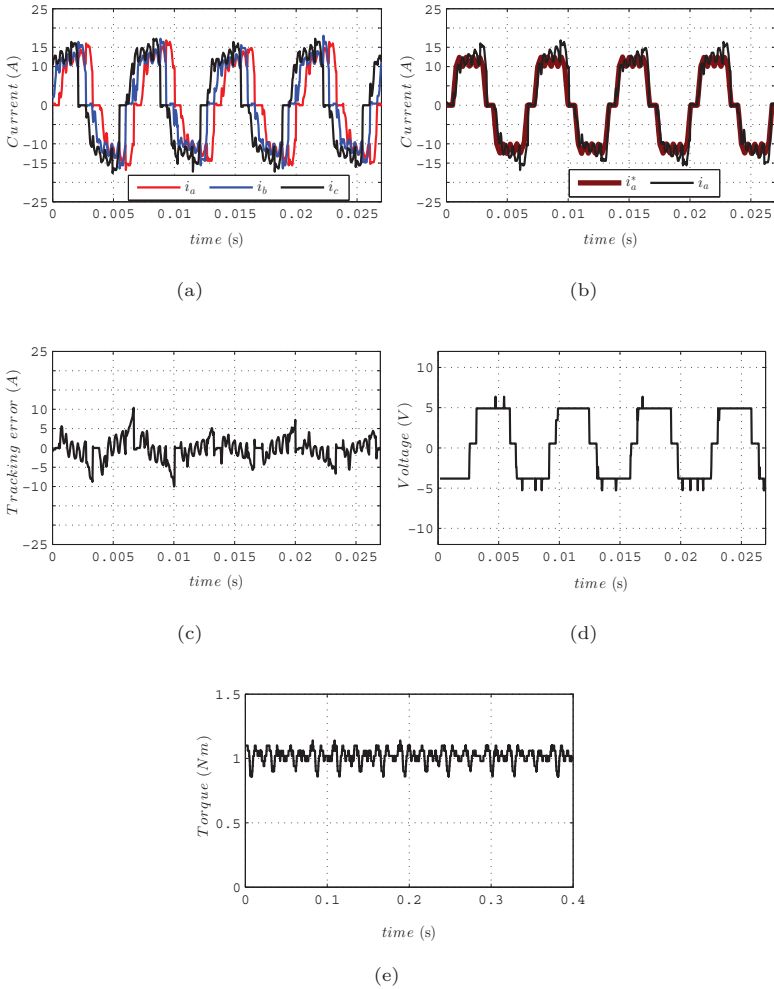


Figure 5.14.: Measurements with discrete time sliding mode current controller at 2250 rpm/1 Nm, with optimized current reference. (a) measured current for phase A, B and C; (b) current reference (i_a^*) versus measured current (i_a) for phase A; (c) tracking error for phase A; (d) output of phase A current controller; (e) electrical torque.

5. Experimental Results

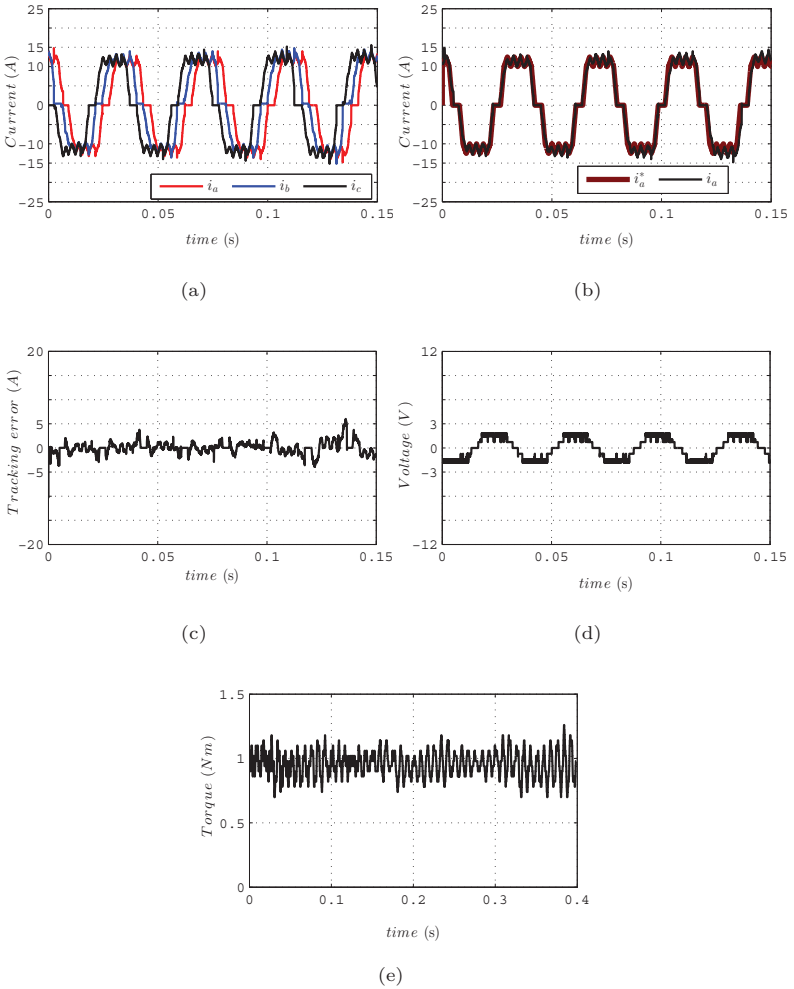


Figure 5.15.: Measurements with discrete super-twisting current controller at 400 rpm/1 Nm, with optimized current reference. (a) Measured current for phase A, B and C; (b) current reference (i_a^*) versus measured current (i_a) for phase A; (c) tracking error for phase A; (d) output of phase A current controller; (e) electrical torque.

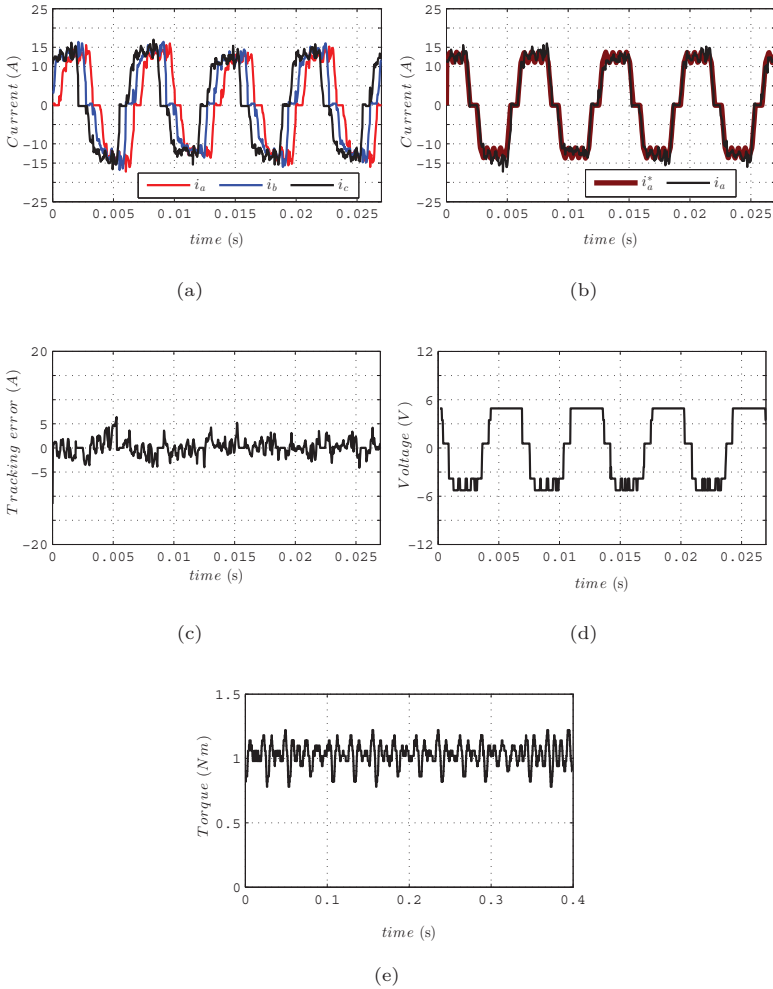


Figure 5.16.: Measurements with discrete super-twisting current controller at 2250 rpm/1 Nm, with optimized current reference. (a) Measured current for phase A, B and C; (b) current reference (i_a^*) versus measured current (i_a) for phase A; (c) tracking error for phase A; (d) output of phase A current controller; (e) electrical torque.

5.5. Discrete time sliding mode controller based on Gao's approach with decoupled disturbance observer

One of the topics addressed in this work is the estimation of the disturbance in the six-phase BLDC model. These algorithms have been developed in Chapter 4 and here, the obtained experimental results are presented. The first observer to be investigated is a decoupled disturbance observer based on the sliding mode approach.

In Figure 5.17, the results of the discrete time sliding mode control combined with the decoupled disturbance observer at 400 rpm are presented. The measurement is carried out, considering the standard current reference.

Despite the fast dynamic and good tracking of the controller, the oscillations caused by mutual inductances in the phase currents are still present. The performance of the observer is related to the disturbance variation. For a good disturbance observer performance, the disturbances should not vary too much between two consecutive sampling instances. However, in this case, the disturbance variation is very quickly, which damages the observer performance. The use of an optimized current reference is an alternative to overcoming this problem. Figure 5.18 shows the results for the decoupled disturbance observer with the use of the optimized current reference. Figure 5.18 (a) shows the measured currents in phases A, B and C; Figure 5.18 (b) presents the measured current versus the optimized current reference for phase A and Figure 5.18 (c) depicts the tracking error for the phase current in phase A. Also, Figure 5.18 (d) shows the output of the current controller combined with the disturbance observer and Figure 5.18 (e) the resultant electrical torque. Furthermore, Figure 5.18 (f) shows the observed disturbance in phase A.

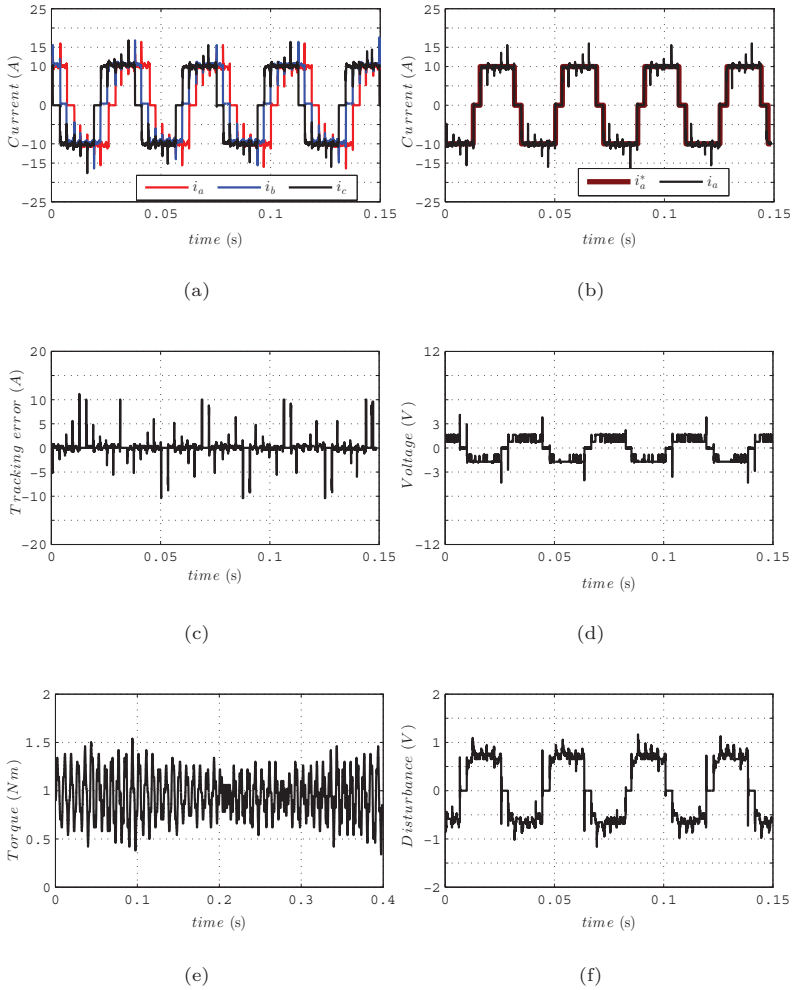


Figure 5.17.: Measurements with discrete time sliding mode controller combined with decoupled disturbance observer at 400 rpm/1Nm, with standard current reference. (a) Measured current for phase A, B and C; (b) current reference (i_a^*) versus measured current (i_a) for phase A; (c) tracking error for phase A; (d) output of the phase A current controller in combination with the disturbance observer; (e) electrical torque; (f) observed disturbance.

5. Experimental Results

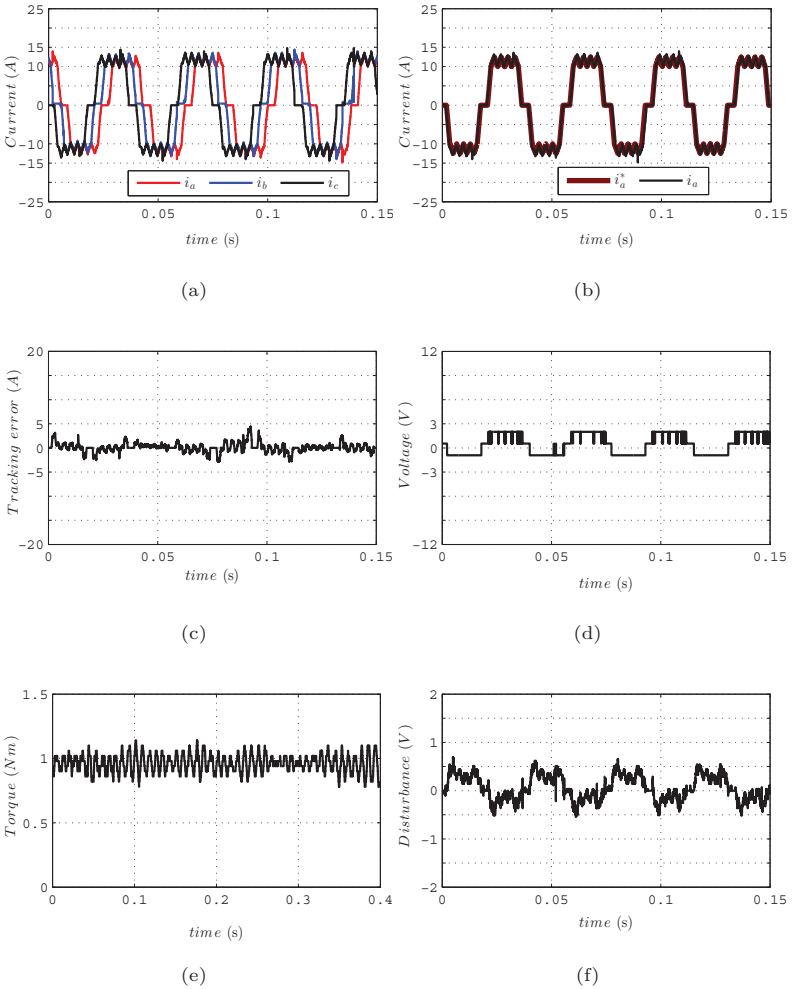


Figure 5.18.: Measurements with discrete time sliding mode controller combined with decoupled disturbance observer at 400 rpm/1 Nm, with optimized current reference. (a) Measured current for phase A, B and C; (b) current reference (i_a^*) versus measured current (i_a) for phase A; (c) tracking error for phase A; (d) output of the phase A current controller in combination with the disturbance observer; (e) electrical torque; (f) observed disturbance.

In Figure 5.18 (f), it is possible to verify the observed disturbance. The amplitude of the observed disturbance is not large, since part of the back-emf amplitude is calculated and compensated by the relationship between the measured speed and the constant back-emf (K_{pre}). Part of the back-emf amplitude that is not compensated by this relationship is observed by the disturbance estimator. Also, the non-idealities in the back-emf crest and the coupling inductance between the phases are observed and they are compensated by a feedforward action.

Figure 5.19 shows the results at nominal speed.

With the speed increasing, the challenge of the observer is even greater since the frequency of the disturbances variation increases. Even if the performance of the observer at high speeds is slightly inferior than the performance at low speeds, the response is even satisfactory and presents a good reference tracking with low electrical torque oscillations.

5. Experimental Results

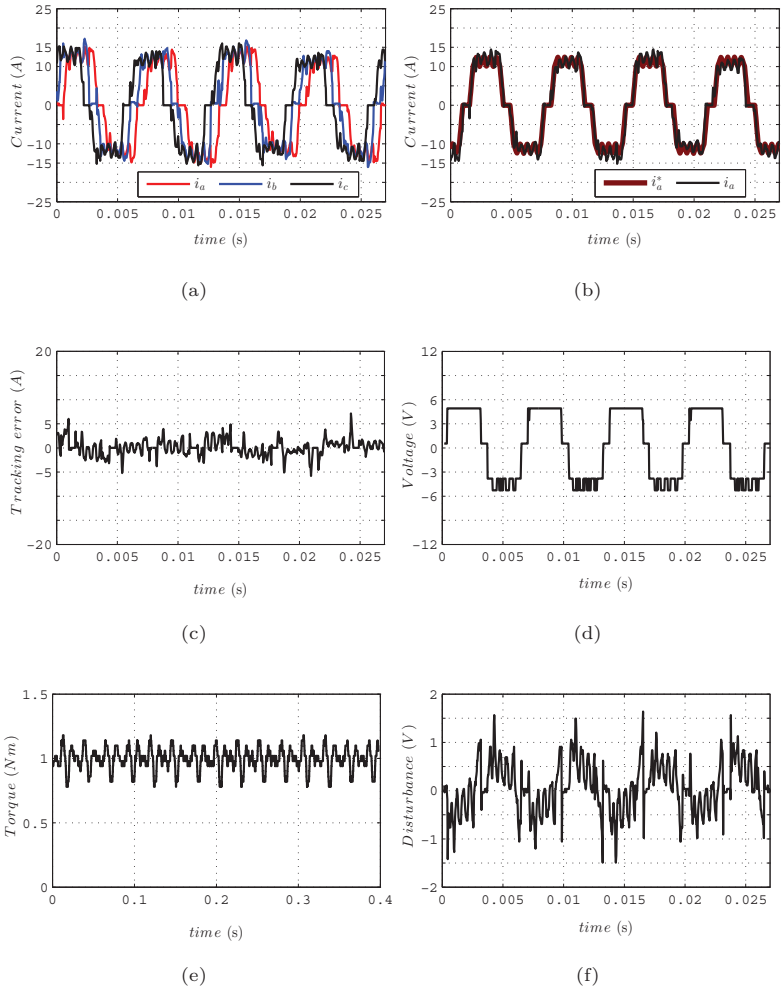


Figure 5.19.: Measurements with discrete time sliding mode controller combined with decoupled disturbance observer at 2250 rpm/1 Nm, with optimized current reference. (a) Measured current for phase A, B and C; (b) current reference (i_a^*) versus measured current (i_a) for phase A; (c) tracking error for phase A; (d) output of the phase A current controller in combination with the disturbance observer; (e) electrical torque; (f) observed disturbance.

5.6. Discrete time sliding mode controller based on Gao's approach with reduced order disturbance observer

The results of the combination of the discrete time sliding mode controller, with a reduced order disturbance observer applied to the six-phase BLDC machine, are presented in this section. For the sake of comparison, the results using the standard current reference at low speeds are shown in Figure 5.20.

Figure 5.21 shows the results with the optimized current reference.

Fast dynamic response and good reference tracking are achieved with the sliding mode controller combined with this observer at low speeds. In the observed disturbance in Figure 5.21 (f) is possible to notice that the observed signals are similar to a trapezoidal waveform. It concludes that much of the observed disturbance is related to back-emf.

Figure 5.22 shows the results at nominal speed. Figure 5.22 (a) shows the measured currents in phases A, B and C; Figure 5.22 (b) shows the measured current versus the optimized current reference for phase A and Figure 5.22 (c) presents the tracking error for the phase current in phase A. Figure 5.22 (d) shows the output of the current controller combined with the observer and Figure 5.22 (e) the resultant electrical torque. Figure 5.22 (f) shows the observed disturbance in phase A.

Despite the fact that at high speeds the frequency of the disturbance variation increases, which, in turn, deteriorate the estimator performance, the controller combined with the reduced order disturbance observer presents a satisfactory response since the resultant electrical torque does not present high oscillations and the current controller adequately tracks the reference.

5. Experimental Results

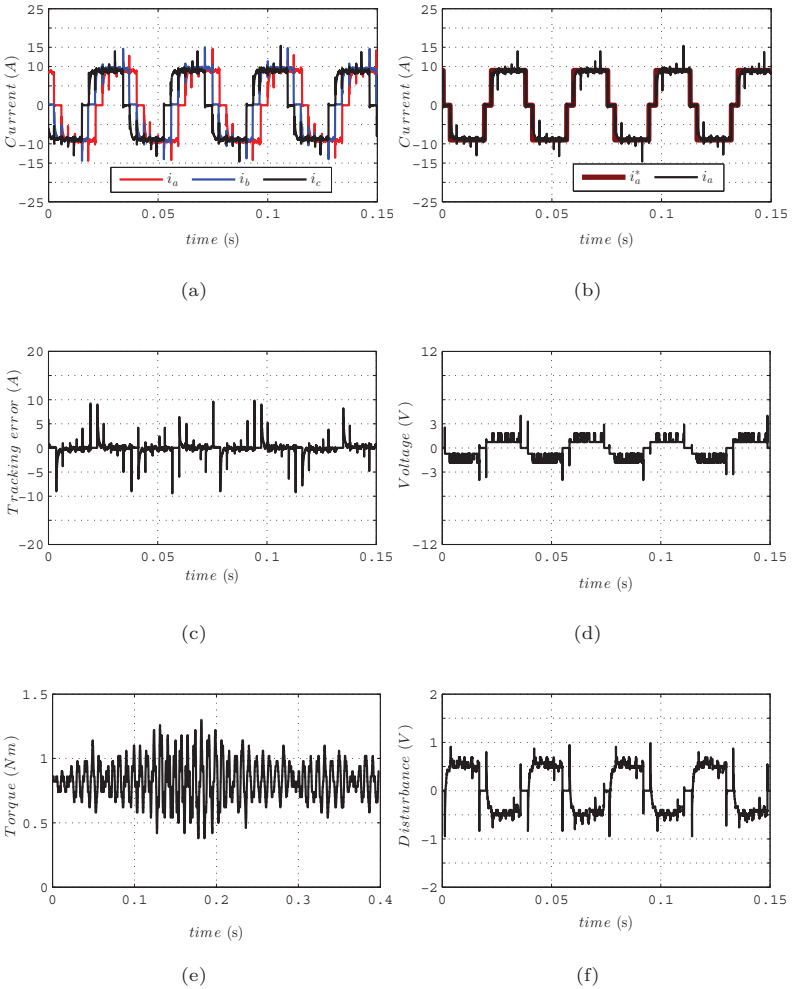


Figure 5.20.: Measurements with discrete time sliding mode controller combined with reduced order disturbance observer at 400 rpm/1 Nm, with standard current reference. (a) Measured current for phase A, B and C; (b) current reference (i_a^*) versus measured current (i_a) for phase A; (c) tracking error for phase A; (d) output of the phase A current controller in combination with the disturbance observer; (e) electrical torque; (f) observed disturbance.

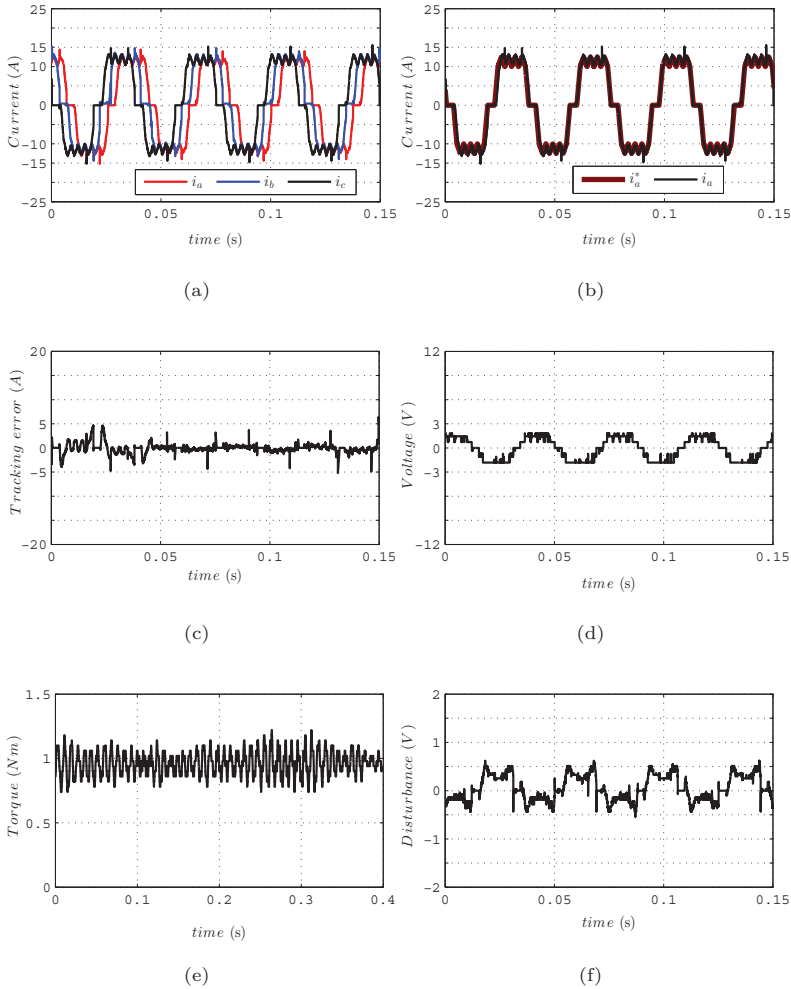


Figure 5.21.: Measurements with discrete time sliding mode controller combined with reduced order disturbance observer at 400 rpm/1 Nm, with optimized current reference. (a) Measured current for phase A, B and C; (b) current reference (i_a^*) versus measured current (i_a) for phase A; (c) tracking error for phase A; (d) output of the phase A current controller in combination with the disturbance observer; (e) electrical torque; (f) observed disturbance.

5. Experimental Results

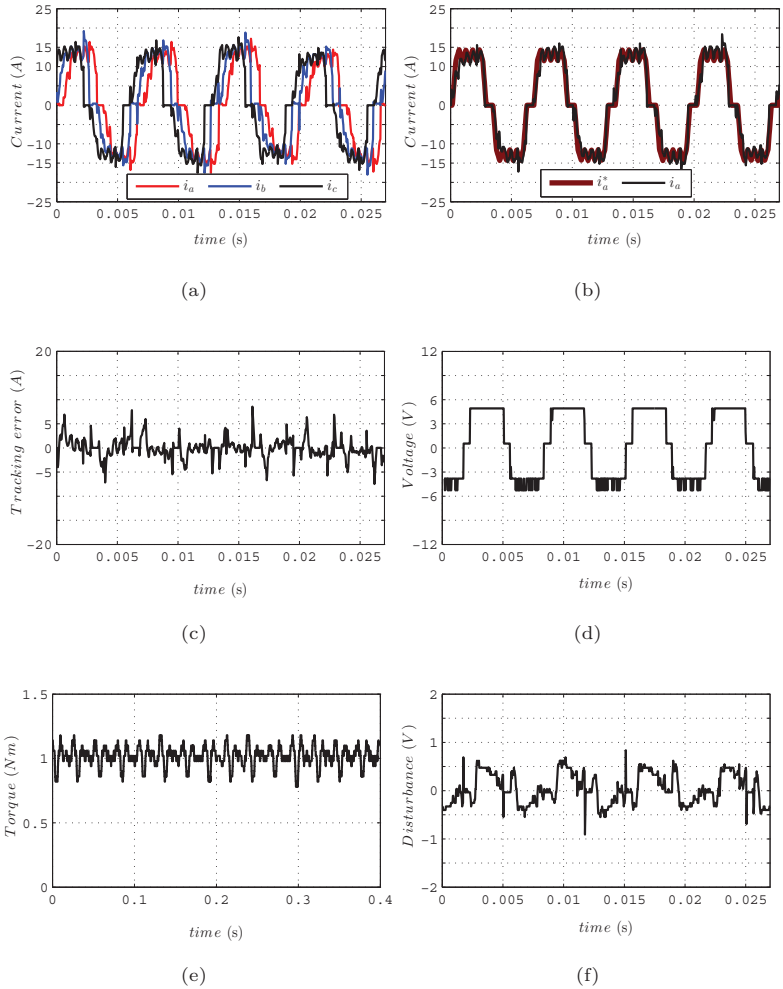


Figure 5.22.: Measurements with discrete time sliding mode controller combined with reduced order disturbance observer at 2250 rpm/1 Nm, with optimized current reference. (a) Measured current for phase A, B and C; (b) current reference (i_a^*) versus measured current (i_a) for phase A; (c) tracking error for phase A; (d) output of the phase A current controller in combination with the disturbance observer; (e) electrical torque; (f) observed disturbance.

5.7. Torque load variation and proportional-integral speed control

In order to verify the dynamic response of the proposed current controller, a load torque variation is applied to the system, as shown in Figure 5.23 (c). The measurement was carried out considering the discrete time sliding mode current controller combined with the reduced order disturbance observer.

In Figure 5.23 (a) the phase currents for phases A, B, C are shown. By the figure it is possible to verify a fast dynamic response without overshooting in the current, when a load torque variation is applied to the system.

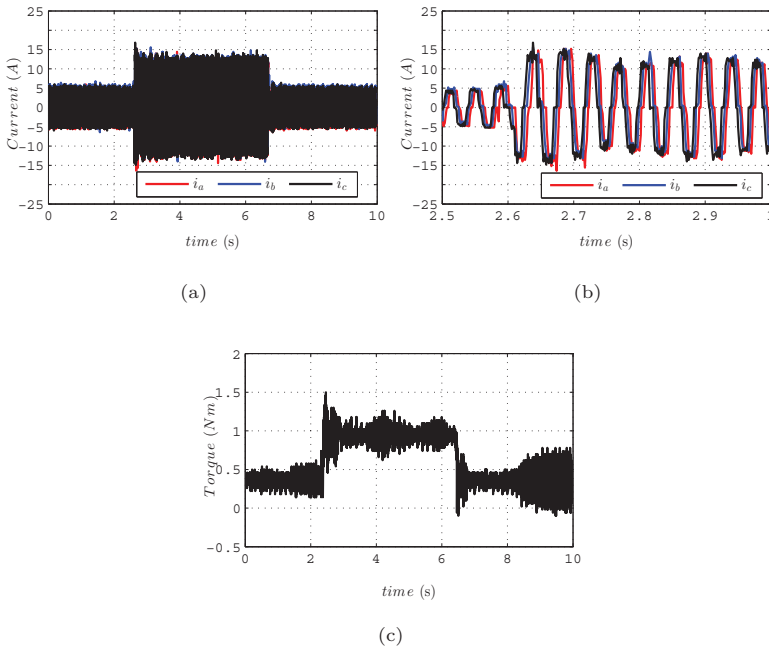


Figure 5.23.: (a) Measured current for phase A, B and C; (b) zoom of measured currents; (c) electrical torque.

5. Experimental Results

Figure 5.24 (a) e (b) show the performance of the proportional-integral speed controller used in the external loop of the BLDC control. From 0s to 8s, the system is in open loop. When the measured angular speed reaches the speed reference, the system goes to the closed loop. To verify the dynamic response of the speed controller, variations in the speed reference are carried out.

The PI speed controller presents a good dynamic response, when a speed variation is applied to the system. The proportional-integral controller is adequate to control the speed, since the mechanical model of the system does not present strong uncertainties and its dynamic is slower as the electrical dynamics.

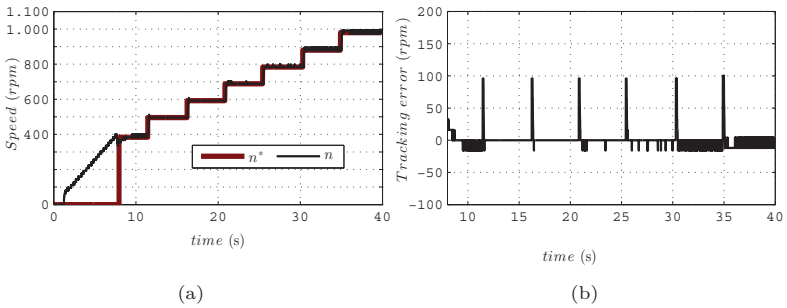


Figure 5.24.: (a) Speed reference versus measured speed in rpm; (b) speed tracking error in closed loop.

To summarize the performance of the proposed current controllers presented in this chapter, the maximal and the minimal values of the torque and the torque oscillations for each test case are presented in Table 5.1. The test cases are described below:

- **Test case 1:** PI current controller with optimized current reference at 400 rpm/1 Nm;
- **Test case 2:** PI current controller with optimized current reference at 2250 rpm/1 Nm;

- **Test case 3:** PI current controller with optimized current reference at 2250 rpm/1 Nm with gain parameter adjustment;
- **Test case 4:** discrete time sliding mode controller based on Gao's approach with standard current reference at 400 rpm/0.75 Nm;
- **Test case 5:** discrete time sliding mode controller based on Gao's approach with optimized current reference at 400 rpm/0.85 Nm;
- **Test case 6:** discrete time sliding mode controller based on Gao's approach with optimized current reference at 2250 rpm/1 Nm;
- **Test case 7:** discrete time super-twisting algorithm with optimized current reference at 400 rpm/1 Nm;
- **Test case 8:** discrete time super-twisting algorithm with optimized current reference at 2250 rpm/1 Nm;
- **Test case 9:** discrete time sliding mode controller based on Gao's approach with decoupled disturbance observer, with standard current reference at 400 rpm/1 Nm;
- **Test case 10:** discrete time sliding mode controller based on Gao's approach with decoupled disturbance observer with optimized current reference at 400 rpm/1 Nm;
- **Test case 11:** discrete time sliding mode controller based on Gao's approach with decoupled disturbance observer and optimized current reference at 2250 rpm/1 Nm;
- **Test case 12:** discrete time sliding mode controller based on Gao's approach with reduced order disturbance observer with standard current reference at 400 rpm/1 Nm;
- **Test case 13:** discrete time sliding mode controller based on Gao's approach with reduced order disturbance observer and optimized current reference at 400 rpm/1 Nm;

5. Experimental Results

- **Test case 14:** discrete time sliding mode controller based on Gao's approach with reduced order disturbance observer and optimized reference current at 2250 rpm/1 Nm.

Test case	Figure	Maximal Torque (Nm)	Minimal Torque (Nm)	Torque variation (Nm)	Torque ripple (%)
Test case 1	5.9	1.26	0.7	0.56	28
Test case 2	5.10	1.18	0.82	0.36	18
Test case 3	5.11	1.18	0.82	0.36	18
Test case 4	5.12	1.14	0.34	0.8	40
Test case 5	5.13	1	0.74	0.26	13
Test case 6	5.14	1.14	0.86	0.28	14
Test case 7	5.15	1.26	0.7	0.56	26.5
Test case 8	5.16	1.22	0.78	0.44	22
Test case 9	5.17	1.54	0.34	1.2	60
Test case 10	5.18	1.14	0.78	0.36	18
Test case 11	5.19	1.18	0.78	0.4	20
Test case 12	5.20	1.3	0.38	0.92	46
Test case 13	5.21	1.22	0.74	0.48	24
Test case 14	5.22	1.18	0.78	0.4	20

Table 5.1.: Electrical torque oscillations of each proposed current controller.

It is clear that the optimized current reference contributes considerably to the torque oscillation reduction. By using the optimized current reference all the current controllers present a satisfactory torque oscillation level for applications like traction, for example. However, the classical proportional-integral controller is not adequate for this application due to its slow dynamic response. In order to obtain an acceptable dynamic response over the whole operation range, the PI controller gains must be carefully tuned and due to the fidelity prerequisites of the model, the robustness over the whole operation range is effectively reduced by using the conventional classical control with limited bandwidth.

5.8. Summary

The main purpose of this chapter was to demonstrate experimentally the performance of the discrete time controllers applied to the six-phase brushless DC machine, as well the performance of the system when the optimized current reference is used. The experimental results show that the use of the optimized current reference contributes in minimizing the effect of the magnetic coupling between the phases and consequently, it reduces the oscillation in the phase current and in the resultant torque. The discrete time sliding mode controllers combined with the disturbance observers present a good performance over the entire operation range of the machine, thereby ensuring a torque with minimal oscillations. Experimental results from the combination of super-twisting controller with the reduced order disturbance observer are not presented in this chapter because of the similarity to the results obtained with the controller based on Gao's approach combined with the reduced order disturbance observer.

6. Conclusions and future work

This work investigated the application of different current control strategies based on the discrete time sliding mode approach in a fault-tolerant BLDC system intended for high-performance applications such as electric vehicles and aircraft systems. Ideally, in a fault-tolerant system, each single-phase module should present minimal electrical, magnetic and thermal interactions with the other phases. The electrical isolation between the phases is achieved by supplying each phase with a full bridge. To avoid the mutual coupling between the phases, a machine design with concentrated windings around each tooth is recommended. Nevertheless, the machine considered in this work presents a wave winding configuration, which gives a frame-size machine reduction and also significantly increases the magnetic coupling between the phases and consequently the complexity of the model. Great effort must be invested to describe minutely the model, since the self- and mutual inductances vary in accordance with the rotor position and with the current amplitude. For this reason, a robust controller approach has been chosen to ensure a good performance, even if the machine model is not completely known.

In Chapter 2, some characteristics of the six-phase BLDC machine — such as the back-emf, the partial behavior of the inductances and the description of the model in abc coordinates — have been presented.

The uncertainties and parameter variations present in the six-phase BLDC model due to the mutual coupling are a challenge for the controller design.

The multiphase BLDC control system developed in this thesis comprises an outer speed control loop and six inner current control loops. In the outer speed loop a proportional-integral control has been adopted. The proportional-integral classical controller is suitable to control the speed

since the mechanical dynamic is slower than the electrical machine dynamics and the mechanical model must reject just the disturbances caused by load torque variations.

The inner loops have a faster dynamic and great complexity due to the mutual magnetic coupling between the phases and non-idealities of the back-emf that cannot be measured. The purpose of this work was to develop a high-performance controller based on the sliding mode approach for the inner loops of the multiphase brushless DC machine, which would overcome the uncertainties and parameter variations in the model, thereby providing robustness to a system where the model is not exactly known.

The choice of the sliding mode approach was made in consideration of its robustness and high-simplicity controller design. The sliding mode is an appropriate tool for solving problems of uncertain nonlinear systems. Furthermore, the stability analysis in the continuous time domain is a natural result of the control design based on a Lyapunov function.

The development of the proposed method followed a structured and progressive sequence, to allow its understanding and implementation. First, a theoretical background of the continuous time sliding mode control was presented as a basis for the development of the sliding mode techniques in the discrete time domain. Considering that the experimental setup is based on an FPGA system, the experimental investigation of the continuous time sliding mode controller was not carried out. Usually, in the literature, the sliding mode controllers are designed in the continuous time domain and implemented in the discrete time domain. However, the conditions of existence of the sliding mode and the analysis of stability by Lyapunov in continuous and in discrete time domain differ from each other. For this reason, the design of the current controllers in the discrete time domain is carried out in order to ensure its stability in practical investigations.

Two discrete time sliding mode algorithms have been developed in this work: a first-order sliding mode based on Gao's approach and a second-order sliding mode controller based on a super-twisting algorithm. The sliding mode existence conditions and the control stability proof in the discrete time domain are presented for both algorithms.

Both algorithms are analyzed by simulation results presented in Chapter 3 and by experimental investigations presented in Chapter 5, and it has been concluded that only the proposed discrete time sliding mode controllers are not capable of overcoming the effects of the mutual inductances and the back-emf non-idealities in the system. As in discrete time the control law is updated just at sampling times, the invariance property of the sliding mode is lost and the control acts with limited robustness.

In order to improve the robustness of the control and to reduce the chattering, a combination of the discrete time sliding mode controller with a disturbance observer has been proposed in Chapter 4. The purpose of the observer is to estimate the disturbance in the system and to compensate this disturbance in the control law, reducing the uncertainties that the sliding mode controller has to overcome in order to keep its robustness. The formulation and analysis in discrete time domain of the two proposed observers, combined with the discrete time sliding mode controllers, are presented as well as simulation and experimental results.

A challenge for the disturbance observer is to deal with time-variant disturbances. The convergence of the estimation error depends on the disturbance observer error. Therefore, within one sampling period, the disturbance variation should not be too large owing to the fact that a fast time-varying disturbance encumbers the convergence of the error to zero, thereby diminishing the observer's performance.

From the simulation and experimental results of the disturbance observer, it has been concluded that the disturbance variations are not sufficiently small to ensure a good system performance. For this reason, an optimization in the current reference has been proposed in this work. The aim of the current reference optimization is to smooth the time derivative of the current signal in its rising and falling edges. By the simulations and experimental investigations carried out in this work, it can be concluded that the use of the optimized current contributes to a significant reduction in torque oscillations caused by the magnetic coupling between the phases.

In order to experimentally verify the performance of the proposed control techniques, an experimental setup based on FPGA implementation has been developed. The choice by an FPGA system has been made due

to the high numbers of PWM and IOs signals needed to feed the fault-tolerant six-phase brushless DC machine. Beyond that, considering the number of mathematical operations required to execute the control, the microprocessor should present a high computation capability.

The controller implementation with 50 kHz sampling frequency was desired in order to achieve a better performance of the discrete time controllers. With the code implementation in VHDL language in the FPGA, 50 kHz sampling frequency has been achieved.

The experimental results presented in Chapter 5 are qualitatively analyzed with regard to the controller dynamic response, tracking reference accuracy and torque oscillations. A comparative table has been presented with the resultant torque oscillations from each controller strategy developed in this work. It is possible to verify that the oscillations are considerably reduced when the optimized current reference is used, even for the proportional-integral current controller. However, it should be considered that the classical proportional-integral controller is not adequate for nonlinear systems applications due to its linear nature. Furthermore, due to the limited bandwidth, the conventional PI controller lacks robustness when facing an operation scenario where parameter variations and disturbances are added to the nominal model and consequently, the operation hardly remains satisfactory over the whole machine operation range. When compared with the sliding mode controllers, the PI controller presents a slow dynamic response which degrades the transient response of the BLDC machine by stating that it is not ideal for high-performance applications.

The discrete time controllers based on the sliding mode approach ensure a good dynamic response against parameter variations and a satisfactory performance over the entire BLDC operation range, even though the model is not exactly known. Furthermore, the control algorithm is simple to be implemented.

Future work that may stem from the development of this thesis includes an application of the proposed control, based on the discrete time sliding mode approach to a multiphase machine with higher electric power capacity, aiming its application in a traction system.

Another possibility for future work is the development of a sensorless strategy in order to eliminate the necessity of the hall sensors for the speed and rotor position measurement. Thus, it is possible to reduce the sizes of the motor.

It is also important the development and implementation of a remedial strategy in order to ensure a torque with minimal oscillations, even if one or more phases fail. When a failure occurs, the fault-tolerant system continues to operate but with a degraded performance. To improve the performance and ensure a torque with minimal oscillations — besides the fault-tolerant machine and driver design — a remedial control strategy should be adopted when a failure in the systems happens. A fault diagnostic algorithm should be carried out in order to know which phase has failed and from this information, a modification in the current reference from the phases that are in operation should be made to compensate the phases that are not in operation. It should be considered that if a sensorless strategy is indeed developed, it should also be adapted to the fault-tolerant remedial strategy.

Beyond that, thorough investigation of the energy efficiency analysis of the experimental setup is suggested, specifically an analysis of the converter performance such as converter switching losses — for example, by operating with the control strategies proposed in this work.

Bibliography

- [1] *Energy Technology Perspectives: Scenarios and Strategies to 2050*. 2008.
- [2] J. Rosero, J. Ortega, E. Aldabas, and L. Romeral, “Moving towards a more electric aircraft,” *Aerospace and Electronic Systems Magazine, IEEE*, vol. 22, pp. 3–9, March 2007.
- [3] M. Villani, M. Tursini, G. Fabri, and L. Castellini, “High reliability permanent magnet brushless motor drive for aircraft application,” *Industrial Electronics, IEEE Transactions on*, vol. 59, pp. 2073–2081, May 2012.
- [4] C. Chan, “The state of the art of electric, hybrid, and fuel cell vehicles,” *Proceedings of the IEEE*, vol. 95, pp. 704–718, April 2007.
- [5] C. Chan and Y. Wong, “Electric vehicles charge forward,” *Power and Energy Magazine, IEEE*, vol. 2, pp. 24–33, Nov 2004.
- [6] C. Chan, “An overview of electric vehicle technology,” *Proceedings of the IEEE*, vol. 81, pp. 1202–1213, Sep 1993.
- [7] T. Gopalarathnam, H. Toliyat, and J. Moreira, “Multi-phase fault-tolerant brushless DC motor drives,” in *Industry Applications Conference, 2000. Conference Record of the 2000 IEEE*, vol. 3, pp. 1683–1688 vol.3, 2000.
- [8] Y. Jin, Z. Tang, Y. Wen, and H. Zou, “High performance adaptive control for BLDC motor with realtime estimation of uncertainties,” in *Applied Power Electronics Conference and Exposition, 2006. APEC '06. Twenty-First Annual IEEE*, pp. 5 pp.–, March 2006.

- [9] G. Gatto, I. Marongiu, A. Perfetto, and A. Serpi, "Sensorless brushless DC drive controlled by predictive algorithm," in *Industrial Electronics, 2009. IECON '09. 35th Annual Conference of IEEE*, pp. 1270–1275, Nov 2009.
- [10] W. Gao and J. Hung, "Variable structure control of nonlinear systems: a new approach," *Industrial Electronics, IEEE Transactions on*, vol. 40, pp. 45–55, Feb 1993.
- [11] W. Perruquetti and J. P. Barbot, *Sliding Mode Control In Engineering*. CRC Press, 2002.
- [12] V. Utkin, "Variable structure systems with sliding modes," *Automatic Control, IEEE Transactions on*, vol. 22, pp. 212–222, April 1977.
- [13] G. Bartolini, A. Ferrara, and E. Usani, "Chattering avoidance by second-order sliding mode control," *Automatic Control, IEEE Transactions on*, vol. 43, pp. 241–246, Feb 1998.
- [14] K. Young and U. Ozguner, "Sliding mode: control engineering in practice," in *American Control Conference, 1999. Proceedings of the 1999*, vol. 1, pp. 150–162 vol.1, 1999.
- [15] W. Gao, Y. Wang, and A. Homaifa, "Discrete-time variable structure control systems," *Industrial Electronics, IEEE Transactions on*, vol. 42, pp. 117–122, April 1995.
- [16] B. Veselic, C. Milosavljevic, B. Perunicic-Drazenovic, and D. Mitic, "Digitally controlled sliding mode based servo-system with active disturbance estimator," in *Variable Structure Systems, 2006. VSS'06. International Workshop on*, pp. 51–56, June 2006.
- [17] T. Chunxia, "The control system design for ASV via discrete sliding mode control based on disturbance observer," in *Computational Engineering in Systems Applications, IMACS Multiconference on*, vol. 1, pp. 758–762, Oct 2006.

- [18] J. Liu and L. Han, "Discrete sliding mode control based on disturbance observer and its application on flight simulator servo system," in *Systems and Control in Aerospace and Astronautics, 2006. ISSCAA 2006. 1st International Symposium on*, pp. 4 pp.–928, Jan 2006.
- [19] X. Liu and X. Wei, "Composite disturbance-observer-based control and discrete-time sliding mode control for a class of MIMO systems with nonlinearity," in *Decision and Control, 2009 held jointly with the 2009 28th Chinese Control Conference. CDC/CCC 2009. Proceedings of the 48th IEEE Conference on*, pp. 2783–2788, Dec 2009.
- [20] J. Yang, S. Li, and X. Yu, "Sliding-mode control for systems with mismatched uncertainties via a disturbance observer," in *IECON 2011 - 37th Annual Conference on IEEE Industrial Electronics Society*, pp. 3988–3993, Nov 2011.
- [21] J.-L. Chang, "Discrete-time sliding mode controller design with state estimator and disturbance observer," *Electrical Engineering*, vol. 89, no. 5, pp. 397–404, 2007.
- [22] Z. W. S. S N Wu, X Y Sun and X. D. Wu, "Sliding-mode control for starting-mode spacecraft using a disturbance observer," *Proc. Inst. Mech. Eng. Part G: J. Aerospace Engineering*, vol. 224, no. 2, pp. 215–224, 2010.
- [23] M. Chen and W.-H. Chen, "Sliding mode control for a class of uncertain nonlinear system based on disturbance observer," *International Journal of Adaptive Control and Signal Processing*, vol. 24, no. 1, pp. 51–64, 2010.
- [24] P. Pillay and R. Krishnan, "Application characteristics of permanent magnet synchronous and brushless DC motors for servo drives," *Industry Applications, IEEE Transactions on*, vol. 27, pp. 986–996, Sep 1991.
- [25] P. Pillay and R. Krishnan, "Modeling, simulation, and analysis of permanent-magnet motor drives. I. The permanent-magnet syn-

- chronous motor drive,” *Industry Applications, IEEE Transactions on*, vol. 25, pp. 265–273, March 1989.
- [26] P. Pillay and R. Krishnan, “Modeling, simulation, and analysis of permanent-magnet motor drives. II. The brushless dc motor drive,” *Industry Applications, IEEE Transactions on*, vol. 25, pp. 274–279, March 1989.
- [27] P. Yedamale, “Brushless DC (BLDC) motor fundamentals - AN885,” tech. rep., Microchip Technology Inc, 2003.
- [28] C. L. Baratieri and H. Pinheiro, “A novel starting method for sensorless brushless DC motors with current limitation,” in *Electrical Machines (ICEM), 2012 XXth International Conference on*, pp. 816–822, Sept 2012.
- [29] J. Johnson, M. Ehsani, and Y. Guzelgunler, “Review of sensorless methods for brushless DC,” in *Industry Applications Conference, 1999. Thirty-Fourth IAS Annual Meeting. Conference Record of the 1999 IEEE*, vol. 1, pp. 143–150 vol.1, 1999.
- [30] T.-H. Kim, H.-W. Lee, and M. Ehsani, “State of the art and future trends in position sensorless brushless DC motor/generator drives,” in *Industrial Electronics Society, 2005. IECON 2005. 31st Annual Conference of IEEE*, pp. 8 pp.–, Nov 2005.
- [31] P. Acarnley and J. Watson, “Review of position-sensorless operation of brushless permanent-magnet machines,” *Industrial Electronics, IEEE Transactions on*, vol. 53, pp. 352–362, April 2006.
- [32] R. Krishnan, *Permanent Magnet Synchronous and Brushless DC Motor Drives*. 2009.
- [33] D. C. Hanselman, *Brushless Permanent Magnet Motor Design*. 1994.
- [34] S. Ziaeinejad, Y. Sangsefidi, and A. Shoulaie, “Analysis of commutation torque ripple of BLDC motors and a simple method for its

- reduction,” in *Electrical Engineering and Informatics (ICEEI), 2011 International Conference on*, pp. 1–6, July 2011.
- [35] L. Parsa, “On advantages of multi-phase machines,” in *Industrial Electronics Society, 2005. IECON 2005. 31st Annual Conference of IEEE*, pp. 6 pp.–, Nov 2005.
- [36] L. Parsa and H. Toliyat, “Fault-tolerant interior-permanent-magnet machines for hybrid electric vehicle applications,” *Vehicular Technology, IEEE Transactions on*, vol. 56, pp. 1546–1552, July 2007.
- [37] E. Levi, “Multiphase electric machines for variable-speed applications,” *Industrial Electronics, IEEE Transactions on*, vol. 55, pp. 1893–1909, May 2008.
- [38] G. Fabri, C. Olivieri, and M. Tursini, “Observer-based sensorless control of a five-phase brushless DC motor,” in *Electrical Machines (ICEM), 2010 XIX International Conference on*, pp. 1–6, Sept 2010.
- [39] T.-Y. Kim, B.-K. Lee, and C.-Y. Won, “Modeling and simulation of multiphase BLDC motor drive systems for autonomous underwater vehicles,” in *Electric Machines Drives Conference, 2007. IEMDC '07. IEEE International*, vol. 2, pp. 1366–1371, May 2007.
- [40] B. Mecrow, A. Jack, J. Haylock, and J. Coles, “Fault-tolerant permanent magnet machine drives,” *Electric Power Applications, IEE Proceedings -*, vol. 143, pp. 437–442, Nov 1996.
- [41] L. Parsa and H. Toliyat, “Five-phase permanent-magnet motor drives,” *Industry Applications, IEEE Transactions on*, vol. 41, pp. 30–37, Jan 2005.
- [42] A. Oliveira, J. Monteiro, M. Aguiar, and D. Gonzaga, “Extended DQ transformation for vectorial control applications of non-sinusoidal permanent magnet AC machines,” in *Power Electronics Specialists Conference, 2005. PESC '05. IEEE 36th*, pp. 1807–1812, June 2005.

- [43] D. Grenier and J.-P. Louis, "Use of an extension of the Park's transformation to determine control laws applied to a non-sinusoidal permanent magnet synchronous motor," in *Power Electronics and Applications, 1993., Fifth European Conference on*, pp. 32–37 vol.6, Sep 1993.
- [44] D. Grenier and J.-P. Louis, "Modeling for control of non-sinewave permanent-magnet synchronous drives by extending Park's transformation," *Mathematics and Computers in Simulation*, vol. 38, no. 4-6, pp. 445 – 452, 1995.
- [45] S. Mousavi, S. Mirbagheri, S. Sefid, and S. Sefid, "Simulation of a new multiphase BLDC motor drive," in *Power Electronics, Drives and Energy Systems (PEDES), 2012 IEEE International Conference on*, pp. 1–5, Dec 2012.
- [46] R. Krishnan, *Electric Motor Drives - Modeling, Analysis, And Control*. Prentice Hall, 2001.
- [47] L. Bai, "Electric drive system with BLDC motor," in *Electric Information and Control Engineering (ICEICE), 2011 International Conference on*, pp. 359–363, April 2011.
- [48] N. Milivojevic, M. Krishnamurthy, A. Emadi, and I. Stamenkovic, "Theory and implementation of a simple digital control strategy for brushless DC generators," *Power Electronics, IEEE Transactions on*, vol. 26, pp. 3345–3356, Nov 2011.
- [49] J. Jeon, S. Na, and H. Heo, "Cascade sliding mode; new robust PID control for BLDC motor of in-wheel system," in *Environment and Electrical Engineering (EEEIC), 2011 10th International Conference on*, pp. 1–4, May 2011.
- [50] Y. Xiaojuan and L. Jinglin, "A novel sliding mode control for BLDC motor network control system," in *Advanced Computer Theory and Engineering (ICACTE), 2010 3rd International Conference on*, vol. 2, pp. V2–289–V2–293, Aug 2010.

- [51] R. Decarlo, S. Zak, and G. Matthews, "Variable structure control of nonlinear multivariable systems: a tutorial," *Proceedings of the IEEE*, vol. 76, pp. 212–232, March 1988.
- [52] J. Hung, W. Gao, and J. Hung, "Variable structure control: a survey," *Industrial Electronics, IEEE Transactions on*, vol. 40, pp. 2–22, Feb 1993.
- [53] A. Isidori, *Nonlinear Control Systems*. Springer, 1995.
- [54] S. K. S. Christopher Edwards, *Sliding Mode Control: theory and applications*. CRC Press, 1998.
- [55] V. Utkin, *Sliding Modes in Control and Optimization*. Springer, 1992.
- [56] W. L. Jean Jacques Slotine, *Applied nonlinear control*. Prentice, 1991.
- [57] A. LEVANT, "Sliding order and sliding accuracy in sliding mode control," *International Journal of Control*, vol. 58, no. 6, pp. 1247–1263, 1993.
- [58] V. Utkin, "Equations of sliding mode in discontinuous systems," *Automation and Remote Control*, 1971.
- [59] A. GLUMINEAU, M. HAMY, C. LANIER, and C. H. MOOG, "Robust control of a brushless servo motor via sliding mode techniques," *International Journal of Control*, vol. 58, no. 5, pp. 979–990, 1993.
- [60] J.-J. E. Slotine, "Sliding controller design for non-linear systems," *International Journal of Control*, vol. 40, no. 2, pp. 421–434, 1984.
- [61] S. Laghrouche, F. Plestan, A. Glumineau, and R. Boisliveau, "Robust second order sliding mode control for a permanent magnet synchronous motor," in *American Control Conference, 2003. Proceedings of the 2003*, vol. 5, pp. 4071–4076 vol.5, June 2003.
- [62] A. Levant, "Principles of 2-sliding mode design," *Automatica*, vol. 43, no. 4, pp. 576 – 586, 2007.

- [63] C. Milosavljevic, "General conditions for the existence of a quasi sliding mode on the switching hyperplane in discrete time variable structure systems," *Automatic Remote Control*, vol. 46, pp. 307–314, 1985.
- [64] K. Furuta, "Sliding mode control of a discrete system," *Systems & Control Letters*, vol. 14, no. 2, pp. 145 – 152, 1990.
- [65] H. SIRA-RAMIREZ, "Non-linear discrete variable structure systems in quasi-sliding mode," *International Journal of Control*, vol. 54, no. 5, pp. 1171–1187, 1991.
- [66] S. Sarpturk, Y. Istefanopulos, and O. Kaynak, "On the stability of discrete-time sliding mode control systems," *Automatic Control, IEEE Transactions on*, vol. 32, pp. 930–932, Oct 1987.
- [67] A. Bartoszewicz, "Discrete-time quasi-sliding-mode control strategies," *Industrial Electronics, IEEE Transactions on*, vol. 45, pp. 633–637, Aug 1998.
- [68] G. Monsees, *Discrete-time sliding mode control*. PhD thesis, Technical University Delft, 2002.
- [69] Y. Niu, D. Ho, and Z. Wang, "Improved sliding mode control for discrete-time systems via reaching law," *Control Theory Applications, IET*, vol. 4, pp. 2245–2251, November 2010.
- [70] A. Bartoszewicz, "Remarks on "Discrete-time variable structure control systems"," *IEEE Transactions on Industrial Electronics*, vol. 43, no. 1, 1996.
- [71] A. Levant, "Higher-order sliding modes, differentiation and output-feedback control," *International Journal of Control*, vol. 76, no. 9-10, pp. 924–941, 2003.
- [72] M. Lopez-Franco, A. Salome-Baylon, A. Y. Alanis, and N. Arana-Daniel, "Discrete super twisting control algorithm for the nonholonomic mobile robots tracking problem," in *Electrical Engineering*

- Computing Science and Automatic Control (CCE), 2011 8th International Conference on*, pp. 1–5, Oct 2011.
- [73] I. Salgado, I. Chairez, B. Bandyopadhyay, L. Fridman, and O. Camacho, “Discrete-time non-linear state observer based on a super twisting-like algorithm,” *Control Theory Applications, IET*, vol. 8, pp. 803–812, July 2014.
- [74] A. Levant, “Discretization issues of high-order sliding modes,” *IFAC world Congress*, 2011.
- [75] Y. Eun, J.-H. Kim, K. Kim, and D.-I. Cho, “Discrete-time variable structure controller with a decoupled disturbance compensator and its application to a CNC servomechanism,” *Control Systems Technology, IEEE Transactions on*, vol. 7, pp. 414–423, July 1999.
- [76] K. soo Kim and K.-H. Rew, “Discrete-time disturbance observers with multirate output state estimation,” in *Control, Automation and Systems (ICCAS), 2011 11th International Conference on*, pp. 103–106, Oct 2011.
- [77] K. soo Kim, K.-H. Rew, and S. Kim, “Disturbance observer for estimating higher order disturbances in time series expansion,” *Automatic Control, IEEE Transactions on*, vol. 55, pp. 1905–1911, Aug 2010.
- [78] J.-L. Chang, “Applying discrete-time proportional integral observers for state and disturbance estimations,” *Automatic Control, IEEE Transactions on*, vol. 51, May 2006.
- [79] B.-G. Schulze, “Generator Elektromotor Kombination, insbesondere ein elektrisches Getriebe,” 2007.
- [80] B.-G. Schulze, M. Sven, S. Raav, and A. Dittner, “Einrichtung zum Schalten von Strömen in einer Statorwicklung einer Generator Elektromotor Kombination,” 1998.
- [81] B.-G. Schulze and A. Dittner, “Generator Motor Kombination [EN] Combined electric generator and motor for vehicle hybrid drive,” 1994.

- [82] A. S. Poznyak, *Advanced Mathematical Tools for Automatic Control Engineers: Deterministic Techniques*. 2008.

List of Figures

- 2.1. Back-emf and phase current in the PMSM and in the BLDC machine. 11
- 2.2. Typical BLDC driver topology. 12
- 2.3. Hall sensor, back-emf and phase currents in the BLDC machine. 12
- 2.4. Cross section of six-phase BLDC. 16
- 2.5. Wave winding. 17
- 2.6. One phase configuration of BLDC motor drive system. . . 17
- 2.7. Back-emf, Hall sensor signals and phase current waveforms in accordance with the electrical angle. 19
- 2.8. Single phase bridge considering the mutual coupling in the model. 21
- 2.9. (a) Self- and mutual inductances from phase A as a function of the rotor position, (b) self- and mutual inductances from phase B as a function of the rotor position, (c) self- and mutual inductances from phase C as a function of the rotor position, (d) self- and mutual inductances from phase D as a function of the rotor position. (e) self- and mutual inductances from phase E as a function of the rotor position. (f) self- and mutual inductances from phase F as a function of the rotor position. 27
- 2.10. Speed versus back-emf measurement for the back-emf factor determination. 28
- 2.11. Experimental back-emf from phase A, B and C of the six-phase BLDC motor at 2250 rpm. 29
- 3.1. Block diagram of the BLDC machine. 33

3.2.	Block diagram of PI current control with feedforward control for one phase of the multiphase BLDC machine.	34
3.3.	Illustration of the sliding surface behavior.	37
3.4.	Illustration of the chattering sliding surface behavior.	37
3.5.	Boundary layer.	43
3.6.	Sign function.	43
3.7.	Chattering reduction: saturation function.	44
3.8.	Chattering reduction: dead zone function.	45
3.9.	Super-twisting trajectory in the phase plane.	58
3.10.	Discrete time proportional-integral control. (a) Current reference (i_a^*) versus measured current (i_a) for phase A; (b) tracking error for phase A; (c) output of phase A current controller; (d) electrical torque; (e) zoom of electrical torque.	65
3.11.	Continuous time sliding mode control. (a) Current reference (i_a^*) versus measured current (i_a) for phase A; (b) tracking error for phase A; (c) output of phase A current controller; (d) electrical torque; (e) zoom of electrical torque.	67
3.12.	Discrete time sliding mode control. (a) Current reference (i_a^*) versus measured current (i_a) for phase A; (b) tracking error for phase A; (c) output of phase A current controller; (d) electrical torque; (e) zoom of electrical torque.	69
3.13.	Discrete time super-twisting control. (a) Current reference (i_a^*) versus measured current (i_a) for phase A; (b) tracking error for phase A; (c) output of phase A current controller; (d) electrical torque; (e) zoom of electrical torque.	71
3.14.	(a) Speed reference versus measured speed; (b) speed tracking error; (c) speed controller output; (d) load torque.	72
4.1.	System structure with nonlinear disturbance observer.	76
4.2.	Optimized phase current reference versus standard phase current reference.	82
4.3.	Optimized phase currents references, phase back-emf and resultant electrical torque.	84

4.4. Discrete time sliding mode control with decoupled variable structure disturbance observer. (a) Current reference (i_a^*) versus measured current (i_a) for phase A; (b) tracking error for phase A; (c) output of the current controller in combination with the disturbance observer; (d) disturbance versus estimated disturbance; (e) electrical torque; (f) zoom of electrical torque.	86
4.5. Discrete time sliding mode control with reduced order disturbance observer. (a) Current reference (i_a^*) versus measured current (i_a) for phase A; (b) tracking error for phase A; (c) output of the current controller in combination with the disturbance observer; (d) disturbance versus estimated disturbance; (e) electrical torque; (f) zoom of electrical torque.	88
4.6. Discrete time super-twisting control with reduced order disturbance observer. (a) Current reference (i_a^*) versus measured current (i_a) for phase A; (b) tracking error for phase A; (c) output of the current controller in combination with the disturbance observer; (d) disturbance versus estimated disturbance; (e) electrical torque; (f) zoom of electrical torque.	90
4.7. Discrete time sliding mode control with decoupled variable structure disturbance observer and optimized current reference. (a) Current reference (i_a^*) versus measured current (i_a) for phase A; (b) tracking error for phase A; (c) output of the current controller in combination with the disturbance observer; (d) disturbance versus estimated disturbance; (e) electrical torque; (f) zoom of electrical torque.	92
4.8. Discrete time sliding mode control with reduced order disturbance observer and optimized current reference. (a) Current reference (i_a^*) versus measured current (i_a) for phase A; (b) tracking error for phase A; (c) output of the current controller in combination with the disturbance observer; (d) disturbance versus estimated disturbance; (e) electrical torque; (f) zoom of electrical torque.	93

4.9.	Discrete time super-twisting control with reduced order disturbance observer and optimized current reference. (a) Current reference (i_a^*) versus measured current (i_a) for phase A; (b) tracking error for phase A; (c) output of the current controller in combination with the disturbance observer; (d) disturbance versus estimated disturbance; (e) electrical torque; (f) zoom of electrical torque.	95
5.1.	Six-phase BLDC machine.	96
5.2.	Experimental setup for the investigation of control strategies applied to the six-phase BLDC machine.	97
5.3.	FPGA Board.	98
5.4.	Hall sensor period.	99
5.5.	Six-phase H-Bridge converter.	100
5.6.	Reset signal from phase A.	101
5.7.	State machine for the six-phase BLDC machine control.	101
5.8.	Unipolar four-quadrant PWM technique.	103
5.9.	Measurements with PI current controller and optimized current reference at 400 rpm/1Nm. (a) Measured current for phase A, B and C; (b) current reference (i_a^*) versus measured current (i_a) for phase A; (c) tracking error for phase A; (d) output of phase A current controller; (e) electrical torque.	106
5.10.	Measurements with PI current controller and optimized current reference at 2250 rpm/1Nm. (a) Measured current for phase A, B and C; (b) current reference (i_a^*) versus measured current (i_a) for phase A; (c) tracking error for phase A; (d) output of phase A current controller; (e) electrical torque.	107

5.11. Measurements with PI current controller and optimized current reference at 2250 rpm/1Nm with gain parameter adjustment. (a) Measured current for phase A, B and C; (b) current reference (i_a^*) versus measured current (i_a) for phase A; (c) tracking error for phase A; (d) output of phase A current controller; (e) electrical torque. 108

5.12. Measurements with discrete time sliding mode current controller at 400 rpm/0.75Nm, with standard current reference. (a) Measured current for phase A, B and C; (b) current reference (i_a^*) versus measured current (i_a) for phase A; (c) tracking error for phase A; (d) output of phase A current controller; (e) electrical torque. 110

5.13. Measurements with discrete time sliding mode current controller at 400 rpm/0.85 Nm, with optimized current reference. (a) Measured current for phase A, B and C; (b) current reference (i_a^*) versus measured current (i_a) for phase A; (c) tracking error for phase A; (d) output of phase A current controller; (e) electrical torque. 111

5.14. Measurements with discrete time sliding mode current controller at 2250 rpm/1 Nm, with optimized current reference. (a) measured current for phase A, B and C; (b) current reference (i_a^*) versus measured current (i_a) for phase A; (c) tracking error for phase A; (d) output of phase A current controller; (e) electrical torque. 113

5.15. Measurements with discrete super-twisting current controller at 400 rpm/1 Nm, with optimized current reference. (a) Measured current for phase A, B and C; (b) current reference (i_a^*) versus measured current (i_a) for phase A; (c) tracking error for phase A; (d) output of phase A current controller; (e) electrical torque. 114

5.16. Measurements with discrete super-twisting current controller at 2250 rpm/1 Nm, with optimized current reference. (a) Measured current for phase A, B and C; (b) current reference (i_a^*) versus measured current (i_a) for phase A; (c) tracking error for phase A; (d) output of phase A current controller; (e) electrical torque. 115

5.17. Measurements with discrete time sliding mode controller combined with decoupled disturbance observer at 400 rpm/1Nm, with standard current reference. (a) Measured current for phase A, B and C; (b) current reference (i_a^*) versus measured current (i_a) for phase A; (c) tracking error for phase A; (d)output of the phase A current controller in combination with the disturbance observer; (e) electrical torque; (f) observed disturbance. 117

5.18. Measurements with discrete time sliding mode controller combined with decoupled disturbance observer at 400 rpm/1 Nm, with optimized current reference. (a) Measured current for phase A, B and C; (b) current reference (i_a^*) versus measured current (i_a) for phase A; (c) tracking error for phase A; (d) output of the phase A current controller in combination with the disturbance observer; (e) electrical torque; (f) observed disturbance. 118

5.19. Measurements with discrete time sliding mode controller combined with decoupled disturbance observer at 2250 rpm/1 Nm, with optimized current reference. (a) Measured current for phase A, B and C; (b) current reference (i_a^*) versus measured current (i_a) for phase A; (c) tracking error for phase A; (d) output of the phase A current controller in combination with the disturbance observer; (e) electrical torque; (f) observed disturbance. 120

5.20. Measurements with discrete time sliding mode controller combined with reduced order disturbance observer at 400 rpm/1 Nm, with standard current reference. (a) Measured current for phase A, B and C; (b) current reference (i_a^*) versus measured current (i_a) for phase A; (c) tracking error for phase A; (d) output of the phase A current controller in combination with the disturbance observer; (e) electrical torque; (f) observed disturbance.	122
5.21. Measurements with discrete time sliding mode controller combined with reduced order disturbance observer at 400 rpm/1 Nm, with optimized current reference. (a) Measured current for phase A, B and C; (b) current reference (i_a^*) versus measured current (i_a) for phase A; (c) tracking error for phase A; (d) output of the phase A current controller in combination with the disturbance observer; (e) electrical torque; (f) observed disturbance.	123
5.22. Measurements with discrete time sliding mode controller combined with reduced order disturbance observer at 2250 rpm/1 Nm, with optimized current reference. (a) Measured current for phase A, B and C; (b) current reference (i_a^*) versus measured current (i_a) for phase A; (c) tracking error for phase A; (d) output of the phase A current controller in combination with the disturbance observer; (e) electrical torque; (f) observed disturbance.	124
5.23. (a) Measured current for phase A, B and C; (b) zoom of measured currents; (c) electrical torque.	125
5.24. (a) Speed reference versus measured speed in rpm; (b) speed tracking error in closed loop.	126
A.1. Block diagram for BLDC machine current control.	160
A.2. Block diagram for BLDC machine speed control.	163

List of Tables

2.1. Conducting phases in accordance with the operation sectors.	18
2.2. Measurement of back-emf.	28
3.1. Motor specification.	62
5.1. Electrical torque oscillations of each proposed current controller.	128

Acronyms

Back-emf	Back electromotive force
BLDC	Brushless DC motors
CO ₂	Carbon dioxide
DC	Direct current
DSMC	Discrete time sliding mode control
DSP	Digital Signal Processor
DSTC	Discrete time super-twisting control
EMAs	Electromechanical actuators
EV	Electrical vehicle
FPGA	Field-programmable gate array
HEV	Hybrid vehicle
HOSM	High order sliding mode control
ICE	Internal combustion engine
IGBT	Insulated Gate Bipolar Transistor
IM	Induction motor
IO	Digital input/Digital output
MOSFET	Metal oxide semiconductor field effect transistor
NdFeB	Neodym-Eisen-Bor
PI	Proportional-integral
PMSM	Permanent Magnet Synchronous motor
PWM	Pulse width modulation
RMS	Root mean square
SMC	Sliding mode control
SmCo	Samarium Cobalt
VHDL	Very high speed integrated circuit hardware description language
VSC	Variable structure control

Symbols

Symbol	Description	Unit
P_{out}	Output power	W
T_e	Electrical torque	Nm
P_{CPMSM}	Copper losses in permanent magnet synchronous machine	W
P_{CBLDC}	Copper losses in brushless DC machine	W
I_{PMSM}	Rms current in permanent magnet synchronous machine	A
I_{BLDC}	Rms current in brushless DC machine	A
$I_{peakPMSM}$	Stator peak current in permanent magnet synchronous machine	A
$I_{peakBLDC}$	Stator peak current in brushless DC machine	A
P	Number of pole pairs	–
J	Inertia	kgm^2
b	Viscous damping	Ns/m
L_s	Self-inductance	H
R_s	Stator resistance	Ω
K_T	Torque constant	Nm/A
K_e	Back-emf constant	Vs/rad
T_L	Load torque	Nm
v_k	Phase voltage	V
i_k	Phase current	A
i^*	Phase current reference	A
e_k	Phase back-emf	V

f_k	Phase back-emf function	–
V_{DC}	DC link voltage	V
M_{kl}	Mutual inductance	H
M_1	Mutual inductance	H
M_2	Mutual inductance	H
M_3	Mutual inductance	H
E	Back-emf amplitude	V
n_{rpm}	Speed	rpm
V	Lyapunov function	–
K	Sliding mode control gain	–
t_e	Electrical period	s
t_s	Sampling period	s
f_s	Sampling frequency	Hz
KP_{dv}	Proportional gain in discrete time domain for current control	–
KI_{dv}	Integral gain in discrete time domain for current control	–
$KP_{d\omega}$	Proportional gain in discrete time domain for speed control	–
$KI_{d\omega}$	Integral gain in discrete time domain for speed control	–
rd	Relative degree	–
c	Sliding surface gain	–
sat	Saturation function	–
$sign$	Sign function	–
q	Gao's approach control gain	–
S_1	Auxiliary variable for stability analysis	–
S_2	Auxiliary variable for stability analysis	–
S_3	Auxiliary variable for stability analysis	–
S_4	Auxiliary variable for stability analysis	–
S_5	Auxiliary variable for stability analysis	–
S_6	Auxiliary variable for stability analysis	–
S_7	Auxiliary variable for stability analysis	–

S_8	Auxiliary variable for stability analysis	–
R	Radius of B_r	–
B_r	Stability circle for super-twisting stability analysis	–
A	Term of the LMI function	–
P	Term of the LMI function	–
Q	Term of the LMI function	–
X	Term of Lambda inequality	–
Y	Term of Lambda inequality	–
I	Identity matrix	–
A	Matrix of continuous time state-space model	–
B	Matrix of continuous time state-space model	–
C	Matrix of continuous time state-space model	–
F	Matrix of continuous time state-space model	–
G	Matrix of discrete time state-space model	–
W	Matrix of discrete time state-space model	–
H	Matrix of discrete time state-space model	–
J	Matrix of a $2n$ super-twisting system	–
L	Matrix of a $2n$ super-twisting system	–
R	Resistance matrix	–
z	Variable of the reduced order disturbance observer	–
Z	Auxiliar variable for super-twisting stability analysis	–
x	State vector	–
x^*	State reference value vector	–
u	Input vector / control law	–
y	Output vector	–
y^*	Output reference value vector	–

$\tilde{\mathbf{y}}_f^*$	Filtered output reference value vector	–
\mathbf{e}	Back-emf vector	V
\mathbf{emf}	Feedforward action	V
\mathbf{xc}	Auxiliary variable for PI control	–
\mathbf{u}_{eq}	Equivalent control term	V
\mathbf{u}_n	Discontinuous control law component	V
\mathbf{u}_{st}	Super-twisting control law component	V
\mathbf{u}_1	Auxiliary variable for super-twisting control	V
\mathbf{u}_{smc}	Gao's approach control law	V
\mathbf{uDSTC}	Super-twisting control law	V
Γ	Inductance matrix	–
θ_r	Mechanical rotor position	°
θ_e	Electrical rotor position	°
ω_r	Mechanical rotor speed	rad/s
ω_e	Electrical rotor speed	rad/s
Φ	Inclination of the new reference current	–
σ	Sliding mode surface	–
$\boldsymbol{\sigma}$	Sliding mode surface vector	–
ξ	Disturbance vector in continuous time domain	V
ξ_d	Disturbance vector in discrete time domain	V
$\tilde{\xi}_d$	Vector of disturbance estimation error in discrete time domain	V
$\hat{\xi}_d$	Estimated disturbance vector in discrete time domain	V
Λ	Disturbance observer gain	–
ϑ	Boundary layer width	–
ε	Gao's approach control gain	–
λ_1	Super-twisting control gain	–
λ_2	Super-twisting control gain	–
$\bar{\delta}_1$	Auxiliary variable for super-twisting stability analysis	–

$\overline{\delta_2}$	Auxiliary variable for super-twisting stability analysis	–
Θ	Auxiliary variable for super-twisting stability analysis	–
η_d	Disturbance vector considering back-emf as disturbance	–
Π	Disturbance upper bound	–
ψ	Matrix of a $2n$ super-twisting system	–
ω_b	Control bandwidth	–
ω_n	Corner frequency	rad/s
ς	Auxiliary variable for super-twisting stability analysis	–
ρ	Damping ratio	–

Index

Symbol	Description
*	Reference value
n	System order
m	System order
i	i -th variable from a vector
j	j -th variable from a vector
k	Phase a, b, c, d, e, f
l	Phase a, b, c, d, e, f

Appendices

A. Gain design of proportional-integral controller

A.1. Proportional-integral current controller: gain design

A simplified model for the electric dynamic of the BLDC machine, without to account the mutual inductances in the model is considered aiming to design the current PI controller. The mutual inductances are considered as disturbances of the system. The technique adopted for the design of proportional-integral controllers is based on the bandwidth of the closed-loop system. The BLDC nominal electrical dynamic with proportional-integral current controller is shown in Figure A.1.

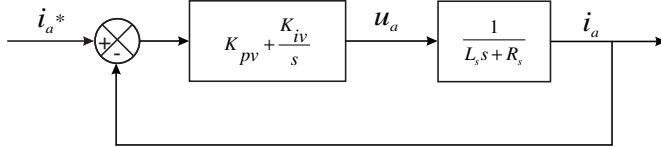


Figure A.1.: Block diagram for BLDC machine current control.

The transfer functions of the controller and of the electrical dynamic of each phase are given by:

$$G_{ic}(s) = K_{pv} + \frac{K_{iv}}{s} \quad (\text{A.1})$$

$$G_p(s) = \frac{1}{L_s s + R_s} \quad (\text{A.2})$$

The transfer function of the system in a closed-loop is represented by:

$$TF(s) = \frac{\frac{sK_{pv}+K_{iv}}{L_s}}{s^2 + \frac{R_s K_{pv}}{L_s} s + \frac{K_{iv}}{L_s}} \quad (\text{A.3})$$

The transfer function of the system in a closed-loop is represented by:

$$TF(s) = \frac{\frac{sK_{pv}+K_{iv}}{L_s}}{s^2 + \frac{R_s K_{pv}}{L_s} s + \frac{K_{iv}}{L_s}} \quad (\text{A.4})$$

Considering that the stator resistance is much lower than the controller gains, it can be neglected and the equation (A.4) is rewrite as:

$$TF(s) = \frac{\frac{sK_{pv}+K_{iv}}{L_s}}{s^2 + \frac{K_{pv}}{L_s} s + \frac{K_{iv}}{L_s}} \quad (\text{A.5})$$

This equation is identical to the equation of a second-order system in the frequency domain:

$$T_{ref}(s) = \frac{i(j\omega_b)}{i^*(j\omega_b)} = \frac{2\rho\omega_n(j\omega_b) + \omega_n^2}{(j\omega_b)^2 + 2\rho\omega_n(j\omega_b) + \omega_n^2} \quad (\text{A.6})$$

where ω_b is the bandwidth, ρ is the damping ratio, ω_n is corner frequency in rad/s.

Defining i_x as the output and i_x^* as reference, the bandwidth is given by:

$$20 \log \left(\frac{i_x(j\omega_b)}{i_x^*(j\omega_b)} \right) = 3.01db \quad (\text{A.7})$$

It is considered that the bandwidth is defined when the module is equal 0.707 pu, so:

$$\|T_{ref}(j\omega_b)\| = \left\| \frac{2\rho\omega_n(j\omega_b) + \omega_n^2}{(j\omega_b)^2 + 2\rho\omega_n(j\omega_b) + \omega_n^2} \right\| = 0.707 \quad (\text{A.8})$$

Solving the module of (A.8):

$$\|T_{ref}(j\omega_b)\| = \frac{\sqrt{(2\rho\omega_n\omega_b)^2 + \omega_n^4}}{\sqrt{(\omega_n^2 - \omega_b^2)^2 + (2\rho\omega_n\omega_b)^2}} = 0.707 \quad (\text{A.9})$$

From (A.9):

$$\omega_n^4 = 0.5 \left[(\omega_n^2 - \omega_b^2)^2 + (2\rho\omega_n\omega_b)^2 \right] - (2\rho\omega_n\omega_b)^2 \quad (\text{A.10})$$

Dividing the both equation sides by ω_n^4 :

$$1 = 0.5 \left\{ \left[1 - \left(\frac{\omega_b}{\omega_n} \right)^2 \right]^2 + 4\rho^2 \left(\frac{\omega_b}{\omega_n} \right)^2 \right\} - 4\rho^2 \left(\frac{\omega_b}{\omega_n} \right)^2 \quad (\text{A.11})$$

Defining:

$$a = \left(\frac{\omega_b}{\omega_n} \right)^2 \quad (\text{A.12})$$

and replacing in (A.11):

$$1 = 0.5 \left[(1 - a)^2 + 4\rho^2 a \right] - 4\rho^2 a \quad (\text{A.13})$$

Solving (A.13):

$$-0.5a^2 + (2\rho^2 + 1)a + 0.5 = 0 \quad (\text{A.14})$$

$$a = 2\rho^2 + 1 \pm \sqrt{(2\rho^2 + 1)^2 + 1} \quad (\text{A.15})$$

Replacing the equation (A.15) in (A.12):

$$\left(\frac{\omega_b}{\omega_n} \right)^2 = 2\rho^2 + 1 \pm \sqrt{(2\rho^2 + 1)^2 + 1} \quad (\text{A.16})$$

$$\omega_b = \omega_n \sqrt{2\rho^2 + 1 + \sqrt{(2\rho^2 + 1)^2 + 1}} \quad (\text{A.17})$$

From the transfer functions (A.5) and (A.6) it is possible to calculate the gains for the current controller:

$$2\rho\omega_n = \frac{K_{pv}}{L_s} \quad (\text{A.18})$$

$$\omega_n^2 = \frac{K_{iv}}{L_s} \quad (\text{A.19})$$

Replacing the equation (A.17) in (A.18) and in (A.19):

$$K_{pv} = \frac{2\rho\omega_b L_s}{\sqrt{2\rho^2 + 1} + \sqrt{(2\rho^2 + 1)^2 + 1}} \quad (\text{A.20})$$

$$K_{iv} = \frac{\omega_b^2 L_s}{2\rho^2 + 1 + \sqrt{(2\rho^2 + 1)^2 + 1}} \quad (\text{A.21})$$

The discrete gains are, calculated according to the Euler discretization:

$$K_{Pdv} = K_{pv} - \frac{K_{iv}t_s}{2} \quad (\text{A.22})$$

$$K_{Idv} = K_{iv}t_s \quad (\text{A.23})$$

A.2. Proportional-integral speed controller: gain design

The BLDC mechanical dynamic with proportional-integral speed controller is represented in the Figure A.2.

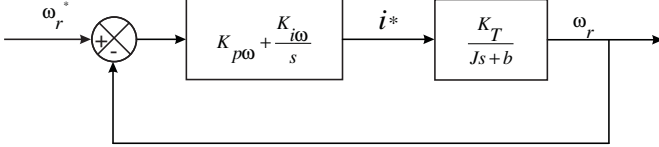


Figure A.2.: Block diagram for BLDC machine speed control.

The transfer function of the controller is given by:

$$G_{\omega c}(s) = K_{p\omega} + \frac{K_{i\omega}}{s} \quad (\text{A.24})$$

Considering the equation for the electromagnetic torque:

$$T_e = K_T (i_a + i_b + i_c + i_d + i_e + i_f) = K_T I \quad (\text{A.25})$$

The transfer function of the mechanical dynamic of the motor is represented the following equation:

$$G_{p\omega}(s) = \frac{K_T}{Js + b} \quad (\text{A.26})$$

Considering that $b \ll K_{p\omega}K_{i\omega}$, the parameter can be neglected and the closed-loop transfer function is given by:

$$T_{\omega F}(s) = \frac{\omega(s)}{\omega_{ref}(s)} = \frac{s \frac{K_{p\omega}K_T}{J} + \frac{K_{i\omega}K_T}{J}}{s^2 + \left(\frac{K_{p\omega}K_T}{J}\right)s + \frac{K_{i\omega}K_T}{J}} \quad (\text{A.27})$$

with (A.27) and the second-order system (A.6), it is possible to calculate the gains for the speed controller, similarly to the calculation of the gains for the current controller presented before.

$$2\rho\omega_n = \frac{K_{p\omega} \cdot K_T}{J} \quad (\text{A.28})$$

$$\omega_n^2 = \frac{K_{i\omega}}{J} \quad (\text{A.29})$$

Replacing the equation (A.17) in the equations (A.27) and (A.28) the proportional and the integral gain for the speed controller are respectively:

$$K_{p\omega} = \frac{J}{K_T} \frac{2\rho\omega_b}{\sqrt{2\rho^2 + 1 \pm \sqrt{(2\rho^2 + 1)^2 + 1}}} \quad (\text{A.30})$$

$$K_{i\omega} = \frac{J}{K_T} \frac{\omega_b^2}{2\rho^2 + 1 \pm \sqrt{(2\rho^2 + 1)^2 + 1}} \quad (\text{A.31})$$

The discrete gains are:

$$K_{Pd\omega} = K_{p\omega} - \frac{K_{i\omega}t_s}{2} \quad (\text{A.32})$$

$$K_{Id\omega} = K_{i\omega}t_s \quad (\text{A.33})$$

B. Mathematical development for control stability analysis

Appendix B presents the mathematical development carried out in order to solve the equations used to the stability analysis of the controllers presented in this thesis.

B.1. Stability proof of continuous time sliding mode controller

From (3.19):

$$\begin{aligned}
 \dot{V}(\sigma) = & -K \begin{bmatrix} \text{sign}(\sigma_a) \\ \text{sign}(\sigma_b) \\ \text{sign}(\sigma_c) \\ \text{sign}(\sigma_d) \\ \text{sign}(\sigma_e) \\ \text{sign}(\sigma_f) \end{bmatrix}^T \begin{bmatrix} \sigma_a \\ \sigma_b \\ \sigma_c \\ \sigma_d \\ \sigma_e \\ \sigma_f \end{bmatrix} + \begin{bmatrix} \xi_a \\ \xi_b \\ \xi_c \\ \xi_d \\ \xi_e \\ \xi_f \end{bmatrix}^T \begin{bmatrix} \sigma_a \\ \sigma_b \\ \sigma_c \\ \sigma_d \\ \sigma_e \\ \sigma_f \end{bmatrix} + \\
 & + \begin{bmatrix} \sigma_a \\ \sigma_b \\ \sigma_c \\ \sigma_d \\ \sigma_e \\ \sigma_f \end{bmatrix}^T \begin{bmatrix} \xi_a \\ \xi_b \\ \xi_c \\ \xi_d \\ \xi_e \\ \xi_f \end{bmatrix} - K \begin{bmatrix} \sigma_a \\ \sigma_b \\ \sigma_c \\ \sigma_d \\ \sigma_e \\ \sigma_f \end{bmatrix}^T \begin{bmatrix} \text{sign}(\sigma_a) \\ \text{sign}(\sigma_b) \\ \text{sign}(\sigma_c) \\ \text{sign}(\sigma_d) \\ \text{sign}(\sigma_e) \\ \text{sign}(\sigma_f) \end{bmatrix}
 \end{aligned} \tag{B.1}$$

$$\begin{aligned}
 \dot{V}(\sigma) = & -K \begin{pmatrix} \sigma_a \text{sign}(\sigma_a) + \sigma_b \text{sign}(\sigma_b) + \\ + \sigma_c \text{sign}(\sigma_c) + \sigma_d \text{sign}(\sigma_d) + \\ + \sigma_e \text{sign}(\sigma_e) + \sigma_f \text{sign}(\sigma_f) \end{pmatrix} + \\
 & + \xi_a \sigma_a + \xi_b \sigma_b + \xi_c \sigma_c + \xi_d \sigma_d + \xi_e \sigma_e + \xi_f \sigma_f + \\
 & + \xi_a \sigma_a + \xi_b \sigma_b + \xi_c \sigma_c + \xi_d \sigma_d + \xi_e \sigma_e + \xi_f \sigma_f - \\
 & -K \begin{pmatrix} \sigma_a \text{sign}(\sigma_a) + \sigma_b \text{sign}(\sigma_b) + \\ + \sigma_c \text{sign}(\sigma_c) + \sigma_d \text{sign}(\sigma_d) + \\ + \sigma_e \text{sign}(\sigma_e) + \sigma_f \text{sign}(\sigma_f) \end{pmatrix}
 \end{aligned} \tag{B.2}$$

B.2. Appendix B.2: Stability proof of discrete time sliding mode controller based on a Lyapunov function

From (3.60):

$$\begin{aligned}
 \Delta V(k) = & \sigma^T(k) \sigma(k) - qt_s \sigma^T(k) \sigma(k) - \varepsilon t_s \sigma^T(k) \text{sign}(\sigma(k)) - \\
 & - qt_s \sigma^T(k) \sigma(k) + q^2 t_s^2 \sigma^T(k) \sigma(k) + \varepsilon q t_s^2 \sigma^T(k) \text{sign}(\sigma(k)) - \\
 & - (\varepsilon t_s \text{sign}(\sigma(k)))^T \sigma(k) + qt_s (\varepsilon t_s \text{sign}(\sigma(k)))^T \sigma(k) + \\
 & + [(\varepsilon t_s \text{sign}(\sigma(k)))^T (\varepsilon t_s \text{sign}(\sigma(k)))] - (\sigma^T(k) \sigma(k))
 \end{aligned} \tag{B.3}$$

$$\begin{aligned}
 \Delta V(k) = & -2qt_s \sigma^T(k) \sigma(k) - \varepsilon t_s \sigma^T(k) \text{sign}(\sigma(k)) - \\
 & + q^2 t_s^2 \sigma^T(k) \sigma(k) + \varepsilon q t_s^2 \sigma^T(k) \text{sign}(\sigma(k)) - \\
 & - (\varepsilon t_s \text{sign}(\sigma(k)))^T \sigma(k) + qt_s (\varepsilon t_s \text{sign}(\sigma(k)))^T \sigma(k) + \varepsilon^2 t_s^2
 \end{aligned} \tag{B.4}$$

Solving (B.4):

$$\begin{aligned}
 \Delta V(k) = & -2qt_s \begin{bmatrix} \sigma_a(k) \\ \sigma_b(k) \\ \sigma_c(k) \\ \sigma_d(k) \\ \sigma_e(k) \\ \sigma_f(k) \end{bmatrix}^T \begin{bmatrix} \sigma_a(k) \\ \sigma_b(k) \\ \sigma_c(k) \\ \sigma_d(k) \\ \sigma_e(k) \\ \sigma_f(k) \end{bmatrix} - \\
 & -\varepsilon t_s \begin{bmatrix} \sigma_a(k) \\ \sigma_b(k) \\ \sigma_c(k) \\ \sigma_d(k) \\ \sigma_e(k) \\ \sigma_f(k) \end{bmatrix}^T \begin{bmatrix} \text{sign}(\sigma_a(k)) \\ \text{sign}(\sigma_b(k)) \\ \text{sign}(\sigma_c(k)) \\ \text{sign}(\sigma_d(k)) \\ \text{sign}(\sigma_e(k)) \\ \text{sign}(\sigma_f(k)) \end{bmatrix} + q^2 t_s^2 \begin{bmatrix} \sigma_a(k) \\ \sigma_b(k) \\ \sigma_c(k) \\ \sigma_d(k) \\ \sigma_e(k) \\ \sigma_f(k) \end{bmatrix}^T \begin{bmatrix} \sigma_a(k) \\ \sigma_b(k) \\ \sigma_c(k) \\ \sigma_d(k) \\ \sigma_e(k) \\ \sigma_f(k) \end{bmatrix} + \\
 & +\varepsilon q t_s^2 \begin{bmatrix} \sigma_a(k) \\ \sigma_b(k) \\ \sigma_c(k) \\ \sigma_d(k) \\ \sigma_e(k) \\ \sigma_f(k) \end{bmatrix}^T \begin{bmatrix} \text{sign}(\sigma_a(k)) \\ \text{sign}(\sigma_b(k)) \\ \text{sign}(\sigma_c(k)) \\ \text{sign}(\sigma_d(k)) \\ \text{sign}(\sigma_e(k)) \\ \text{sign}(\sigma_f(k)) \end{bmatrix} - \\
 & -\varepsilon t_s \begin{bmatrix} \text{sign}(\sigma_a(k)) \\ \text{sign}(\sigma_b(k)) \\ \text{sign}(\sigma_c(k)) \\ \text{sign}(\sigma_d(k)) \\ \text{sign}(\sigma_e(k)) \\ \text{sign}(\sigma_f(k)) \end{bmatrix}^T \begin{bmatrix} \sigma_a(k) \\ \sigma_b(k) \\ \sigma_c(k) \\ \sigma_d(k) \\ \sigma_e(k) \\ \sigma_f(k) \end{bmatrix} + \\
 & +q\varepsilon t_s^2 \begin{bmatrix} \text{sign}(\sigma_a(k)) \\ \text{sign}(\sigma_b(k)) \\ \text{sign}(\sigma_c(k)) \\ \text{sign}(\sigma_d(k)) \\ \text{sign}(\sigma_e(k)) \\ \text{sign}(\sigma_f(k)) \end{bmatrix}^T \begin{bmatrix} \sigma_a(k) \\ \sigma_b(k) \\ \sigma_c(k) \\ \sigma_d(k) \\ \sigma_e(k) \\ \sigma_f(k) \end{bmatrix} + \varepsilon^2 t_s^2
 \end{aligned}
 \tag{B.5}$$

The (B.5) can be rewritten as:

$$\begin{aligned} \Delta V(k) = & -2qt_s S_3(k) - \varepsilon t_s S_1(k) + q^2 t_s^2 S_3(k) + \\ & + \varepsilon q t_s^2 S_1(k) - \varepsilon t_s S_1(k) + q \varepsilon t_s^2 S_1(k) + \varepsilon^2 t_s^2 \end{aligned} \quad (\text{B.6})$$

B.3. Stability proof of discrete time sliding mode controller based on a Lyapunov function - Lower limit of ε

From (3.72):

$$\begin{aligned} & -qt_s \begin{bmatrix} \sigma_a(k) \\ \sigma_b(k) \\ \sigma_c(k) \\ \sigma_d(k) \\ \sigma_e(k) \\ \sigma_f(k) \end{bmatrix} \begin{bmatrix} \text{sign}(\sigma_a(k)) \\ \text{sign}(\sigma_b(k)) \\ \text{sign}(\sigma_c(k)) \\ \text{sign}(\sigma_d(k)) \\ \text{sign}(\sigma_e(k)) \\ \text{sign}(\sigma_f(k)) \end{bmatrix}^T - \\ & -\varepsilon t_s \begin{bmatrix} \text{sign}(\sigma_a(k)) \\ \text{sign}(\sigma_b(k)) \\ \text{sign}(\sigma_c(k)) \\ \text{sign}(\sigma_d(k)) \\ \text{sign}(\sigma_e(k)) \\ \text{sign}(\sigma_f(k)) \end{bmatrix} \begin{bmatrix} \text{sign}(\sigma_a(k)) \\ \text{sign}(\sigma_b(k)) \\ \text{sign}(\sigma_c(k)) \\ \text{sign}(\sigma_d(k)) \\ \text{sign}(\sigma_e(k)) \\ \text{sign}(\sigma_f(k)) \end{bmatrix}^T < 0 \end{aligned} \quad (\text{B.7})$$

$$\begin{aligned} & -qt_s \left(\begin{aligned} & \sigma_a(k) \text{sign}(\sigma_a(k)) + \sigma_b(k) \text{sign}(\sigma_b(k)) + \\ & + \sigma_c(k) \text{sign}(\sigma_c(k)) + \sigma_d(k) \text{sign}(\sigma_d(k)) + \\ & + \sigma_e(k) \text{sign}(\sigma_e(k)) + \sigma_f(k) \text{sign}(\sigma_f(k)) \end{aligned} \right) - \\ & -\varepsilon t_s \left(\begin{aligned} & \text{sign}^2(\sigma_a(k)) + \text{sign}^2(\sigma_b(k)) + \text{sign}^2(\sigma_c(k)) + \\ & + \text{sign}^2(\sigma_d(k)) + \text{sign}^2(\sigma_e(k)) + \text{sign}^2(\sigma_f(k)) \end{aligned} \right) < 0 \end{aligned} \quad (\text{B.8})$$

$$\begin{aligned} & -qt_s (|\sigma_a(k)| + |\sigma_b(k)| + |\sigma_c(k)| + |\sigma_d(k)| + |\sigma_e(k)| + |\sigma_f(k)|) - \varepsilon t_s < 0 \end{aligned} \quad (\text{B.9})$$

B.4. Stability proof of discrete time sliding mode controller based on a Lyapunov function - Upper limit of ε

From (3.75):

$$\begin{aligned}
 & 2 \begin{bmatrix} \sigma_a(k) \\ \sigma_b(k) \\ \sigma_c(k) \\ \sigma_d(k) \\ \sigma_e(k) \\ \sigma_f(k) \end{bmatrix} \begin{bmatrix} \text{sign}(\sigma_a(k)) \\ \text{sign}(\sigma_b(k)) \\ \text{sign}(\sigma_c(k)) \\ \text{sign}(\sigma_d(k)) \\ \text{sign}(\sigma_e(k)) \\ \text{sign}(\sigma_f(k)) \end{bmatrix}^T - qt_s \begin{bmatrix} \sigma_a(k) \\ \sigma_b(k) \\ \sigma_c(k) \\ \sigma_d(k) \\ \sigma_e(k) \\ \sigma_f(k) \end{bmatrix} \begin{bmatrix} \text{sign}(\sigma_a(k)) \\ \text{sign}(\sigma_b(k)) \\ \text{sign}(\sigma_c(k)) \\ \text{sign}(\sigma_d(k)) \\ \text{sign}(\sigma_e(k)) \\ \text{sign}(\sigma_f(k)) \end{bmatrix}^T - \\
 & -\varepsilon t_s \begin{bmatrix} \text{sign}(\sigma_a(k)) \\ \text{sign}(\sigma_b(k)) \\ \text{sign}(\sigma_c(k)) \\ \text{sign}(\sigma_d(k)) \\ \text{sign}(\sigma_e(k)) \\ \text{sign}(\sigma_f(k)) \end{bmatrix} \begin{bmatrix} \text{sign}(\sigma_a(k)) \\ \text{sign}(\sigma_b(k)) \\ \text{sign}(\sigma_c(k)) \\ \text{sign}(\sigma_d(k)) \\ \text{sign}(\sigma_e(k)) \\ \text{sign}(\sigma_f(k)) \end{bmatrix}^T \geq 0
 \end{aligned} \tag{B.10}$$

$$\begin{aligned}
 & 2 \left(\sigma_a(k)\text{sign}(\sigma_a(k)) + \sigma_b(k)\text{sign}(\sigma_b(k)) + \sigma_c(k)\text{sign}(\sigma_c(k)) + \right. \\
 & \left. + \sigma_d(k)\text{sign}(\sigma_d(k)) + \sigma_e(k)\text{sign}(\sigma_e(k)) + \sigma_f(k)\text{sign}(\sigma_f(k)) \right) \\
 & -qt_s \left(\sigma_a(k)\text{sign}(\sigma_a(k)) + \sigma_b(k)\text{sign}(\sigma_b(k)) + \sigma_c(k)\text{sign}(\sigma_c(k)) + \right. \\
 & \left. + \sigma_d(k)\text{sign}(\sigma_d(k)) + \sigma_e(k)\text{sign}(\sigma_e(k)) + \sigma_f(k)\text{sign}(\sigma_f(k)) \right) \\
 & -\varepsilon t_s \left(\text{sign}^2(\sigma_a(k)) + \text{sign}^2(\sigma_b(k)) + \text{sign}^2(\sigma_c(k)) + \right. \\
 & \left. + \text{sign}^2(\sigma_d(k)) + \text{sign}^2(\sigma_e(k)) + \text{sign}^2(\sigma_f(k)) \right) \geq 0
 \end{aligned} \tag{B.11}$$

$$\begin{aligned}
 & 2(|\sigma_a(k)| + |\sigma_b(k)| + |\sigma_c(k)| + |\sigma_d(k)| + |\sigma_e(k)| + |\sigma_f(k)|) \\
 & -qt_s(|\sigma_a(k)| + |\sigma_b(k)| + |\sigma_c(k)| + |\sigma_d(k)| + |\sigma_e(k)| + |\sigma_f(k)|) - \varepsilon t_s \geq 0
 \end{aligned} \tag{B.12}$$

B.5. Stability proof of discrete time Sliding Mode controller based on a Lyapunov function considering disturbances in the model

From (3.78):

$$\Delta V(k) = \left(\begin{array}{l} (\boldsymbol{\xi}_d(k))^T (\boldsymbol{\xi}_d(k) + \boldsymbol{\sigma}(k) - \boldsymbol{\sigma}(k)qt_s - \varepsilon t_s \text{sign}(\boldsymbol{\sigma}(k))) \\ + (\boldsymbol{\sigma}(k))^T (\boldsymbol{\xi}_d(k) + \boldsymbol{\sigma}(k) - \boldsymbol{\sigma}(k)qt_s - \varepsilon t_s \text{sign}(\boldsymbol{\sigma}(k))) \\ - (\boldsymbol{\sigma}(k)qt_s)^T (\boldsymbol{\xi}_d(k) + \boldsymbol{\sigma}(k) - \boldsymbol{\sigma}(k)qt_s - \varepsilon t_s \text{sign}(\boldsymbol{\sigma}(k))) \\ - (\varepsilon t_s \text{sign}(\boldsymbol{\sigma}(k)))^T (\boldsymbol{\xi}_d(k) + \boldsymbol{\sigma}(k) - \boldsymbol{\sigma}(k)qt_s - \varepsilon t_s \text{sign}(\boldsymbol{\sigma}(k))) \end{array} \right) - (\boldsymbol{\sigma}^T(k) \mathbf{P} \boldsymbol{\sigma}(k)) \quad (\text{B.13})$$

Solving (B.13):

$$\begin{aligned}
 \Delta V(k) = & \begin{bmatrix} \xi_{da}(k) \\ \xi_{db}(k) \\ \xi_{dc}(k) \\ \xi_{dd}(k) \\ \xi_{de}(k) \\ \xi_{df}(k) \end{bmatrix}^T \begin{bmatrix} \xi_{da}(k) \\ \xi_{db}(k) \\ \xi_{dc}(k) \\ \xi_{dd}(k) \\ \xi_{de}(k) \\ \xi_{df}(k) \end{bmatrix} + \begin{bmatrix} \xi_{da}(k) \\ \xi_{db}(k) \\ \xi_{dc}(k) \\ \xi_{dd}(k) \\ \xi_{de}(k) \\ \xi_{df}(k) \end{bmatrix}^T \begin{bmatrix} \sigma_a(k) \\ \sigma_b(k) \\ \sigma_c(k) \\ \sigma_d(k) \\ \sigma_e(k) \\ \sigma_f(k) \end{bmatrix} - \\
 & -qt_s \begin{bmatrix} \xi_{da}(k) \\ \xi_{db}(k) \\ \xi_{dc}(k) \\ \xi_{dd}(k) \\ \xi_{de}(k) \\ \xi_{df}(k) \end{bmatrix}^T \begin{bmatrix} \sigma_a(k) \\ \sigma_b(k) \\ \sigma_c(k) \\ \sigma_d(k) \\ \sigma_e(k) \\ \sigma_f(k) \end{bmatrix} - \varepsilon t_s \begin{bmatrix} \xi_{da}(k) \\ \xi_{db}(k) \\ \xi_{dc}(k) \\ \xi_{dd}(k) \\ \xi_{de}(k) \\ \xi_{df}(k) \end{bmatrix}^T \begin{bmatrix} \text{sign}(\sigma_a(k)) \\ \text{sign}(\sigma_b(k)) \\ \text{sign}(\sigma_c(k)) \\ \text{sign}(\sigma_d(k)) \\ \text{sign}(\sigma_e(k)) \\ \text{sign}(\sigma_f(k)) \end{bmatrix} + \\
 & + \begin{bmatrix} \sigma_a(k) \\ \sigma_b(k) \\ \sigma_c(k) \\ \sigma_d(k) \\ \sigma_e(k) \\ \sigma_f(k) \end{bmatrix}^T \begin{bmatrix} \xi_{da}(k) \\ \xi_{db}(k) \\ \xi_{dc}(k) \\ \xi_{dd}(k) \\ \xi_{de}(k) \\ \xi_{df}(k) \end{bmatrix} - qt_s \begin{bmatrix} \sigma_a(k) \\ \sigma_b(k) \\ \sigma_c(k) \\ \sigma_d(k) \\ \sigma_e(k) \\ \sigma_f(k) \end{bmatrix}^T \begin{bmatrix} \sigma_a(k) \\ \sigma_b(k) \\ \sigma_c(k) \\ \sigma_d(k) \\ \sigma_e(k) \\ \sigma_f(k) \end{bmatrix} - \\
 & -\varepsilon t_s \begin{bmatrix} \sigma_a(k) \\ \sigma_b(k) \\ \sigma_c(k) \\ \sigma_d(k) \\ \sigma_e(k) \\ \sigma_f(k) \end{bmatrix}^T \begin{bmatrix} \text{sign}(\sigma_a(k)) \\ \text{sign}(\sigma_b(k)) \\ \text{sign}(\sigma_c(k)) \\ \text{sign}(\sigma_d(k)) \\ \text{sign}(\sigma_e(k)) \\ \text{sign}(\sigma_f(k)) \end{bmatrix} - qt_s \begin{bmatrix} \sigma_a(k) \\ \sigma_b(k) \\ \sigma_c(k) \\ \sigma_d(k) \\ \sigma_e(k) \\ \sigma_f(k) \end{bmatrix}^T \begin{bmatrix} \xi_{da}(k) \\ \xi_{db}(k) \\ \xi_{dc}(k) \\ \xi_{dd}(k) \\ \xi_{de}(k) \\ \xi_{df}(k) \end{bmatrix} - \\
 & -qt_s \begin{bmatrix} \sigma_a(k) \\ \sigma_b(k) \\ \sigma_c(k) \\ \sigma_d(k) \\ \sigma_e(k) \\ \sigma_f(k) \end{bmatrix}^T \begin{bmatrix} \sigma_a(k) \\ \sigma_b(k) \\ \sigma_c(k) \\ \sigma_d(k) \\ \sigma_e(k) \\ \sigma_f(k) \end{bmatrix} + q^2 t_s^2 \begin{bmatrix} \sigma_a(k) \\ \sigma_b(k) \\ \sigma_c(k) \\ \sigma_d(k) \\ \sigma_e(k) \\ \sigma_f(k) \end{bmatrix}^T \begin{bmatrix} \sigma_a(k) \\ \sigma_b(k) \\ \sigma_c(k) \\ \sigma_d(k) \\ \sigma_e(k) \\ \sigma_f(k) \end{bmatrix} +
 \end{aligned}$$

$$\begin{aligned}
 & +q\varepsilon t_s^2 \begin{bmatrix} \sigma_a(k) \\ \sigma_b(k) \\ \sigma_c(k) \\ \sigma_d(k) \\ \sigma_e(k) \\ \sigma_f(k) \end{bmatrix}^T \begin{bmatrix} \text{sign}(\sigma_a(k)) \\ \text{sign}(\sigma_b(k)) \\ \text{sign}(\sigma_c(k)) \\ \text{sign}(\sigma_d(k)) \\ \text{sign}(\sigma_e(k)) \\ \text{sign}(\sigma_f(k)) \end{bmatrix} - \\
 & -\varepsilon t_s \begin{bmatrix} \text{sign}(\sigma_a(k)) \\ \text{sign}(\sigma_b(k)) \\ \text{sign}(\sigma_c(k)) \\ \text{sign}(\sigma_d(k)) \\ \text{sign}(\sigma_e(k)) \\ \text{sign}(\sigma_f(k)) \end{bmatrix}^T \begin{bmatrix} \xi_{da}(k) \\ \xi_{db}(k) \\ \xi_{dc}(k) \\ \xi_{dd}(k) \\ \xi_{de}(k) \\ \xi_{df}(k) \end{bmatrix} - \\
 & -\varepsilon t_s \begin{bmatrix} \text{sign}(\sigma_a(k)) \\ \text{sign}(\sigma_b(k)) \\ \text{sign}(\sigma_c(k)) \\ \text{sign}(\sigma_d(k)) \\ \text{sign}(\sigma_e(k)) \\ \text{sign}(\sigma_f(k)) \end{bmatrix}^T \begin{bmatrix} \sigma_a(k) \\ \sigma_b(k) \\ \sigma_c(k) \\ \sigma_d(k) \\ \sigma_e(k) \\ \sigma_f(k) \end{bmatrix} + \\
 & +q\varepsilon t_s^2 \begin{bmatrix} \text{sign}(\sigma_a(k)) \\ \text{sign}(\sigma_b(k)) \\ \text{sign}(\sigma_c(k)) \\ \text{sign}(\sigma_d(k)) \\ \text{sign}(\sigma_e(k)) \\ \text{sign}(\sigma_f(k)) \end{bmatrix}^T \begin{bmatrix} \sigma_a(k) \\ \sigma_b(k) \\ \sigma_c(k) \\ \sigma_d(k) \\ \sigma_e(k) \\ \sigma_f(k) \end{bmatrix} + \\
 & +\varepsilon^2 t_s^2 \begin{bmatrix} \text{sign}(\sigma_a(k)) \\ \text{sign}(\sigma_b(k)) \\ \text{sign}(\sigma_c(k)) \\ \text{sign}(\sigma_d(k)) \\ \text{sign}(\sigma_e(k)) \\ \text{sign}(\sigma_f(k)) \end{bmatrix}^T \begin{bmatrix} \text{sign}(\sigma_a(k)) \\ \text{sign}(\sigma_b(k)) \\ \text{sign}(\sigma_c(k)) \\ \text{sign}(\sigma_d(k)) \\ \text{sign}(\sigma_e(k)) \\ \text{sign}(\sigma_f(k)) \end{bmatrix}
 \end{aligned} \tag{B.14}$$

$$\begin{aligned}
 \Delta V(k) = & \xi_{da}^2(k) + \xi_{db}^2(k) + \xi_{dc}^2(k) + \xi_{dd}^2(k) + \xi_{de}^2(k) + \xi_{df}^2(k) + \\
 & + \xi_{da}(k)\sigma_a(k) + \xi_{db}(k)\sigma_b(k) + \xi_{dc}(k)\sigma_c(k) + \\
 & + \xi_{dd}(k)\sigma_d(k) + \xi_{de}(k)\sigma_e(k) + \xi_{df}(k)\sigma_f(k) - \\
 & -qt_s \left(\begin{array}{l} \xi_{da}(k)\sigma_a(k) + \xi_{db}(k)\sigma_b(k) + \xi_{dc}(k)\sigma_c(k) + \\ + \xi_{dd}(k)\sigma_d(k) + \xi_{de}(k)\sigma_e(k) + \xi_{df}(k)\sigma_f(k) \end{array} \right) - \\
 & -\varepsilon t_s \left(\begin{array}{l} \xi_{da}(k)\text{sign}(\sigma_a(k)) + \xi_{db}(k)\text{sign}(\sigma_b(k)) + \\ + \xi_{dc}(k)\text{sign}(\sigma_c(k)) + \xi_{dd}(k)\text{sign}(\sigma_d(k)) + \\ + \xi_{de}(k)\text{sign}(\sigma_e(k)) + \xi_{df}(k)\text{sign}(\sigma_f(k)) \end{array} \right) + \\
 & + \xi_{da}(k)\sigma_a(k) + \xi_{db}(k)\sigma_b(k) + \xi_{dc}(k)\sigma_c(k) + \\
 & + \xi_{dd}(k)\sigma_d(k) + \xi_{de}(k)\sigma_e(k) + \xi_{df}(k)\sigma_f(k) - \\
 & -qt_s (\sigma_a^2(k) + \sigma_b^2(k) + \sigma_c^2(k) + \sigma_d^2(k) + \sigma_e^2(k) + \sigma_f^2(k)) - \\
 & \varepsilon t_s \left(\begin{array}{l} \sigma_a(k)\text{sign}(\sigma_a(k)) + \sigma_b(k)\text{sign}(\sigma_b(k)) + \\ + \sigma_c(k)\text{sign}(\sigma_c(k)) + \sigma_d(k)\text{sign}(\sigma_d(k)) + \\ + \sigma_e(k)\text{sign}(\sigma_e(k)) + \sigma_f(k)\text{sign}(\sigma_f(k)) \end{array} \right) - \\
 & -qt_s \left(\begin{array}{l} \xi_{da}(k)\sigma_a(k) + \xi_{db}(k)\sigma_b(k) + \xi_{dc}(k)\sigma_c(k) + \\ + \xi_{dd}(k)\sigma_d(k) + \xi_{de}(k)\sigma_e(k) + \xi_{df}(k)\sigma_f(k) \end{array} \right) \\
 & -qt_s (\sigma_a^2(k) + \sigma_b^2(k) + \sigma_c^2(k) + \sigma_d^2(k) + \sigma_e^2(k) + \sigma_f^2(k)) + \\
 & q^2 t_s^2 (\sigma_a^2(k) + \sigma_b^2(k) + \sigma_c^2(k) + \sigma_d^2(k) + \sigma_e^2(k) + \sigma_f^2(k)) + \\
 & +q\varepsilon t_s^2 \left(\begin{array}{l} \sigma_a(k)\text{sign}(\sigma_a(k)) + \sigma_b(k)\text{sign}(\sigma_b(k)) + \\ + \sigma_c(k)\text{sign}(\sigma_c(k)) + \sigma_d(k)\text{sign}(\sigma_d(k)) + \\ + \sigma_e(k)\text{sign}(\sigma_e(k)) + \sigma_f(k)\text{sign}(\sigma_f(k)) \end{array} \right) - \\
 & -\varepsilon t_s \left(\begin{array}{l} \xi_{da}(k)\text{sign}(\sigma_a(k)) + \xi_{db}(k)\text{sign}(\sigma_b(k)) + \\ + \xi_{dc}(k)\text{sign}(\sigma_c(k)) + \xi_{dd}(k)\text{sign}(\sigma_d(k)) + \\ + \xi_{de}(k)\text{sign}(\sigma_e(k)) + \xi_{df}(k)\text{sign}(\sigma_f(k)) \end{array} \right) - \\
 & -\varepsilon t_s \left(\begin{array}{l} \sigma_a(k)\text{sign}(\sigma_a(k)) + \sigma_b(k)\text{sign}(\sigma_b(k)) + \\ + \sigma_c(k)\text{sign}(\sigma_c(k)) + \sigma_d(k)\text{sign}(\sigma_d(k)) + \\ + \sigma_e(k)\text{sign}(\sigma_e(k)) + \sigma_f(k)\text{sign}(\sigma_f(k)) \end{array} \right) + \\
 & +q\varepsilon t_s^2 \left(\begin{array}{l} \sigma_a(k)\text{sign}(\sigma_a(k)) + \sigma_b(k)\text{sign}(\sigma_b(k)) + \\ + \sigma_c(k)\text{sign}(\sigma_c(k)) + \sigma_d(k)\text{sign}(\sigma_d(k)) + \\ + \sigma_e(k)\text{sign}(\sigma_e(k)) + \sigma_f(k)\text{sign}(\sigma_f(k)) \end{array} \right) + \varepsilon^2 t_s^2
 \end{aligned} \tag{B.15}$$

B.6. Stability proof of discrete time super-twisting controller based on a Lyapunov function considering disturbances in the model

Considering the system given in (3.100) where:

$$\boldsymbol{\psi}(k+1) = \begin{bmatrix} \mathbf{x}(k+1) \\ \mathbf{u}_1(k+1) \end{bmatrix} = \begin{bmatrix} i_a(k+1) \\ i_b(k+1) \\ i_c(k+1) \\ i_d(k+1) \\ i_e(k+1) \\ i_f(k+1) \\ u_{1a}(k+1) \\ u_{1b}(k+1) \\ u_{1c}(k+1) \\ u_{1d}(k+1) \\ u_{1e}(k+1) \\ u_{1f}(k+1) \end{bmatrix} \quad (\text{B.16})$$

$$\mathbf{x}(k+1) \in \mathfrak{R}^n, \mathbf{u}_1(k+1) \in \mathfrak{R}^n, \mathbf{J} = \begin{bmatrix} \mathbf{G}_{n \times n} & \mathbf{H}_{n \times n} \\ 0 & \mathbf{I}_{n \times n} \end{bmatrix}_{2n \times 2n},$$

$$\mathbf{L}(k) = \begin{bmatrix} -\mathbf{H}_{n \times n} \left(\lambda_1 |\boldsymbol{\sigma}(k)_{n \times 1}|^{1/2} \right) \\ -\mathbf{I}_{n \times n} t s \lambda_2 \end{bmatrix}_{2n \times n}$$

Considering the candidate Lyapunov function:

$$V(k) = \|\boldsymbol{\psi}\|_p^2 \quad (\text{B.17})$$

and:

$$\Delta V(k) := V(k+1) - V(k) \quad (\text{B.18})$$

$$V(k) := \boldsymbol{\psi}^T(k) \mathbf{P} \boldsymbol{\psi}(k) \quad (\text{B.19})$$

then:

$$\Delta V(k) = \boldsymbol{\psi}^T(k+1) \mathbf{P} \boldsymbol{\psi}(k+1) - \boldsymbol{\psi}^T(k) \mathbf{P} \boldsymbol{\psi}(k) \quad (\text{B.20})$$

with $\mathbf{P} \in \mathfrak{R}^{2n \times 2n}$. Replacing (3.101) in (B.20):

$$\begin{aligned} \Delta V(k) = & \mathbf{J}^T \boldsymbol{\psi}^T(k) \mathbf{P} \mathbf{J} \boldsymbol{\psi}(k) + \mathbf{J}^T \boldsymbol{\psi}^T(k) \mathbf{P} \mathbf{L}(k) \text{sign}(\boldsymbol{\sigma}(k)) + \\ & + \mathbf{L}^T(k) \text{sign}(\boldsymbol{\sigma}(k)) \mathbf{P} \mathbf{J} \boldsymbol{\psi}(k) + \mathbf{L}^T(k) \text{sign}(\boldsymbol{\sigma}(k)) \mathbf{P} \mathbf{L}(k) \text{sign}(\boldsymbol{\sigma}(k)) - \\ & - \boldsymbol{\psi}^T(k) \mathbf{P} \boldsymbol{\psi}(k) \end{aligned} \quad (\text{B.21})$$

According to [82], the lambda-inequality is defined as:

$$\mathbf{X}^T \mathbf{Y} + \mathbf{Y}^T \mathbf{X} \leq \mathbf{X}^T \Lambda \mathbf{X} + \mathbf{Y}^T \Lambda^{-1} \mathbf{Y} \quad (\text{B.22})$$

will be applied to the term:

$$\mathbf{J}^T \boldsymbol{\psi}^T(k) \mathbf{P} \mathbf{L}(k) \text{sign}(\boldsymbol{\sigma}(k)) + \mathbf{L}^T(k) \text{sign}(\boldsymbol{\sigma}(k)) \mathbf{P} \mathbf{J} \boldsymbol{\psi}(k).$$

It is considered that:

$$\begin{aligned} \mathbf{X}^T &= \mathbf{J}^T \boldsymbol{\psi}^T(k) \mathbf{P}, & \mathbf{X} &= \mathbf{P} \mathbf{J} \boldsymbol{\psi}(k), \\ \mathbf{Y}^T &= \mathbf{L}^T(k) \text{sign}(\boldsymbol{\sigma}(k)), & \mathbf{Y} &= \mathbf{L}(k) \text{sign}(\boldsymbol{\sigma}(k)) \end{aligned} \quad (\text{B.23})$$

so:

$$\begin{aligned} \mathbf{J}^T \boldsymbol{\psi}^T(k) \mathbf{P} \mathbf{L}(k) \text{sign}(\boldsymbol{\sigma}(k)) + \mathbf{L}^T(k) \text{sign}(\boldsymbol{\sigma}(k)) \mathbf{P} \mathbf{J} \boldsymbol{\psi}(k) \leq \\ \mathbf{J}^T \boldsymbol{\psi}^T(k) \mathbf{P} \Lambda^{-1} \mathbf{J} \boldsymbol{\psi}(k) \mathbf{P} + \mathbf{L}^T(k) \text{sign}(\boldsymbol{\sigma}(k)) \Lambda \mathbf{L}(k) \text{sign}(\boldsymbol{\sigma}(k)) \end{aligned} \quad (\text{B.24})$$

$$\begin{aligned} \mathbf{J}^T \boldsymbol{\psi}^T(k) \mathbf{P} \mathbf{L}(k) \text{sign}(\boldsymbol{\sigma}(k)) + \mathbf{L}^T(k) \text{sign}(\boldsymbol{\sigma}(k)) \mathbf{J} \boldsymbol{\psi}(k) \mathbf{P} \leq \\ \mathbf{J}^T \boldsymbol{\psi}^T(k) \mathbf{P} \Lambda \mathbf{J} \boldsymbol{\psi}(k) \mathbf{P} + \mathbf{L}^T(k) \Lambda^{-1} \mathbf{L}(k) \end{aligned} \quad (\text{B.25})$$

Replacing (B.25) in (B.21) and adding $\varsigma V(k) - \varsigma V(k)$:

$$\begin{aligned} \Delta V(k) \leq & \mathbf{J}^T \boldsymbol{\psi}^T(k) \mathbf{P} \mathbf{J} \boldsymbol{\psi}(k) + \mathbf{J}^T \boldsymbol{\psi}^T(k) \mathbf{P} \mathbf{L}(k) \text{sign}(\boldsymbol{\sigma}(k)) + \\ & + \mathbf{J}^T \boldsymbol{\psi}^T(k) \mathbf{P} \Lambda \mathbf{J} \boldsymbol{\psi}(k) \mathbf{P} + \mathbf{L}^T(k) \Lambda^{-1} \mathbf{L}(k) - \\ & - \boldsymbol{\psi}^T(k) \mathbf{P} \boldsymbol{\psi}(k) + \varsigma V(k) - \varsigma V(k) \end{aligned} \quad (\text{B.26})$$

$$\begin{aligned} \Delta V(k) \leq & \mathbf{J}^T \boldsymbol{\psi}^T(k) \mathbf{P} \mathbf{J} \boldsymbol{\psi}(k) + \mathbf{J}^T \boldsymbol{\psi}^T(k) \mathbf{P} \Lambda^{-1} \mathbf{J} \boldsymbol{\psi}(k) \mathbf{P} + \\ & + \mathbf{L}^T(k) \Lambda \mathbf{L}(k) - \boldsymbol{\psi}^T(k) \mathbf{P} \boldsymbol{\psi}(k) + \varsigma (\boldsymbol{\psi}^T(k) \mathbf{P} \boldsymbol{\psi}(k)) - \varsigma V(k) \end{aligned} \quad (\text{B.27})$$

$$\Delta V(k) \leq \boldsymbol{\psi}^T(k) \left(\mathbf{J}^T (\mathbf{P} + \mathbf{P}\Lambda\mathbf{P}) \mathbf{J} - (1 - \varsigma) \mathbf{P} \right) \boldsymbol{\psi}(k) + \mathbf{L}^T(k) (\Lambda^{-1} + \mathbf{P}) \mathbf{L}(k) - \varsigma V(k) \quad (\text{B.28})$$

Expanding the term $\mathbf{L}^T(k)\mathbf{Z}\mathbf{L}(k)$ with:

$$\mathbf{Z} = (\Lambda^{-1} + \mathbf{P}) = \begin{bmatrix} \mathbf{z}_{11(nxn)} & \mathbf{z}_{12(nxn)} \\ \mathbf{z}_{12(nxn)} & \mathbf{z}_{22n(nxn)} \end{bmatrix}_{2nx2n} \quad (\text{B.29})$$

$$\begin{aligned} \mathbf{L}^T(k)\mathbf{Z}\mathbf{L}(k) &= \begin{bmatrix} -\mathbf{H}_{n \times n} (\lambda_1 |\boldsymbol{\sigma}(k)|^{1/2}) \\ -\mathbf{I}_{n \times n} t_s \lambda_2 \end{bmatrix}^T_{2nx2n} \mathbf{Z} \begin{bmatrix} -\mathbf{H}_{n \times n} (\lambda_1 |\boldsymbol{\sigma}(k)|^{1/2}) \\ -\mathbf{I}_{n \times n} t_s \lambda_2 \end{bmatrix}_{2nx2n} \quad (\text{B.30}) \end{aligned}$$

$$= \begin{bmatrix} -\mathbf{H}\lambda_1 |\boldsymbol{\sigma}(k)|^{1/2} z_{11} - t_s \lambda_2 z_{12} \\ -\mathbf{H}\lambda_1 |\boldsymbol{\sigma}(k)|^{1/2} z_{12} - t_s \lambda_2 z_{22} \end{bmatrix}^T \begin{bmatrix} -\mathbf{H}\lambda_1 |\boldsymbol{\sigma}(k)|^{1/2} \\ -t_s \lambda_2 \end{bmatrix} \quad (\text{B.31})$$

$$= -\mathbf{H}\lambda_1 |\boldsymbol{\sigma}(k)|^{1/2} (-\mathbf{H}\lambda_1 |\boldsymbol{\sigma}(k)|^{1/2} z_{11} - t_s \lambda_2 z_{12}) - t_s \lambda_2 (-\mathbf{H}\lambda_1 |\boldsymbol{\sigma}(k)|^{1/2} z_{12} - t_s \lambda_2 z_{22}) \quad (\text{B.32})$$

$$= \mathbf{H}^2 \lambda_1^2 |\boldsymbol{\sigma}(k)| z_{11} + \mathbf{H} t_s \lambda_1 \lambda_2 z_{12} |\boldsymbol{\sigma}(k)|^{1/2} + \mathbf{H} t_s \lambda_1 \lambda_2 |\boldsymbol{\sigma}(k)|^{1/2} z_{12} + t_s^2 \lambda_2^2 z_{22} \quad (\text{B.33})$$

Applying the lambda-inequality to the term:

$[\mathbf{H} t_s \lambda_1 \lambda_2 z_{12} |\boldsymbol{\sigma}(k)|^{1/2} + \mathbf{H} t_s \lambda_1 \lambda_2 |\boldsymbol{\sigma}(k)|^{1/2} z_{12}]$ with:

$$\begin{aligned} \mathbf{X}^T &= |\boldsymbol{\sigma}(k)|^{1/2}, & \mathbf{X} &= |\boldsymbol{\sigma}(k)|^{1/2}, \\ \mathbf{Y}^T &= \mathbf{H} t_s \lambda_1 \lambda_2 z_{12}, & \mathbf{Y} &= \mathbf{H} t_s \lambda_1 \lambda_2 z_{12} \end{aligned} \quad (\text{B.34})$$

$$\begin{aligned} |\boldsymbol{\sigma}(k)|^{1/2} \mathbf{H} t_s \lambda_1 \lambda_2 z_{12} + \mathbf{H} t_s \lambda_1 \lambda_2 z_{12} |\boldsymbol{\sigma}(k)|^{1/2} &\leq \\ |\boldsymbol{\sigma}(k)|^{1/2} \Lambda |\boldsymbol{\sigma}(k)|^{1/2} + \mathbf{H} t_s \lambda_1 \lambda_2 z_{12} \Lambda^{-1} \mathbf{H} t_s \lambda_1 \lambda_2 z_{12} &\end{aligned} \quad (\text{B.35})$$

$$\begin{aligned} |\boldsymbol{\sigma}(k)|^{1/2} \mathbf{H} t_s \lambda_1 \lambda_2 z_{12} + \mathbf{H} t_s \lambda_1 \lambda_2 z_{12} |\boldsymbol{\sigma}(k)|^{1/2} &\leq \\ |\boldsymbol{\sigma}(k)| \Lambda + \mathbf{H}^2 t_s^2 \lambda_1^2 \lambda_2^2 z_{12}^2 \Lambda^{-1} &\end{aligned} \quad (\text{B.36})$$

So, (B.28) becomes:

$$\begin{aligned} \mathbf{L}^T(k)\mathbf{Z}\mathbf{L}(k) &= \mathbf{H}^2\lambda_1^2|\boldsymbol{\sigma}(k)|\mathbf{z}_{11} + |\boldsymbol{\sigma}(k)|\Lambda + \\ &+ \mathbf{H}^2t_s^2\lambda_1^2\lambda_2^2\mathbf{z}_{12}^2\Lambda^{-1} + t_s^2\lambda_2^2\mathbf{z}_{22} \end{aligned} \quad (\text{B.37})$$

Replacing (B.37) in (B.28):

$$\begin{aligned} \Delta V(k) &\leq \boldsymbol{\psi}^T(k) \left(\mathbf{J}^T(\mathbf{P} + \mathbf{P}\Lambda\mathbf{P})\mathbf{J} - (1 - \varsigma)\mathbf{P} \right) \boldsymbol{\psi}(k) - \varsigma V(k) + \\ &\mathbf{H}^2\lambda_1^2|\boldsymbol{\sigma}(k)|\mathbf{z}_{11} + |\boldsymbol{\sigma}(k)|\Lambda + \mathbf{H}^2t_s^2\lambda_1^2\lambda_2^2\mathbf{z}_{12}^2\Lambda^{-1} + t_s^2\lambda_2^2\mathbf{z}_{22} \end{aligned} \quad (\text{B.38})$$

$$\begin{aligned} \Delta V(k) &\leq \boldsymbol{\psi}^T(k) \left(\mathbf{J}^T(\mathbf{P} + \mathbf{P}\Lambda\mathbf{P})\mathbf{J} - (1 - \varsigma)\mathbf{P} \right) \boldsymbol{\psi}(k) - \varsigma V(k) + \\ &+ \bar{\delta}_1|\boldsymbol{\sigma}(k)| + \bar{\delta}_2 \end{aligned} \quad (\text{B.39})$$

where:

$$\begin{aligned} \bar{\delta}_1 &= \mathbf{H}^2\lambda_1^2\mathbf{z}_{11} + \Lambda \\ \bar{\delta}_2 &= \mathbf{H}^2t_s^2\lambda_1^2\lambda_2^2\mathbf{z}_{12}^2\Lambda^{-1} + t_s^2\lambda_2^2\mathbf{z}_{22} \end{aligned} \quad (\text{B.40})$$

Considering that $\mathbf{Q} = \mathbf{Q}^T > 0$ is the solution for the following LMI:

$$-\mathbf{Q} = \mathbf{A}^T(\mathbf{P} + \mathbf{P}\Lambda\mathbf{P})\mathbf{A} - (1 - \varsigma)\mathbf{P} \quad (\text{B.41})$$

(B.39) becomes:

$$\Delta V(k) \leq -\mathbf{x}^T(k)\mathbf{Q}\mathbf{x}(k) - \varsigma V(k) + \bar{\delta}_1|\mathbf{x}_1(k)| + \bar{\delta}_2 \quad (\text{B.42})$$

$$\Delta V(k) \leq -\|\mathbf{x}(k)\|_Q^2 - \varsigma V(k) + \bar{\delta}_1|\mathbf{x}_1(k)| + \bar{\delta}_2 \quad (\text{B.43})$$

By the Cholesky decomposition [82], the equation (B.43) becomes:

$$\Delta V(k) \leq -\|\mathbf{x}(k)\|_Q^2 + \bar{\delta}_1\|\mathbf{Q}\mathbf{Q}^{-1}\mathbf{x}(k)\| + \bar{\delta}_2 - \varsigma V(k) \quad (\text{B.44})$$

$$\Delta V(k) = -\left(\|\mathbf{Q}^{1/2}x(k)\| - \frac{1}{2}\bar{\delta}_1\right)^T \left(\|\mathbf{Q}^{1/2}x(k)\| - \frac{1}{2}\bar{\delta}_1\right) + \bar{\delta}_2 - \varsigma V(k) + \frac{1}{4}\bar{\delta}_1^{-2}\|\mathbf{Q}^{-1}\|^2 \quad (\text{B.45})$$

Considering that $-\left(\|\mathbf{Q}^{1/2}\mathbf{x}(k)\| - \frac{1}{2}\bar{\delta}_1\right)^T \left(\|\mathbf{Q}^{1/2}\mathbf{x}(k)\| - \frac{1}{2}\bar{\delta}_1\right)$ is always negative, (B.45) can be rewritten as:

$$\Delta V(k) \leq -\varsigma V(k) + \Theta \quad (\text{B.46})$$

where:

$$\Theta = \bar{\delta}_2 - \varsigma V(k) + \frac{1}{4}\bar{\delta}_1^{-2}\|\mathbf{Q}^{-1}\|^2 \quad (\text{B.47})$$

So, it has that:

$$V(k+1) \leq -(\varsigma - 1)V(k) + \Theta \quad (\text{B.48})$$

The solution of (B.48) is given by:

$$V(k+1) \leq (1-\varsigma)^k V(0) + \sum_{i=1}^k (1-\gamma_x)^{i-1} \Theta \quad (\text{B.49})$$

If k goes to infinity:

$$\lim_{k \rightarrow \infty} V(k) \leq \frac{\Theta}{1-\varsigma} \quad (\text{B.50})$$

the radius of the convergence region of the discrete time super-twisting algorithm is given by:

$$R \leq \frac{\Theta}{1-\varsigma} \quad (\text{B.51})$$

Then, it can conclude that the trajectories of the dynamic systems gives in (3.101) converges asymptotically to a ball B_r centred at the origin $B_r := \{x : \|x\|^2 < R\}$ characterized with a radius:

$$R = \frac{\Theta}{1-\varsigma} \quad (\text{B.52})$$

Schriftenverzeichnis Elektrische Energiesysteme

Herausgegeben von / Edited by

Kompetenzzentrum für Dezentrale Elektrische Energieversorgungstechnik

- Band 1:** Wechselrichtersysteme mit Stromzwischenkreis zur Netzanbindung von Photovoltaik-Generatoren, Kassel 2010, ISBN 978-3-89958-912-2
Benjamin Sahan
- Band 2:** Methode zur Evaluation leistungselektronischer Schaltungstopologien für die Anwendung in dezentralen Netzeinspeisern kleiner Leistung, Kassel 2011, ISBN 978-3-86219-094-2
Thorsten Bülo
- Band 3:** On the Perspectives of Wide-Band Gap Power Devices in Electronic-Based Power Conversion for Renewable Systems, Kassel 2013, ISBN 978-3-86219-486-5
Samuel Vasconcelos Araújo
- Band 4:** Development of Brushless Self-excited and Self-regulated Synchronous Generating System for Wind and Hydro Generators, Kassel 2014, ISBN 978-3-86219-018-8
Likaa Fahmi Ahmed Izzat
- Band 5:** Untersuchung eines Ringgenerators für Windenergieanlagen der 10 MW-Klasse auf Basis statischer Versuchsmodelle und numerischer Simulationen, Kassel 2014, ISBN 978-3-86219-732-3
Anna Katharina Messoll
- Band 6:** Modellierung der parasitären passiven Elemente in IGBT-Hochleistungsmodulen, Kassel 2014, ISBN 978-3-86219-752-1
Michael Heeb
- Band 7:** Permanentmagnetische Vormagnetisierung von Speicherdrosseln in Stromrichtern, Kassel 2014, ISBN 978-3-86219-820-7
Jens Friebe
- Band 8:** Analysis and Comparison of Power Electronic Converters with Electronic Isolation, Kassel 2015, ISBN 978-3-86219-822-1
Mehmet Kazanbas
- Band 9:** Optimierung von PV-Wechselrichtern im Netzparallelbetrieb mithilfe analytischer Verhaltens- und Verlustleistungsmodelle, Kassel 2015, ISBN 978-3-86219-924-2
Julia Pinne

- Band 10:** Auswirkungen der Netzintegration von Windkraftanlagen auf die Spannungsstabilität im Nördlichen Verbundsystem Chiles, Kassel 2015, ISBN 978-3-86219-986-0
Darío Lafferte
- Band 11:** Untersuchung des Betriebsverhaltens einer Windkraftanlage mit permanenterregten Synchrongeneratoren für den Einsatz im Offshore-Bereich, Kassel 2015, ISBN 978-3-86219-966-2
Adil Ezzahraoui
- Band 12:** PV-Stromrichter höherer Leistung für 1.500 V Systemspannung. Bewertung, Vergleich, Realisierung, Kassel 2016, ISBN 978-3-7376-0118-4
Christian Nöding
- Band 13:** Investigation on Performance Advantage of Functionally Integrated Magnetic Components in Decentralised Power Electronic Applications, Kassel 2017, ISBN 978-3-7376-0226-6
Thiemo Kleeb
- Band 14:** Discrete time sliding mode control strategies applied to a multiphase brushless DC machine, Kassel 2017, ISBN 978-3-7376-0318-8
Milena Sabrina Godoi Dias

Nowadays, environmental issues motivates the replacement of mechanical, hydraulic and pneumatic system by electrical system in the transport sector aiming to reduce emissions generated by burning of fossil fuels in vehicles. The electrical system must ensure high electrical efficiency and should not exceed the weight of the substituted components. To attend these high performance requirements a fault-tolerant multiphase brushless DC machine was chosen for this research.

The present work introduces a six-phase 600 W brushless DC machine with 8 poles. The main challenge for the control issues of this machine is the mutual magnetic coupling between the phases due to the wave winding machine configuration.

In this context, theoretical and practical investigations of different current control strategies based on the sliding mode control approach applied to the six-phase brushless DC machine are presented.

ISBN 978-3-7376-0318-8



9 783737 603188 >